ABSTRACT

K*(892) Resonance Production in Au+Au and p+p Collisions
at $\sqrt{s_{NN}}$=200GeV at the Relativistic Heavy Ion Collider

Haibin Zhang
Yale University
May 2004

The Relativistic Heavy Ion Collider (RHIC) makes it possible to study high density nuclear matter under extreme conditions. Hadronic resonance states have extremely short lifetimes (few fm/c) which are comparable to the lifetime of the hot dense matter in ultra-relativistic heavy ion collisions. K*(892), as a vector meson resonance, is a unique tool to probe various properties of the hot dense matter. Measurements of K*(892) production in Au+Au and p+p collisions at $\sqrt{s_{NN}} = 200GeV$ are addressed in this thesis.

The hadronic decay channels of $K^{*0}(892) \rightarrow K\pi$ and $K^{*\pm}(892) \rightarrow K^0_S\pi^\pm$ are studied using the STAR detector at RHIC in Brookhaven National Laboratory. Collision data were taken during the RHIC runs of 2001 and 2002. K^{*0} and $K^{*\pm}$ signals are reconstructed using the event-mixing technique. K^{*0} mass shift as a function of transverse momentum is studied in both Au+Au and p+p collisions. The mid-rapidity ($|y| < 0.5$) K^{*0} and $K^{*\pm}$ yields and inverse slope parameters are measured in pp and Au+Au data with various collision centralities. K^{*0} mean transverse momentum distributions for different collision centralities are discussed. The K^*/K ratios in Au+Au collisions are found to be significantly lower than the ratio in pp collisions. K^*/K and ϕ/K^* ratios are compared to different collision systems with various collision energies. The nuclear modification factor (R_{AA}) of K^* at the intermediate p_T is similar to the K^0_S R_{CP} and different from the Λ R_{CP}. Results on K^{*0} elliptic flow in Au+Au collisions are addressed. Physics implications of these measurements are discussed in this thesis.

K*(892) Resonance Production in Au+Au and p+p Collisions at $\sqrt{s_{NN}}$=200GeV at the Relativistic Heavy Ion Collider

A Dissertation
Presented to the Faculty of the Graduate School
of
Yale University
in Candidacy for the Degree of
Doctor of Philosophy

By
Haibin Zhang

Dissertation Director: Prof. Jack Sandweiss
Off-campus Co-adviser: Dr. Zhangbu Xu

May 2004

Acknowledgments

I would like to thank my adviser, Prof. Jack Sandweiss. He has guided me through the graduate school since my first graduate physics class on Quantum Mechanics in 1999 to the last three years of my PhD research. His enormous physics knowledge and enthusiasms in the physics research deeply impressed me. His constant encouragement made sure my PhD research going well. I also would like to thank Dr. Zhangbu Xu, the co-adviser of my PhD research. He guided me through all the detailed analysis in my research. Without him, I must be still struggling in the research. He is not only one of the advisers in my PhD research, but also one of my best friends in my life.

My gratitude also goes to Richard Majka and Evan Finch. Any discussion with them always helped me learn more. Evan Finch deserves many thanks for his hard work on making all the corrections of my thesis. I also cannot forget all the happy life with Alexy Chikanian, Fu Du and two former group members: Sotiria Batsouli and Guangqin Wei. Dr. Patricia Fachini in BNL also deserves my many thanks with her tremendous help on my research.

I also would like to thank all the members in the STAR Collaboration. I learnt a lot from almost everyone in the collaboration. Special thanks should go to all the members in the STAR spectra physics working group for their helps and discussions with my analysis work.

I would like to thank my thesis committee, Prof. Jack Sandweiss, Dr. Zhangbu Xu, Prof. John Harris, Prof. Yoram Alhassid, Prof. Michael Zeller, Professor Andreas Heinz and my outside reader Prof. Jamie Nagle in University of Colorado at Boulder for their careful reading and important critism of the thesis.

Many thanks to Rochelle Lauer for setting up all the computers. I also would like to thank the graduate registrar Jo-Ann Bonnett and secretary Carole DeVore and Lillian Vinston for their helps.

I would like to acknowledge the sacrifices made by my wife, Lili Shou. She has given me the most important support in the passed three years. Special thanks to my parents for encouraging me doing research for years.

Contents

List of Figures

List of Tables

Chapter 1

Physics

1.1 The Physics of Relativistic Heavy Ion Collisions

1.1.1 Deconfinement in QCD and Phase Diagram

The strong interaction, the force which binds protons and neutrons together into atomic nuclei, is generally understood to be described by the field theory of Quantum Chromodynamics (QCD), a theory in which different types, of 'flavors' of massive quarks interact via the exchange of massless gluons. This theory is superficially quite similar to the description of the electromagnetic interaction by the incredibly successful theory of Quantum Electrodynamics [3].

There are two remarkable features of QCD. At large distances or small momentum transfer (Q^2), the strong coupling constant (α_s) is large and quarks are confined in colorless particles. At short distances or large momentum transfer, the coupling constant is small. This is the regime of asymptotic freedom. Lattice QCD calculations, considering two light quark flavors, predict a phase transition from a confined phase, hadronic matter, to a deconfined phase, or quark gluon plasma (QGP), to occur at a temperature of approximately 150 MeV [1].

Figure 1.1 shows the phase diagram of the hadronic and partonic matter. A phase

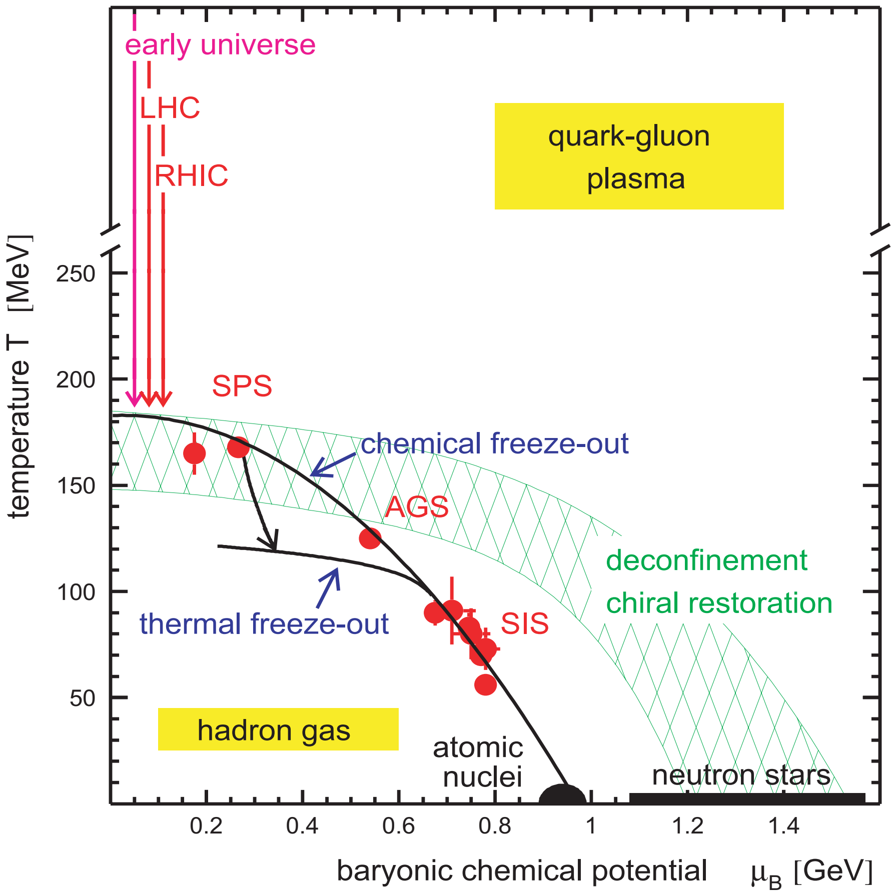

Figure 1.1: Phase diagram of hadronic and partonic matter. Figure is taken from [2].

transition from the confined hadronic matter to the deconfined QGP matter is expected to happen at either high temperature or large baryon chemical potential μ_B. Experiments on relativistic heavy ion collisions are designed to search for and study the deconfined QGP matter.

1.1.2 Relativistic Heavy Ion Collisions

The experimental programs in relativistic heavy ions using the BNL-AGS and CERN-SPS started in 1986. At BNL, ion beams of silicon and gold, accelerated to momenta of 14 and 11 GeV/c per nucleon, respectively, have been utilized in 10 fixed-target experiments. There have been 15 heavy ion experiments at CERN utilizing beams of oxygen at 60 and 200 GeV/c per nucleon, sulphur at 200 GeV/c per nucleon and Pb at 160 GeV/c per nucleon [1].

The Relativistic Heavy Ion Collider (RHIC) at BNL is designed for head on Au+Au collisions at $\sqrt{s_{NN}} = 200$ GeV. The first RHIC run was performed in 2000 with Au+Au collisions at $\sqrt{s_{NN}} = 130$ GeV/c in four experiments, STAR, PHENIX, PHOBOS and BRAHMS. The second RHIC run was in 2001 and 2002 with Au+Au and p+p collisions at $\sqrt{s_{NN}} = 200$ GeV.

The above mentioned relativistic heavy ion collision experiments are designed for the search and study of the possible deconfined high energy density matter, the quark gluon plasma. In head on relativistic heavy ion collisions, two nuclei can be represented as two thin disks approaching each other at high speed because of the Lorentz contraction effect in the moving direction. The initial stage of these collisions can be described as the interpenetration of the nuclei with partonic interactions at high energy. This stage features the creation of high p_T jets, $c\bar{c}$ pairs or other products of high momentum transfer scattering processes on the parton level. With the interactions of the partons in the system, we expect that chemical and local thermal equilibrium of the system will be reached and thus the QGP forms [4]. As the QGP system expands and cools down, mesons and baryons emerge with their abundances expected to be fixed by hadronization temperature and chemical fugacities. This stage of fireball evolution is commonly known as chemical freeze-out. After initial hadronization, the system may evolve as an interacting hadron gas. At a certain point (which can vary according to particle species), kinetic freeze-out, where hadrons stop interacting, is reached [5]. Because a comprehensive understanding of the collision process is currently impossible, we'll now discuss a few important physics approaches on relativistic heavy ion collisions in the following sections.

1.1.3 Statistical Model

Experiments on relativistic heavy ion collisions are designed to look for the production of a quark-gluon plasma phase which subsequently hadronizes. One of the crucial questions is whether thermal and chemical equilibrium is achieved at some stage of the collision. Applying a statistical model which assumes equilibrium, and testing experimental data against model predictions is one way of testing reality against the idea of a thermally and chemically equilibrated fireball at the point of hadro-chemical freeze-out [6].

The present statistical model is based on the use of a grand canonical ensemble to describe the partition function and hence the density of particle species i in an equilibrated fireball:

$$n_i = \frac{g_i}{2\pi^2} \int_0^\infty \frac{p^2 dp}{e^{(E_i(p)-\mu_i)/T} \pm 1} \tag{1.1}$$

with particle density n_i, spin degeneracy g_i, momentum p, total energy E and chemical potential $\mu_i = \mu_B B_i - \mu_S S_i - \mu_{I_3} I_i^3$. The quantities B_i, S_i and I_i^3 are the baryon number, the strangeness number and the third-component of the isospin quantum number of the particle of species i. The temperature T and the baryochemical potential μ_B are the two independent parameters of the model, while the volume of the fireball V, the strangeness chemical potential μ_S, and the isospin chemical potential

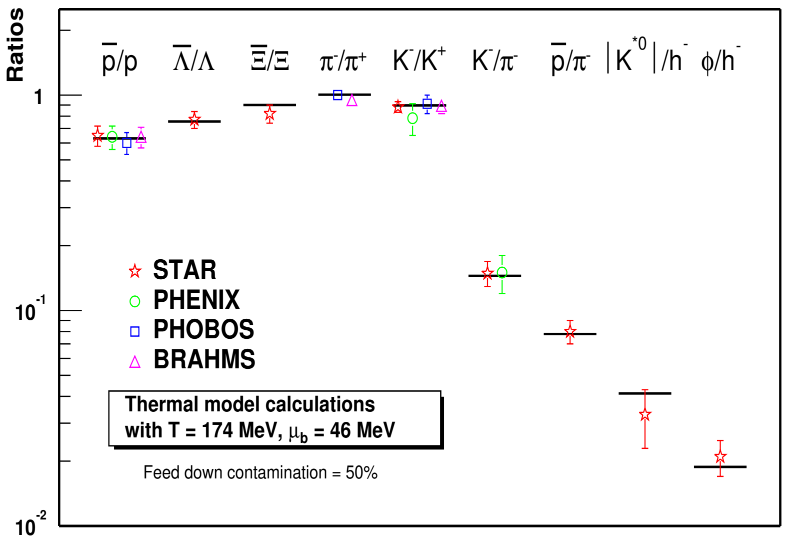

Figure 1.2: Comparison between RHIC experimental particle ratios and statistical model calculations with $T = 174$ MeV and $\mu_B = 46$ MeV. Figure is taken from [7].

μ_{I_3} are fixed by the three conservation laws for

$$\text{baryon number: } V\sum_i n_i B_i = Z + N \tag{1.2}$$

$$\text{strangeness: } V\sum_i n_i S_i = 0 \tag{1.3}$$

$$\text{charge: } V\sum_i n_i I_i^3 = \frac{Z-N}{2} \tag{1.4}$$

This statistical model has been applied to fit the recent RHIC experimental data in Au+Au collisions at $\sqrt{s_{NN}}$= 130 GeV. By using the various particle ratios obtained from the STAR, PHENIX, PHOBOS and BRAHMS experiments at RHIC, the best agreement of the model and the data is achieved with minimal χ^2 at the baryon chemical potential $\mu_B \simeq 46\pm 5$ MeV and the temprature $T \simeq 174\pm 7$ MeV [6]. The comparison of the RHIC experimental particle ratios and the statistical model calculations is shown in Figure 1.2.

1.1.4 Jet Quenching

In deconfined quark and gluon matter at high energy density, partons propagating will lose energy through gluon bremsstrahlung, with the magnitude of the energy loss predicted to depend strongly on the gluon density of the medium. Such a partonic stage energy loss could soften the fragmentation of jets, leading to the suppression of high transverse momentum (high p_T) hadrons in the final state. This effect is usually called jet quenching. Thus a measurement of partonic energy loss and the suppression of high p_T hadrons therefore provides unique probe of the density of the medium [8]. In order to measure the high p_T hadron suppression in relativistic heavy ion collisions, the comparison of the hadron p_T spectra relative to reference data from nucleon-nucleon collisions at the same collision energy is needed. This comparison should also consider the nuclear effect of the colliding nuclei. Thus the nuclear modification factor is defined as

$$R_{AA}(p_T) = \frac{d^2N^{AA}/dp_T d\eta}{T_{AA} d^2\sigma^{NN}/dp_T d\eta} \tag{1.5}$$

where $T_{AA} = \langle N_{\mathrm{bin}}\rangle/\sigma_{\mathrm{inel}}^{NN}$ accounts for the collision geometry, averaged over the event

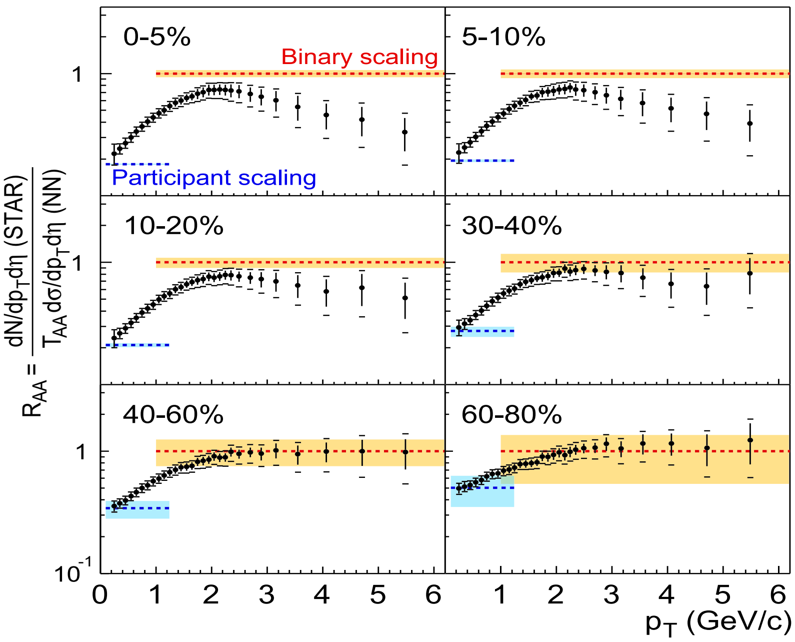

Figure 1.3: $R_{AA}(p_T)$ for various centrality bins, for Au+Au relative to an NN reference spectrum. Figure is taken from [8].

centrality class. $\langle N_{\rm bin}\rangle$, the equivalent number of binary NN collisions, is calculated using a Glauber model. $R_{AA}(p_T)$ is less than unity at low p_T. In contrast, the yield for hard processes scales as $\langle N_{\rm bin}\rangle$ in the absence of nuclear medium effects $[R_{AA}(p_T) = 1]$ [8].

Figure 1.3 shows $R_{AA}(p_T)$ for various centrality bins in Au+Au collisions at $\sqrt{s_{NN}}$=130 GeV relative to an NN reference spectrum. $R_{AA}(p_T)$ increases monotonically for $p_T <$ 2 GeV/c at all centralities and saturates near unity for $p_T >$ 2 GeV/c in the most peripheral bins. In contrast, $R_{AA}(p_T)$ for the central bins reaches a maximum and then decreases strongly above p_T = 2 GeV/c, showing the suppression of the charged hadron yield relative the NN reference. $R_{AA}(p_T)$ varies continuously as a function of centrality, and no centrality threshold for the onset of suppression is observed [8].

Since $R_{AA}(p_T)$ at $p_T >$ 2 GeV/c in peripheral Au+Au collisions is close to unity, the high p_T hadron suppression in central Au+Au collisions can also be investigated by comparing the hadron spectra in central and peripheral Au+Au collisions. Thus R_{CP}

is defined as

$$R_{CP} = \frac{\langle N_{\rm bin}^{\rm peripheral}\rangle d^2N^{\rm central}/dp_Td\eta}{\langle N_{\rm bin}^{\rm central}\rangle d^2N^{\rm peripheral}/dp_Td\eta} \tag{1.6}$$

1.1.5 Strangeness Enhancement

A long standing prediction for a signature of QGP formation is the enhancement of strange hadrons. The production of strange hadrons relative to nonstrange hadrons is suppressed in hadronic reactions. This suppression increases with increasing strangeness content of the hadron. In a QGP, the strange quark content is rapidly saturated by $s\bar{s}$ pair production in gluon-gluon reactions, resulting in an enhancement in the production of strange hadrons over what would be expected if no QGP was formed. In particular, multi-strange baryons and strange antibaryons are predicted to be strongly enhanced when a QGP is formed. Furthermore, it has been shown that an enhanced

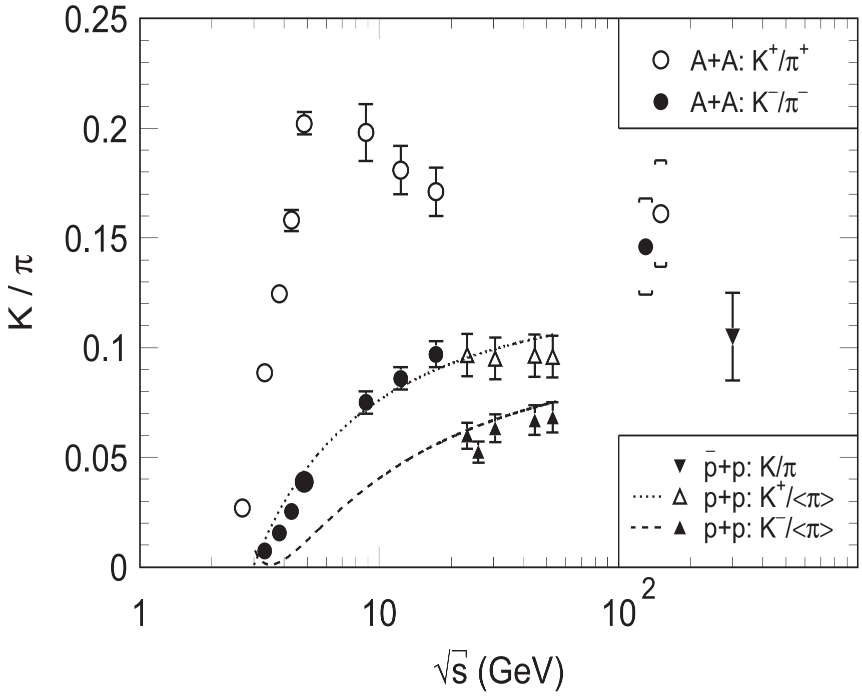

Figure 1.4: Mid-rapidity K/π ratios versus $\sqrt{s_{NN}}$ indicating possible information on strangeness enhancement. Figure is taken from [9].

strangeness content cannot be destroyed nor generated by interactions during expansion and freeze-out [1].

Strangeness production has been studied in heavy-ion collisions at the AGS, SPS and RHIC. The ratio of kaon to pion production is often used to quantify the strangeness production enhancement. Figure 1.4 shows the mid-rapidity K/π ratios versus collision energy $\sqrt{s_{NN}}$ in A+A and p+p collisions at the AGS, SPS and RHIC. A significantly rapid increase of K^+/π^+ ratios from relatively low AGS energy to SPS energy is observed. The ratio then saturates and keeps constant from $\sqrt{s_{NN}} \sim 10$ to 130 GeV. The ratios in A+A collisions at these energies is large compared to p+p collisions at similar energies indicating the strangeness production enhancement in A+A collisions [9].

1.1.6 Elliptic Flow

In non-central Au+Au collisions, the event in the plane perpendicular to the beam axis exhibits an azimuthally anisotropic shape, so the momentum space distribution does bot need to be cylindrically symmetric. The azimuthal particle distributions in momentum space can be expanded in a form of Fourier series

$$E\frac{d^3N}{d^3p} = \frac{1}{2\pi}\frac{d^2N}{p_T dp_T dy}(1 + \sum_{n=1}^{\infty} 2v_n \cos[n(\phi - \Psi_r)]) \tag{1.7}$$

where Ψ_r denotes the reaction plane angle. The Fourier expansion coefficient v_n stands for the nth harmonic of the event azimuthal anisotropies. Anisotropic flow corresponding to the second harmonic (with coefficient v_2) plays a very important role in non-central Au+Au collisions and people use a special term "elliptic flow" to denote this. The word "elliptic" is due to the fact that in polar coordinates an azimuthal distribution with nonzero second harmonic represents an ellipse. The long axis of the "ellipse" of the particle distribution in momentum space together with the beam axis defines the event's reaction plane [10].

Among the first experimental results from RHIC were measurements of v_2 as a function of collision centrality for charged hadrons, and v_2 as a function of p_T for charged hadrons, as well as identified charged pions, charged kaons, and protons ($p_T < 0.9$

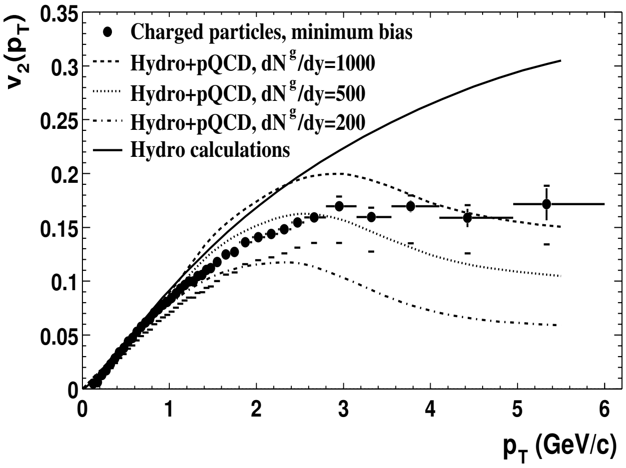

Figure 1.5: $v_2(p_T)$ for minimum-bias events (circle). The error bars represent the statistical errors and the caps show the systematic uncertainty. The data are compared with hydro + pQCD calculations assuming the initial gluon density dN^g/dy=1000 (dashed line), 500 (dotted line), and 200 (dash-dotted line). Also shown are pure hydrodynamical calculations (solid line). Figure is taken from [12].

GeV/c). Further results from RHIC have shown that in the low momentum region ($p_T < 2$ GeV/c) hydrodynamic model calculations provide a good description of v_2 as a function p_T for π, K, p, and Λ. Alternatively, in the region $p_T > 2.5$ GeV/c, the hard scattering of partons apparently become prominent and the hydrodynamic model predictions fail. These results may be explained by assuming a high initial gluon density and energy loss in an early partonic stage [11].

More importantly however, RHIC has shown that, combined with observations of transverse radial flow, the measurement of elliptic flow for multiply strange baryons may provide a key and definitive insight into a state of matter and possible partonic collectivity in the early stage of the collision. Specifically, significant elliptic flow observed e.g. for the Ξ and Ω, would be a clear indication of partonic collectivity in the initial stages of the collision [11].

1.1.7 Heavy Flavor

Charm quark production in relativistic heavy ion collisions is particularly sensitive to the early gluon dominated stages of the collision. Most $c\bar{c}$ production is expected to occur during the early partonic stages, much of it via hard gluon fusion, $gg \rightarrow c\bar{c}$ production during the initial stage. Because the yield of charm is sensitive to the details of the early stages, the measurement of the charm production rate is very important for determining a proper description the initial conditions and the early stages of relativistic nucleus-nucleus collisions [11].

Studying the energy loss of partons in QCD matter is an exciting new possibility afforded for the first time by the high energy of the RHIC machine. For a heavy quark, the amount of energy loss in the medium is expected to be lower than for a light quark due to suppression of gluon radiation at small angles (the "dead cone effect" [13]). This is expected to result in charm enhancement at moderate p_T. One calculation [13] shows a factor of 2 enhancement of D/π ratio at $p_T \sim 5$ GeV/c in hot QGP matter compared to the yield expected in pp collisions.

The production of J/ψ particles in a quark-gluon plasma is predicted to be suppressed. This is a result of the Debye screening of a $c\bar{c}$ pair, initially formed in the QGP by fusion of two incident gluons. Less tightly bound excited states of the $c\bar{c}$ system, such as ψ' and χ_c, are more easily dissociated and will be suppressed even more than the J/ψ. Thus a measurement of charmonium production in relativistic heavy-ion collisions and its yield suppression relative to the yield produced in cold hadronic matter could be a unique signal to study properties of a deconfined QGP matter [1]. Another important element of the study of charmonium suppression in QGP matter is to study the production of open charm, such as D^0, $D^{\pm}$, D^*, etc. Since the open charm can be produced under the same initial gluon conditions, the measurement of open charm production can provide a good reference for the study of charmonium suppression in relativistic heavy ion collisions.

1.2 Resonance Production and Probing Freeze-Out Evolution

If a particle can decay by strong interaction, it does so very quickly. Strongly decaying particles have lifetimes (τ) about 10^{-23} s (about the time it takes a light signal to cross a proton) and such particles are called resonances [14].
Resonances' decay lengths are extremely short, in the scale of a few fm. Their widths (Γ) and lifetimes obey the uncertainty principle $\Gamma \times \tau = \hbar c$. A typical resonance is the K^* vector meson which has a lifetime of 4 fm/c and width of 50.7 MeV/c^2 [15].
Some resonances are excited states of corresponding stable particles. For example, the K^* vector meson resonance is the excited state of the Kaon pseudo-scalar meson.

1.2.1 A Little Bit of History on Resonances

In 1952, Anderson, Fermi and their collaborators at Chicago started their classic experiments on the pion-nucleon interaction at low energy. They used the external pion beams from the Chicago synchrocyclotron as a source of particles, and discovered what was for a long time called the pion-nucleon resonance. This newly found resonance was in the 3/2 isospin state and had an angular momentum of 3/2. The discovery of the pion-nucleon resonance was of paramount importance to the high energy physics community at that time and encouraged the study and discovery of hundreds of resonances in the following years [16].
With the establishment of the hydrogen bubble chamber in 1950s, entirely new possibilities for research into high energy physics presented themselves. Results quickly became apparent in the form of newly discovered elementary particles [16].
In 1960, Luis W. Alvarez, et al, announced the discovery of the first resonance Y_I^* (which is known as $\Sigma^*(1385)$ now) at the Rochester High Energy Physics Conference. Their $K^- + p \rightarrow \Lambda + \pi^+ + \pi^-$ experiments provided proof that the $\pi^\pm$ recoiled against a combination of $\Lambda + \pi^\mp$ that had a unique mass, broadened by the effects of the uncertainty principle. The mass of the $\Lambda\pi$ combination was calculable as 1385 MeV

and the isospin of the system was 1. Although the famous Fermi pion-nucleon resonance had been known for years, the impact of the $\Sigma^*(1385)$ resonance was quite different since it really acted like a new particle and was not simply a resonance in a cross section [16].

Before the end of 1960, the same group that had found the $\Sigma^*(1385)$ found two other strange resonances, the $K^*(890)$ and the $\Lambda(1405)$. During the discovery of the $K^*(890)$, a bump shape in the invariant mass spectrum was for the first time used to establish the existence of a particle. Soon after that, the ρ, ω and η vector meson resonances were discovered. In 1962, the $\Xi^*(1530)$ resonance was discovered and reported. By the year 1967, around 1411 resonances had been discovered [16].

In recent years, experiments using relativistic heavy ion collisions have provided opportunities for the use of resonances to study various properties of the hot and dense nuclear matter under extreme conditions. In the STAR experiment at RHIC, the following resonances have been measured: $\rho^0(770)$ [17], $K^*(892)$ [18], $f_0(980)$ [19], $\phi(1020)$ [20], $\Delta(1232)$ [21], $\Sigma^*(1385)$ [22], $\Lambda(1520)$ [23] and $\Xi^*(1530)$ [24]. Table 1.1 lists the resonances measured in the STAR experiment with their measured decay channels and branching ratios, widths and lifetimes.

Resonance	Decay Channel	Branching Ratio	Width (MeV/c^2)	Lifetime (fm/c)
$\rho^0(770)$	$\pi^+\pi^-$	$\sim$100%	150	1.3
$K^*(892)$	$K\pi$	$\sim$100%	50.7	4
$f_0(980)$	$\pi^+\pi^-$	dominant	40 to 100	2 to 5
$\phi(1020)$	K^+K^-	49.2%	4.46	44
$\Delta(1232)$	$p\pi$	>99%	$\sim$120	$\sim$1.6
$\Sigma^*(1385)$	$\Lambda\pi$	88.2%	35.8	5.5
$\Lambda(1520)$	pK	22.5%	15.6	13
$\Xi^*(1530)$	$\Xi\pi$	$\sim$100%	9.1	22

Table 1.1: The resonances measured in the STAR experiment with their measured decay channels and branching ratios, widths and lifetimes.

1.2.2 Resonance In-Medium Effects

One of the most exciting new directions in nuclear physics is to study how nuclear phenomena change as the environment changes. Thus relativistic heavy ion experiments are designed to probe the state of nuclear matter at extremely high temperature and high density. They make it possible for us to probe the properties of individual hadrons in close encounters with other strongly interacting hadrons in the hot-dense matter. These processes should reflect the change of the strong interaction vacuum as density and temperature are turned on [25]. Here we use the term "the hadrons' in-medium effects" to denote the high density and/or high temperature medium related modification of the individual hadrons properties.

In contrast, the relatively stable particles, such as Λ, D^0, etc., with their lifetimes much greater than the lifetime of the fireball would decay after the kinetic freeze-out when all the hadrons stop interacting so that all the accumulated hot-dense medium related effects will be blurred. We thus cannot expect to observe any in-medium effects by measuring these stable particles. Fortunately, resonances with extremely short lifetimes can decay inside the medium before all the accumulated in-medium effects might be erased. Thus by measuring resonance production, one can access information about how the resonances encounter the hot-dense medium.

One important approach on the studies of the hadrons' in-medium effects was theoretically addressed by G. E. Brown and M. Rho in 1991 [25] which was well known as the Brown-Rho scaling. They started with a known structure of an effective Lagrangian at low energy and zero density (i.e., free space), dictated by symmetries and other constraints of QCD (e.g., chiral symmetry). Then they studied how this theory evolves as density (or temperature) is increased by embedding a hadron in dense matter which is equivalent to changing the vacuum and thereby modifying quark and gluon condensates. Thus they had, as density increases, the same Lagrangian but with the masses and coupling constants of the theory modified according to the symmetry constraints of QCD. Finally, they established the famous approximate in-medium scaling law:

$$m_\sigma^*/m_\sigma \approx m_N^*/m_N \approx m_\rho^*/m_\rho \approx m_\omega^*/m_\omega \tag{1.8}$$

where the masses without asterisks stand for free-space values and the masses with asterisks stand for the values in the dense medium.

R. Rapp also has made recent theoretical studies [26] on the thermal $\pi^+\pi^-$ emission spectra from the late stages of heavy ion reactions at ultra-relativistic energies considering the hadronic in-medium effects. He started with the ρ-propagator D_ρ at finite temperatures and baryon densities:

$$D_\rho = \frac{1}{M^2 - (m_\rho^{(0)})^2 - \Sigma_{\rho\pi\pi} - \Sigma_{\rho M} - \Sigma_{\rho B}} \tag{1.9}$$

The in-medium self-energy terms consist of three parts: (1) $\Sigma_{\rho\pi\pi}$ represents the free decay width into 2-pion states; (2) $\Sigma_{\rho M}$ describes resonant ρ-interactions with surrounding π, K and ρ mesons; (3) $\Sigma_{\rho B}$ accounts for the resonant ρ-interactions with surrounding nucleons, hyperons and baryon resonances. Finally, he reached the in-medium ρ spectral function

$$\frac{dR_{\rho\to\pi\pi}}{dM} = -\frac{6}{\pi}\frac{g_\rho^2}{6\pi}\frac{k^3}{M}F_{\rho\pi\pi}(k)^2 \times ImD_\rho(M;\mu_B,T)(\frac{MT}{2\pi})^{3/2}e^{-(M-\mu_\rho)/T} \tag{1.10}$$

Thus the spectral function for the ρ resonance in a medium with finite density and finite temperature would have a smaller mass peak and wider width than the spectral function for the ρ in a free space. This study implies the resonance in-medium effects would modify the resonance mass, width and even the line shape.

E. V. Shuryak and G. E. Brown have also recently studied resonance in-medium effects [27]. Besides the resonance-pion s-channel interactions which might modify the resonance properties according to the Brown-Rho scaling, the resonance-pion t-channel interactions can also modify the resonance properties. In the case of the ρ resonance, it can scatter with a pion in the medium to temporarily form an a_1 resonance. After the a_1 resonance decays back to a ρ and a pion, the ρ properties might have been modified by this t-channel interactions. They predicted that in the hot-dense medium, a downward mass shift for the ρ and K^* resonance and a upward mass shift for the Δ resonance can be expected.

Thus a systematic measurement of various types of resonances, such as $\rho(770)$, $K^*(892)$, $\Delta(1232)$, etc., and their properties in the hot-dense matter, such as masses, widths and line shapes in relativistic heavy ion collisions is needed to study the hadrons' in-medium effects.

1.2.3 Re-scattering Effect and Re-generation Effect

Resonances have extremely short lifetimes (a few fm/c), which are comparable to the lifetime of the hot-dense matter formed in relativistic heavy ion collisions. The resonances can be thermally produced at the chemical freeze-out stage. Their short lifetimes make it possible for the resonances' decayed daughters to undergo a period of re-interaction in the hadron gas phase [28, 29, 30, 31].

A portion of the resonances may decay before the kinetic freeze-out stage and their hadronic decay daughter particles might be re-scattered by other particles in the hadron gas. This is called the resonance daughter particles' re-scattering effect. This effect may destroy a part of the resonance signals. At the same time, the hadronic particles in the medium can interact with each other to produce a part of the resonance signals. This is called the re-generation effect, and can compensate in part for the resonance yield lost due to the re-scattering effect.

The portion of the resonance signals destroyed by its daughter particles' re-scattering effect depends on the resonance lifetime, its daughter particle's interaction cross sections with the hadrons in the medium, the time scale between the chemical and kinetic freeze-outs and the density of the medium. The amount of the resonance signals which can be produced by the re-generation effect depends on the interaction cross sections for hadrons to produce the resonance, the time scale allowed for this re-generation effect and the medium density.

Due the resonance daughter particles' re-scattering effect and the re-generation effect, resonances are good candidates to probe various properties of the hot-dense matter in relativistic heavy ion collisions, in particular the fireball evolution properties between chemical and kinetic freeze-outs, and the time scale between the two freeze-outs [28, 32, 33, 34, 35].

1.2.4 Measuring the Time Scale between Chemical and Kinetic Freeze-outs

An important aspect in the study of heavy ion collisions is to determine the time scale governing hadron production and the duration of the decoupling (freeze-out) process. At present there is no general consensus on the freeze-out time scale, and hence on how much observed particles "remember" about their primordial source. The Quark Gluon Plasma (QGP) signals should be visible in hadronic particles if freeze-out is explosive (zero time between chemical and kinetic freeze-outs). However, in principle the newly-formed hadrons could undergo a period of re-interaction in a hadronic gas phase. This re-interaction phase between chemical and kinetic freeze-outs, the time scale of which could be hadron-specific, could significantly alter any considered QGP signals. Thus an estimation of the time scale between chemical and kinetic freeze-outs is of great interest. The measurements of short-lived resonance production in relativistic heavy ion collisions provide an unique tool to estimate the time scale between the chemical and kinetic freeze-outs due to the resonance decay daughters' re-scattering effect in the hadronic gas medium [28, 36].

In principle, the resonance decay daughters' re-scattering effect destroys a portion of the resonance signals and the re-generation effect in the hadron medium produces a part of the resonance signals. Both the re-scattering effect and the re-generation effect may happen in the hadron gas medium between the chemical and kinetic freeze-outs. Technically, in order to estimate the time scale, the resonance particle we choose should fulfill one of the following two conditions: (1) resonance signals destroyed by the re-scattering effect are much more than the signals produced by the re-generation effect; (2) the signals produced by the re-generation effect are much more than the signals destroyed by the re-scattering effect. If there is no significant difference between the amounts of resonance signals destroyed and produced, we cannot estimate the time scale.

Thus the $K^*(892)$ resonance is a good candidate to estimate the time scale because it fulfills condition (1). The K^* lifetime is extremely small so that a large portion of the K^* signals may decay inside the hadron medium. Its pion decay daughter's interaction cross section with the pions in the hadron medium is relatively large. Thus we expect to have a large amount of the K^* signals destroyed by its daughter particles' re-scattering effect. On the other hand, the interaction cross section for the kaon and pion particles in the hadron medium to re-generate the K^* signals is relatively small and the number of kaons in the hadron medium is much smaller than the number of pions [37]. Thus we do not expect to have a strong re-generation effect to produce the K^* signals in the hadron medium.

Another good candidate is the ρ^0 resonance via its di-leptonic decay channel $\rho^0 \rightarrow e^+e^-$ which agrees with condition (2). Details will be discussed in Section 1.2.6.

1.2.5 UrQMD Transport Model

The Ultra-relativistic Quantum Molecular Dynamics model (UrQMD [28]) is a microscopic transport approach based on the covariant propagation of constituent quarks and di-quarks accompanied by mesonic and baryonic degrees of freedom. It simulates

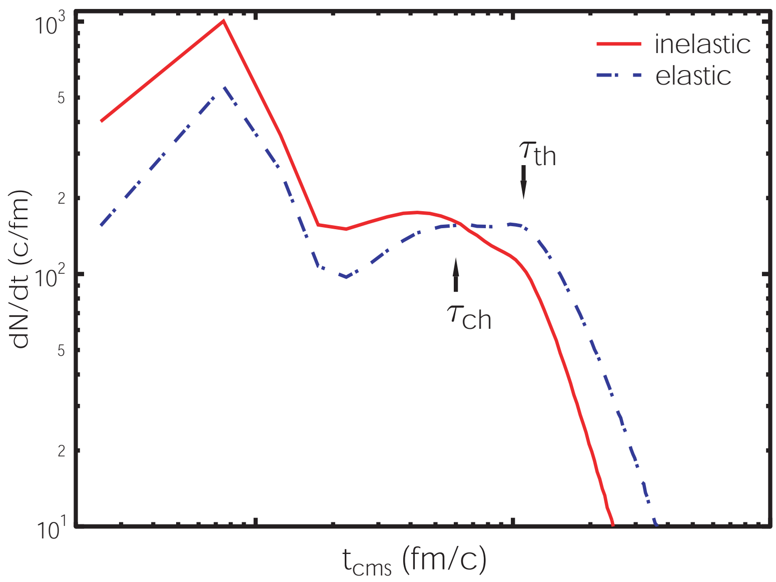

Figure 1.6: Inelastic and (pseudo-)elastic collision rates in Pb+Pb at 160A GeV. τ_{ch} and τ_{th} denote the chemical and thermal/kinetic freeze-out as given by the microscopic reaction dynamics of UrQMD. Figure is taken from [28].

multiple interactions of ingoing and newly produced particles, the excitation and fragmentation of color strings and the formation and decay of hadronic resonances [28]. In the UrQMD model, two different kinds of freeze-outs, the chemical freeze-out and the thermal/kinetic freeze-out, happen sequentially at different temperatures ($T_{\rm ch} \approx$ 160 - 170 MeV, $T_{\rm th} \approx$ 120 MeV) and thus at different times. Before the chemical freeze-out stage, the flavor and chemistry changing inelastic processes (e.g. $\pi\pi \to K\overline{K}$) are dominant. Between the chemical freeze-out and the kinetic freeze-out, the elastic collisions, which consist of two components: the true elastic processes (e.g. $\pi\pi \to \pi\pi$) and the pseudo-elastic processes (e.g. $K\pi \to K^* \to K\pi$), exceed the inelastic processes [28] .

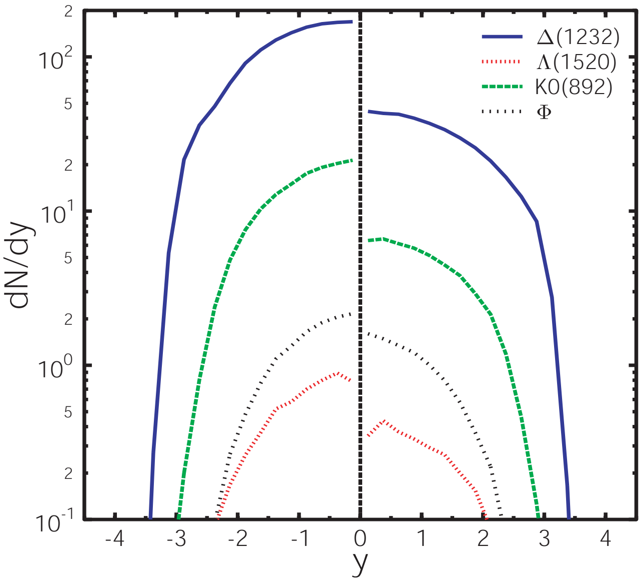

Figure 1.7: Rapidity densities for $\Delta(1232)$, $\Lambda^*(1520)$, $K^{*0}(892)$ and ϕ in Pb+Pb at 160A GeV collisions. Left: All resonances as they decay. Right: Reconstructable resonances. Figure is taken from [28].

Figure 1.6 shows the time evolution of the elastic and inelastic collision rates in Pb+Pb at 160 A GeV from the UrQMD model calculation. However, since there is a separation between the different freeze-outs, a part of the resonance daughters re-scatter, and therefore are unobservable in the final state. The pseudo-inelastic processes which happen between the potential resonance daughters can produce a part of the resonance signals. Using the UrQMD model calculation and considering the above two kinds of processes, Figure 1.7 shows the rapidity densities for the $\Delta(1232)$, $\Lambda^*(1520)$, $K^{*0}(892)$ and ϕ in Pb+Pb at 160A GeV collisions. From this figure, we can see that the resonance daughter particles' re-scattering effect in the hadron medium drastically lowered the observable yields of resonances as compared to the primordial yields at chemical freeze-out. However, this daughter particles' re-scattering effect lowering of the resonance yields has p_T dependence. Resonances with higher p_T have a larger chance to escape the hadron medium and thus avoid the re-scattering effect than the resonances with lower p_T. Figure 1.8 directly addresses the p_T dependence of the observability of resonances. The UrQMD model study supports a strong p_T dependence of the re-scattering probabilities. This effect should lead to a larger apparent temperature (inverse slope parameter) for resonances reconstructed from strongly interacting particles [28].

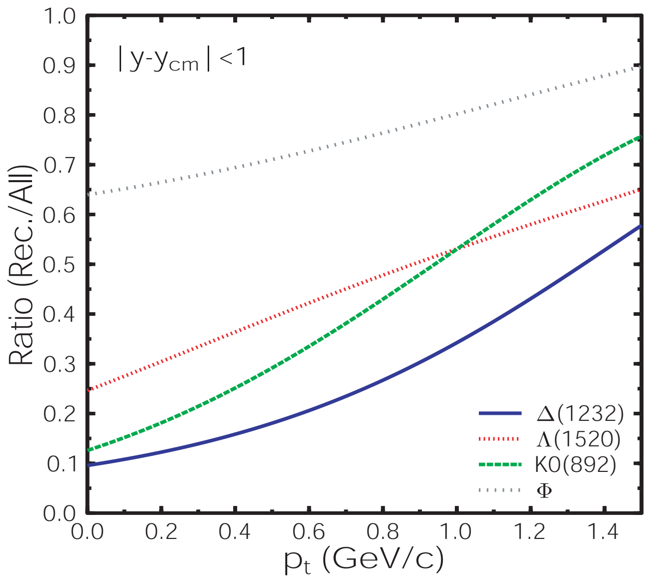

Figure 1.8: Ratio R of reconstructable resonances over all resonances of a given type as a function of transverse momentum for $\Delta(1232)$, $\Lambda^*(1520)$, $K^{*0}(892)$ and ϕ in Pb+Pb at 160A GeV collisions. Figure is taken from [28].

1.2.6 Resonance Di-Lepton Decay Channel

Besides the hadronic decay channel, some quarkonium resonance mesons which have quark content $q\overline{q}$ can decay in the di-leptonic channel, such as $\rho \to e^+e^-$, $\phi \to \mu^+\mu^-$. In the hadron medium phase between chemical and kinetic freeze-out, hadronic decay daughters might be re-scattered by the particles in the hadron medium and thus a portion of the total resonance signals might be lost. But the resonance leptonic decay daughters will very rarely be re-scattered by the hadronic medium since the lepton-hadron interaction cross sections are much smaller than the hadron-hadron interaction cross sections. Thus by measuring the resonance through the di-leptonic decay channel, in principle we expect to measure all the resonance yield [38].

Recently, the ϕ meson production has been measured in central Pb+Pb collisions at 158A GeV at the CERN/SPS. The NA49 Collaboration [39] has identified the ϕ meson via the decay channel $\phi \to K^+K^-$, while the NA50 Collaboration [40] measured it using $\phi \to \mu^+\mu^-$ decay. It was found that the extracted number of ϕ mesons from the di-muon channel exceeds by a factor between two and four the number extracted from the K^+K^- channel. This difference has been attributed to the fact that not all ϕ mesons can be reconstructed from the K^+K^- channel resulting from their decay daughters re-scattering effect in the hadronic matter [38].

In the STAR Collaboration, we have successfully measured the ρ^0 resonance production via the $\rho^0 \to \pi^+\pi^-$ decay channel [19]. With the full coverage Time Of Flight (TOF) detector being installed in the next several years, electron signals are expected to be identified with a combination of the TPC and the TOF detector [11, 41]. Thus it will be possible for us to measure the ρ^0 resonance di-electron decay channel $\rho^0 \to e^+e^-$ [42]. Due to the same reason addressed in the above, we expect to see that the ρ^0 meson yield extracted via the di-electron channel exceeds that via the hadronic decay channel.

Besides giving supporting evidence to the existence of the resonance hadronic decay daughters' re-scattering effect in the hadronic medium, the ρ^0 meson measured via the di-leptonic channel can be used to probe the following two physics topics: (1) to verify the resonance in-medium effects which modify the resonance properties (mass, width and line shape) [19]; (2) to estimate the upper limit of the time scale between

the chemical and kinetic freeze-outs.
As discussed in Section 1.2.2, resonance particles in the hot-dense medium would face the in-medium effect thus the resonance mass, width and even the line shape might be changed. In the STAR Collaboration, the resonance mass and width distributions have been measured for $\rho^0 \rightarrow \pi^+\pi^-$, $K^{*0} \rightarrow K^+\pi^-$ and $\Delta^{++} \rightarrow p\pi^+$ and their downward mass shifts have been observed in Au+Au and p+p collisions at $\sqrt{s_{NN}}$=200 GeV. This mass shift is evidence of an in-medium effect in the hot-dense medium. However, we may also need the resonance di-leptonic decay channel measurements to verify the resonance in-medium effect [18, 19, 21].
As discussed in Section 1.2.4, we might be able to use the K^* resonance production and the K^*/K ratios to estimate the lower limit of the time scale between the chemical and kinetic freeze-outs since the K^* hadronic daughters' re-scattering effect is much stronger than the re-generation effect. In fact, although the kaon and pion interaction cross section is small, we still cannot totally ignore this kaon and pion re-generation effect to produce the K^* signals. Thus we can only estimate the lower limit of the time scale by measuring the K^*/K ratio. Fortunately, we might be able to use the resonance di-leptonic decay channel to estimate the upper limit of the time scale since leptonic decay daughter can be very hardly re-scattered by the hadron medium. In the case of $\rho^0 \rightarrow e^+e^-$, the ρ^0 signals can be re-generated through the $\pi^+\pi^-$ interaction in the hadronic medium and the ρ^0 resonance leptonic daughters cannot be destroyed by the re-scattering effect. Then the ρ^0 yield extracted from the di-leptonic decay channel is expected to increase as a function of the time between chemical and kinetic freeze-outs. Thus by measuring the ρ/π ratio via its di-leptonic channel and compared to that from the hadronic channel, it may enable us to estimate the upper limit of the time scale between chemical and kinetic freeze-outs.

Chapter 2

The STAR Experiment

2.1 The RHIC Accelerator

The Relativistic Heavy Ion Collider (RHIC) at Brookhaven National Lab (BNL) is the first collider to accelerate two counter-rotating heavy ion beams and is capable of accelerating any combination of ion species, such as p+p, d+Au, Au+Au and so on, with the colliding center-of-mass energy per nucleon-nucleon pair at $\sqrt{s_{NN}} = 200$ GeV. Each ion can be accelerated to 99.995% the speed of light ($v = 0.99995c$). The RHIC facility consists of two super-conducting magnets, each with a circumference of 2.4 miles, which focus and guide the beams. RHIC is designed for a Au+Au collision luminosity of about $2{\times}10^{26}$ cm^{-2}sec^{-1} at top energy, while maintaining the potential for future upgrades by an order of magnitude [43].

Figure 2.1 shows the BNL accelerator complex including the accelerators used to bring the gold ions up to RHIC injection energy. First, gold ions are generated and accelerated to 15 MeV/nucleon in the Tandem Van de Graaff facility. Then the gold beam is transferred to the booster where it is accelerated to 95 MeV/nucleon. In the AGS, the gold beam is bunched and further accelerated to 10.8 GeV/nucleon. Once the gold beam is injected into the two counter-rotating rings of RHIC, the bunches are accelerated to collision energy (100GeV/nucleon) and stored for data taking. Usually the ring with a clock-wise rotating beam is called the Blue Ring and the ring with a counter-clock-wise rotating beam is called the Yellow Ring [43].

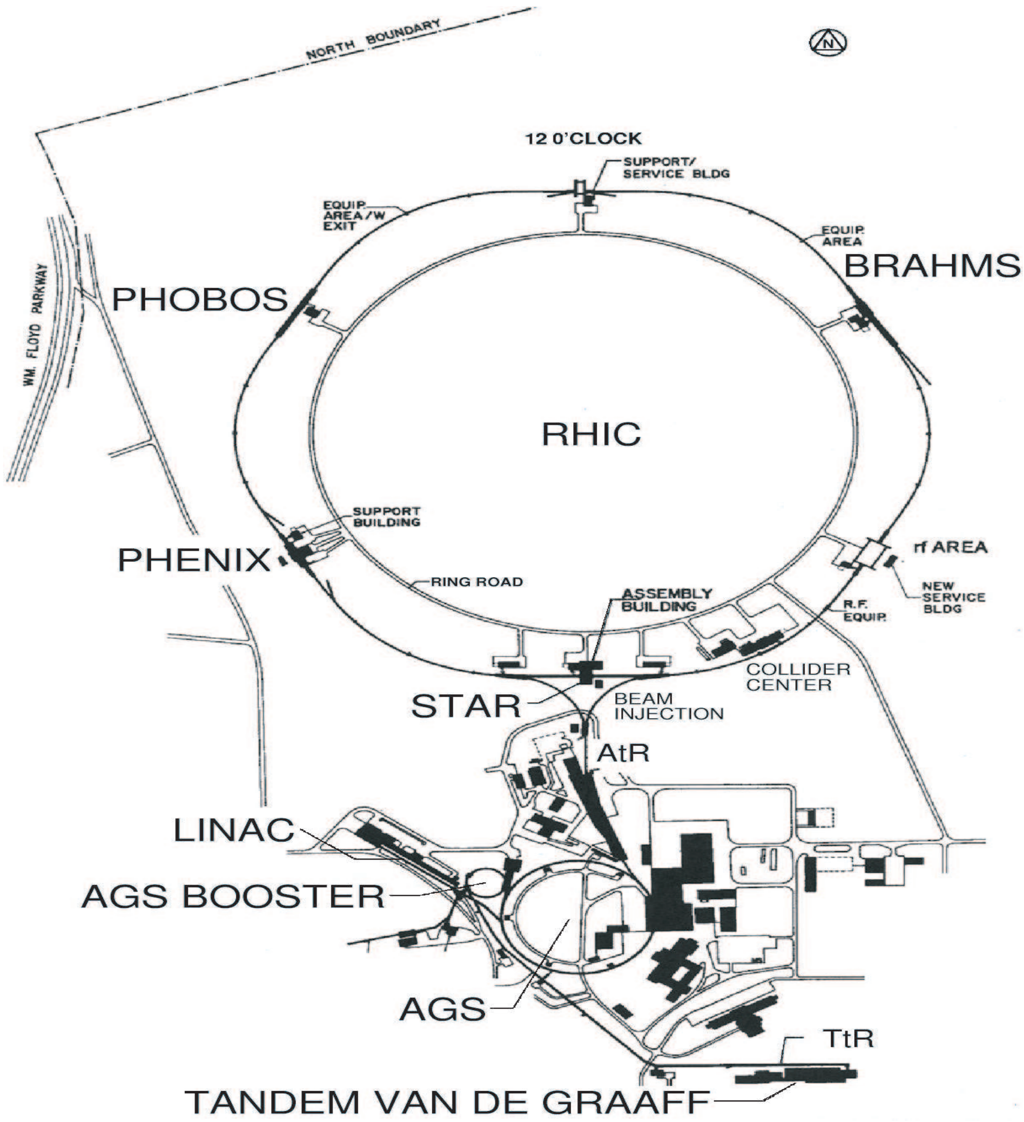

Figure 2.1: A disgram of the Brookhaven National Laboratory collider complex including the accelerators that bring the nuclear ions up to RHIC injection energy (10.8 GeV/nucleon for ^{197}Au). Figure is taken from [44].

RHIC has six interaction points with 4 of them currently occupied: the STAR experiment at the 6 o'clock point; the PHENIX experiment at the 8 o'clock point; the PHOBOS experiment at the 10 o'clock point; the BRAHMS experiment at the 2 o'clock point.

2.2 Van der Meer Scan and Cross Section Measurement

The interaction cross section as a function of transverse energy E_T or charge multiplicity N_{ch} is one of the necessary global event features for specifying the parameters of the initial state in relativistic heavy ion collisions [45]. The Van der Meer Scan (also known as Vernier Scan) is used to determine the luminosity and the total absolute cross section.

The Van der Meer Scan was invented by S. van der Meer in 1968 who showed that it is possible to measure the effective height h_e of the colliding ISR beams by observing the counting rate R in a suitable monitor system while sweeping the two beams vertically through each other [46]. At RHIC, the beams are bunched and cogged with zero crossing angle at the interaction point. STAR used the ZDC (Zero Degree Calorimeter) to measure the neutrons emitted from nuclear fragments from Au+Au collisions that missed the actual interaction zone [47]. The interation rate N_{ZDC} is defined as the numbers of the beam particles (N_{b1} and N_{b2}) going through each other in some area A with cross section σ [48, 49]

$$N_{ZDC} = \frac{N_{b1}N_{b2}}{A}\sigma = L\sigma \tag{2.1}$$

For two beams (Blue and Yellow in our case) with Gaussian distribution $\rho(x, y)$ in both horizontal and vertical directions, we have the luminosity L as

$$L = f_{rev}\int_{-\infty}^{+\infty}\int_{-\infty}^{+\infty}\rho_1(x, y)\rho_2(x, y)dxdy \tag{2.2}$$

where f_{rev} is the revolution frequency (7.8×10^4 Hz),

$$\rho_i = N_i\frac{1}{\sqrt{2\pi}\sigma_{xi}}\exp[-\frac{x^2}{2\sigma_{xi}^2}]\frac{1}{\sqrt{2\pi}\sigma_{yi}}\exp[-\frac{y^2}{2\sigma_{yi}^2}] \tag{2.3}$$

with $i = 1, 2$ for blue and yellow beams respectively and N_i are number of particles per bunch assuming all bunches in one beam are the same. Integrating over x and y, the luminosity is given by

$$L = \frac{f_{rev} N_1 N_2}{2\pi\sqrt{(\sigma_{x1}^2 + \sigma_{x2}^2)(\sigma_{y1}^2 + \sigma_{y2}^2)}} \tag{2.4}$$

If one beam is displaced by d in the x direction, we have

$$\rho_1 = N_1 \frac{1}{\sqrt{2\pi}\sigma_{x1}} \exp[-\frac{(x-d)^2}{2\sigma_{x1}^2}] \frac{1}{\sqrt{2\pi}\sigma_{y1}} \exp[-\frac{y^2}{2\sigma_{y1}^2}] \tag{2.5}$$

Then the luminosity $L(d)$ as a function of d is

$$L = \frac{f_{rev} N_1 N_2}{2\pi\sqrt{(\sigma_{x1}^2 + \sigma_{x2}^2)(\sigma_{y1}^2 + \sigma_{y2}^2)}} \exp[-\frac{d^2}{2(\sigma_{x1}^2 + \sigma_{x2}^2)}] \tag{2.6}$$

Now we can see that the luminosity $L(d)$ is a Gaussian distribution as a function of the displacement d and the width ($\sqrt{\sigma_{x1}^2 + \sigma_{x2}^2}$) of the Gaussian distribution from Vernier Scan is the width required in luminosity calculation. Thus by measuring the interaction rate N_{ZDC} for different beam displacement d in the x or y direction respectively, we can determine the beam profile σ_{Vx} and σ_{Vy}, where

$$\sigma_{Vx} = \sqrt{\sigma_{x1}^2 + \sigma_{x2}^2} \tag{2.7}$$

$$\sigma_{Vy} = \sqrt{\sigma_{y1}^2 + \sigma_{y2}^2} \tag{2.8}$$

From Equation 2.4, we know that we have to measure beam currents (N_1, N_2) and beam profiles $(\sigma_{Vx}, \sigma_{Vy})$ for a certain number of bunches k_b in the beam. The total beam intensity is measured by sensitive "DC" transformer and the bunched beam intensity is measured with a wideband wall current pickup [49]. The beam profile is measured by the van der Meer Scan described above. There are two Beam Position Monitors (BPM) [49] in each side of the interaction point measuring the Yellow and Blue beam x and y positions, respectively. Because the beam intensities in both Blue and Yellow rings decrease as a function of time, we normalize the ZDC counts with the beam intensities as $N_{ZDC}/(N_1N_2)$ to cancel out this effect. Thus the absolute cross section in Au+Au collisions with zero beam displacement is

$$\sigma_{Au+Au} = (\frac{N_{ZDC}}{N_1N_2})\frac{2\pi k_b \sigma_{Vx}\sigma_{Vy}}{f_{rev}} \tag{2.9}$$

where k_b is the number of bunches in a beam (k_b =55).

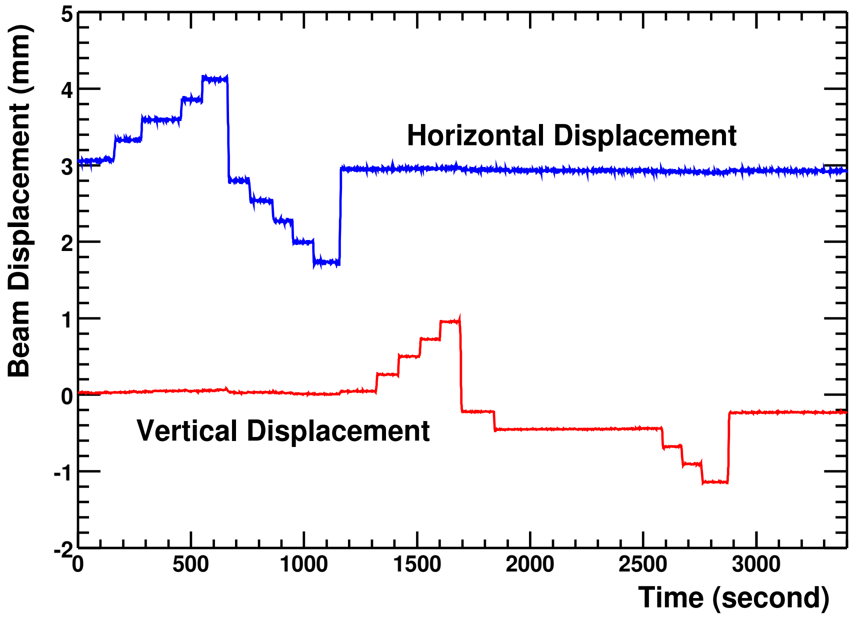

Figure 2.2: The BPM measured Blue beam horizontal and vertical position as a function of time for the scan Vernier3 at the STAR interaction point.

There is at least one Vernier Scan carried out for each interaction point. At the STAR interaction point, we have three carefully measured scans. The three scans are Vernier1 (beginning at September 21st, 2001, 15:17), Vernier2 (beginning at October 22nd, 2001, 15:50) and Vernier3 (beginning at November 15th, 2001, 21:14). For each beam horizontal and vertical set position, we recorded the beam intensities of both beams, the beams' horizontal and vertical positions, ZDC counts averaging over one minute and the time of the measurement.

Figure 2.2 shows the BPM measured Blue beam horizontal and vertical position as a function of time for the scan Vernier3 at the STAR interaction point. This scan was performed by setting the correcting magnet to steer the beam to the desired position

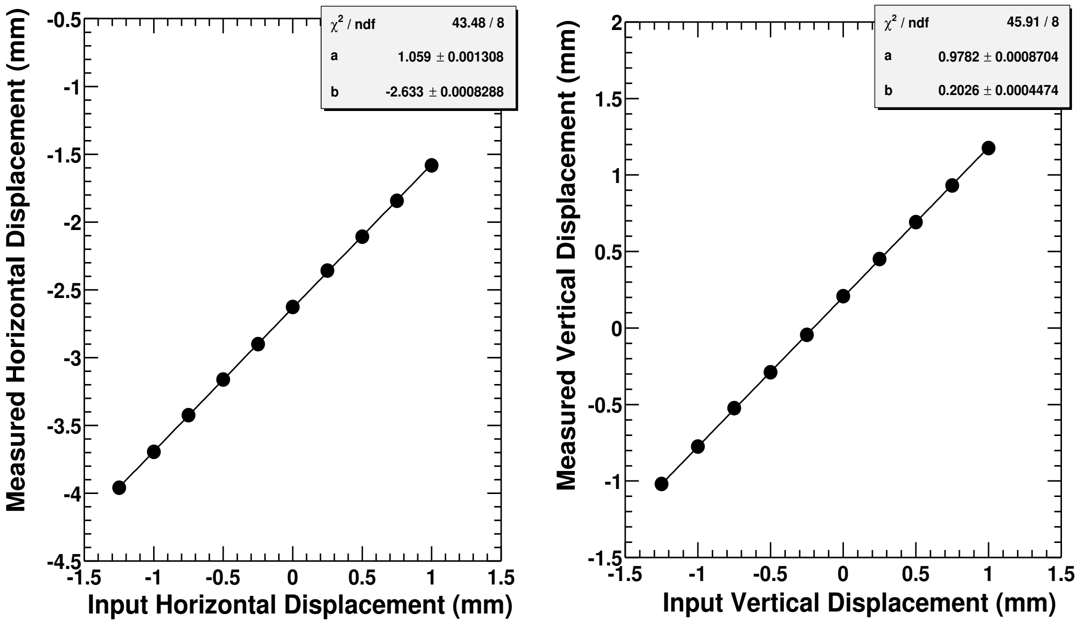

Figure 2.3: The BPM measured beam horizontal (left) and vertical (right) position (average of Blue and Yellow beams) vs. the set beam position for the scan Vernier3 and fit with a linear function $y = ax + b$.

with each step 250 μm. Figure 2.3 shows the BPM measured beam horizontal and vertical position vs. the set beam position and fit with a linear function. From this figure, we can see that the measured beam positions are well calibrated and have a resolution in the order of 10 μm.

Figure 2.4 shows the calculated $N_{ZDC}/(N_1N_2)$ (in unit of 10^{-18}Hz) vs. the beam horizontal and vertical positions and fit with a Gaussian function plus a constant representing any possible background. From the fit, we can extrapolate the beam profiles $\sigma_{Vx} = 361 \pm 6$ μm and $\sigma_{Vy} = 345 \pm 6$ μm.

Using Equation 2.9, the raw Au+Au total cross section can be calculated as 9.05 $\pm$ 0.22 barn. Since not all bunches in both beams are equally filled with particles, the raw total cross section is then corrected with the fill pattern [49]. By averaging the corrected total cross sections measured with all scans, we get the final Au+Au inclusive double neutron disassociation cross section $\sigma_{\mathrm{Au+Au}} = 9.8 \pm 0.2 \pm 1.2$ barn at collision energy $\sqrt{s_{NN}} = 200$ GeV.

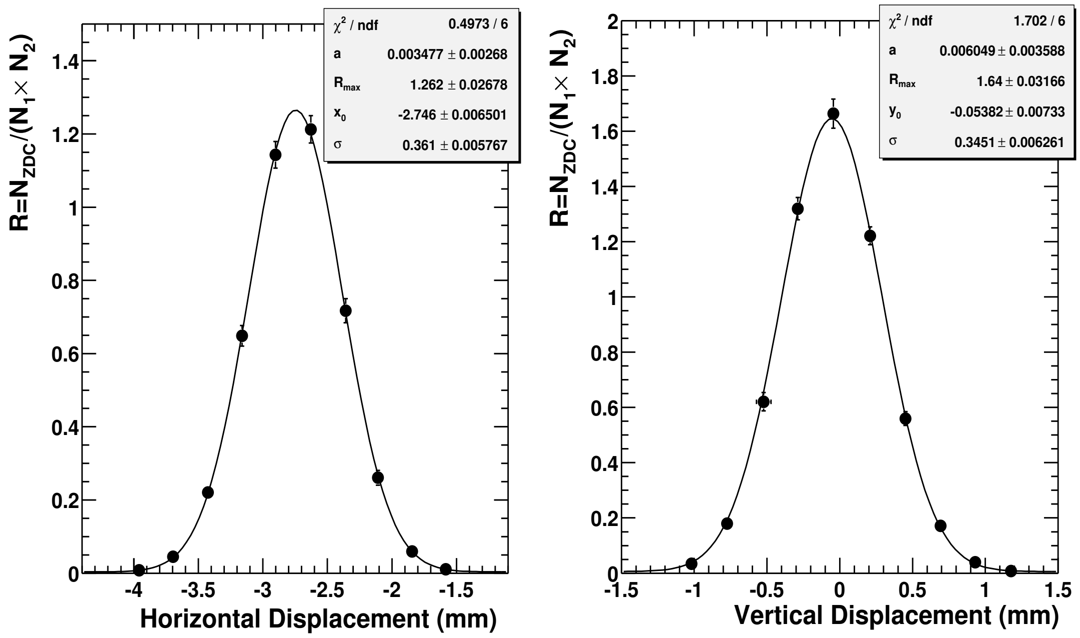

Figure 2.4: The R ($= N_{ZDC}/(N_1N_2)$) vs. the measured beam horizontal (left) and vertical (right) position and fit with a Gaussian function $R = a + R_{max}\exp[-(x - x_0)^2/2\sigma^2]$.

2.3 The STAR Detector

The Solenoidal Tracker at RHIC (STAR) is one of the two large detector systems constructed at the Relativistic Heavy Ion Collider (RHIC) at Brookhaven National Laboratory. It was constructed to investigate the behavior of strongly interacting matter at high energy density and to search for signatures of quark gluon plasma (QGP) formation. STAR can measure many observables simultaneously to study signatures of a possible QGP phase transition and to understand the space-time evolution of the collision process in relativistic heavy ion collisions. The goal is to obtain a fundamental understanding of the microscopic structure of these hadronic interactions at high energy densities. In order to accomplish this, STAR was designed primarily for measurements of hadron production over a large solid angle, featuring detector systems for high precision tracking, momentum analysis, and particle identification at the center of mass rapidity. The large acceptance of STAR makes

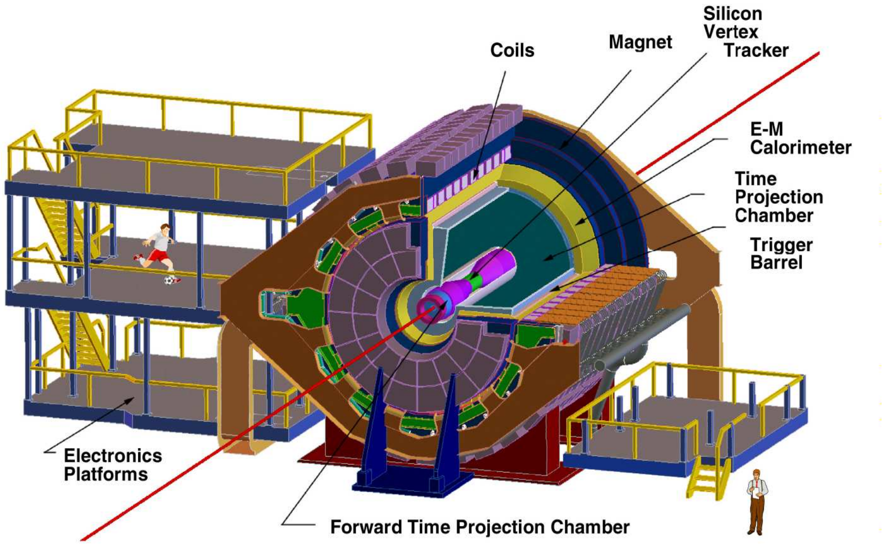

Figure 2.5: Perspective view of the STAR detector, with a cutaway for viewing inner detector systems. Figure is taken from [50].

it particularly well suited for event-by-event characterizations of heavy ion collisions and for the detection of hadron jets [50].

The layout of the STAR detector is shown in Figure 2.5. A cutaway side of the STAR detector as configured for the RHIC 2001 run is displayed in Figure 2.6. A large volume Time Projection Chamber (TPC) for charged particle tracking and particle identification is located at a radial distance from 50 to 200 cm from the beam axis. The TPC is 4 meters long and it covers a pseudo-rapidity range $|\eta| \leq 1.8$ for tracking with complete azimuthal symmetry ($\Delta\phi = 2\pi$). A solenoidal magnet with a maximum magnetic field of 0.5 T provides a uniform magnetic field for charged particle momentum analysis. Charged particle tracking close to the interaction region is accomplished by a Silicon Vertex Tracker (SVT) consisting of 216 silicon drift detectors. To extend the tracking to the forward region, a radial-drift Forward TPC (FTPC) is installed covering $2.5 < |\eta| < 4$, also with complete azimuthal coverage and symmetry. To extend the particle identification in STAR to larger momenta, a ring imaging Cherenkov detector (RICH) covers $|\eta| < 0.3$ and $\Delta\phi = 0.11\pi$ is installed [50].

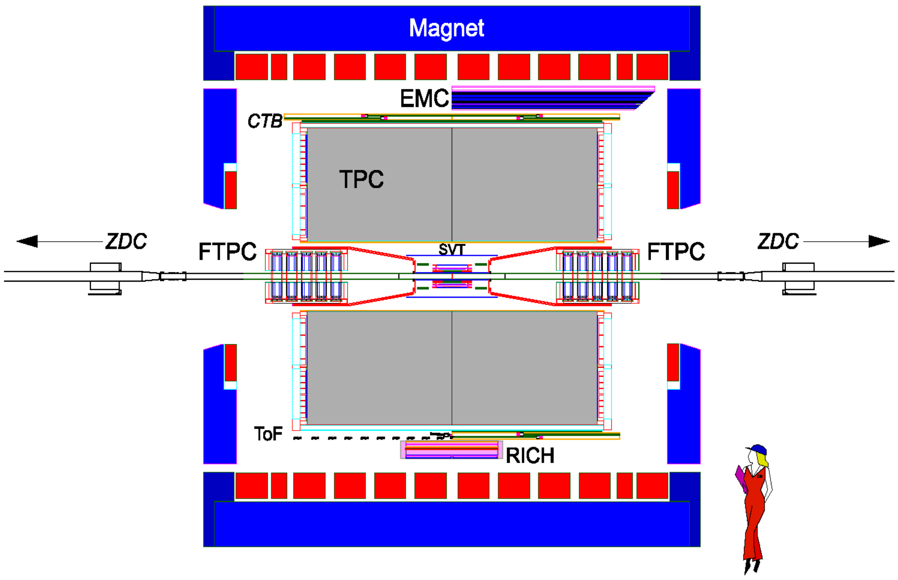

Figure 2.6: Cutaway side view of the STAR detector. Figure is taken from [50]

The fast detectors that provide input to the trigger system are a central trigger barrel (CTB) at $|\eta| < 1$ and two zero-degree calorimeters (ZDC) located in the forward directions at $\theta < 2$ mrad. The CTB surrounds the outer cylinder of the TPC, and triggers on the flux of charged particles in the mid-rapidity region. The ZDCs are used for determining the energy in neutral particles remaining in the forward directions [50]. Besides, two Beam-Beam Counters (BBC) which measure the charged particle multiplicity near beam rapidity are used to define the trigger in p+p collisions.

2.3.1 The Time Projection Chamber

The STAR detector uses the TPC as its primary tracking device. The TPC records the tracks of charged particles, measures their momenta, and identifies the particles by measuring their ionization energy loss (dE/dx). Its acceptance covers ±1.8 units of pseudo-rapidity through the full azimuthal angle and over the full range of multiplicities. Particles are identified over a momentum range from 100 MeV/c to greater than 1 GeV/c and momenta are measured over a range of 100 MeV/c to 30

GeV/c [51].

The STAR TPC is shown schematically in Figure 2.7. It is an empty volume of gas in a well defined uniform electric field of ≈ 135 V/cm. The uniform electric field which is required to drift the electrons and is defined by a thin conductive Central Membrane (CM) at the center of the TPC, concentric field cage cylinders and the

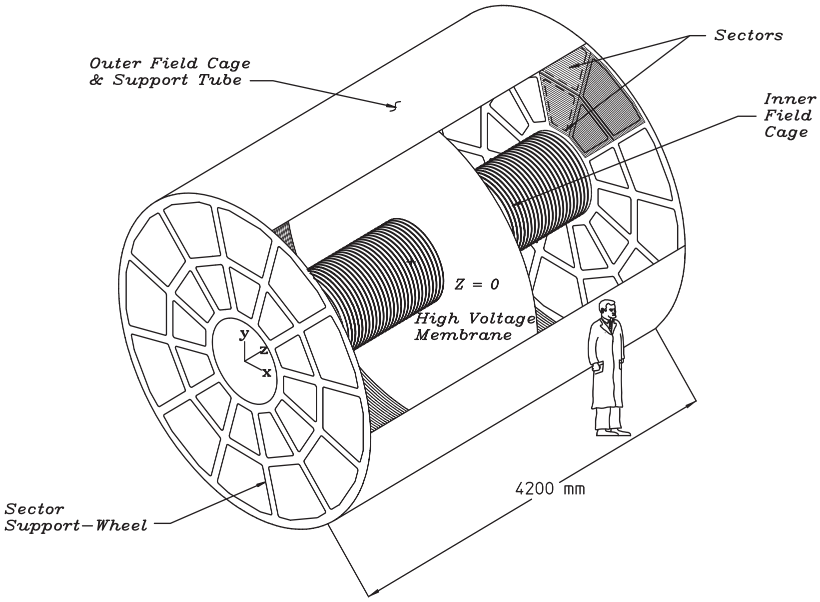

Figure 2.7: The STAR TPC surrounds a beam-beam interaction region at RHIC. The collisions take place near the center of the TPC. Figure is taken from [51].

readout end caps. The TPC is a fully pixelized drift chamber with a Multi-Wire Proportional Chamber (MWPC) at both ends of the TPC for readout. The TPC has 144,000 pads which give x-y coordinate information and up to 512 time buckets which provide z-position information for each hit, a total of 70 million pixels. The TPC is filled with P10 gas (10% methane, 90% argon) regulated at 2 mbar above atmospheric pressure. It's primary attribute is a fast drift velocity which peaks a t a low electric field [51].

Charged particles can be detected in drift chambers because they ionize the gas along their flight path. The energy required for ionization is very small, typically a few keV per cm. When a charged particle traverses the TPC volume, it ionizes on average gas atoms and molecules every few tenths of a millimeter along its path and leaves behind a cluster of electrons. Under the influence of an externally applied electric field, the electron clusters then drift at a constant average velocity to the readout electronics where their time of arrival and location are recorded.

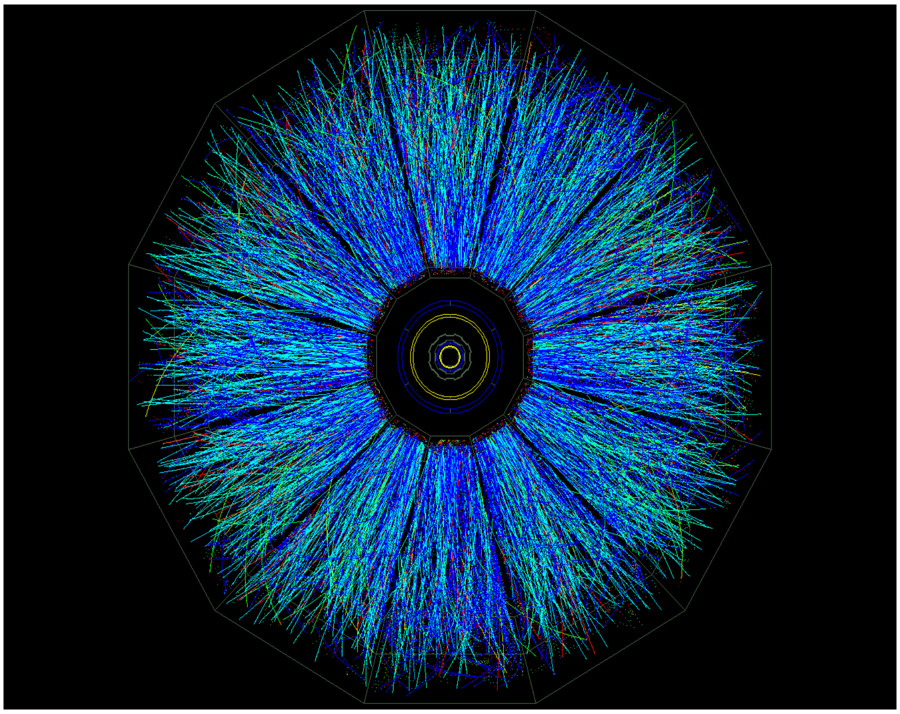

Figure 2.8: Beam's eye view of a central Au+Au collision event in the STAR Time Projection Chamber. This event was drawn by the STAR online display. Figure is taken from [50].

At the Data Acquisition (DAQ) stage, raw events containing millions of ADC values were recorded to tapes. Raw data were then reconstructed into meaningful quantities such as hits, tracks, vertices, etc. In the event reconstruction stage, starting from the hit with the lowest track density at the outer wall of the TPC, the Kalman Filter method is used to fit the hits in a uniform magnetic field to form a global track. Once all the global tracks in an event are reconstructed, the trajectories of selected global tracks are extrapolated to the beam axis to be at $x = y = 0$ and thus the z position of the primary collision vertex of this event is found. Then the global tracks with a

3-dimensional distance of closest approach (DCA) to the primary vertex less than 3 cm are chosen for a re-fit by forcing a new track helix ending at the primary vertex. These newly reconstructed helices are called primary tracks. Figure 2.8 shows the beam's eye view of a central Au+Au collision event in the STAR TPC.

2.3.2 Particle Identification (PID)

Charged tracks passing through the TPC will lose energy via ionization. The total ionized charges collected from each hit on a track are proportional to the energy loss of the particle. For a particle with charge Z (in units of e) and speed $\beta = v/c$ passing through a medium with density ρ, the mean energy loss it suffers can be described by the Bethe-Bloch formula

$$\langle\frac{dE}{dx}\rangle = 2\pi N_0 r_e^2 m_e c^2 \rho \frac{Zz^2}{A\beta^2}[\ln\frac{2m_e\gamma^2 v^2 E_M}{I^2} - 2\beta^2] \tag{2.10}$$

where N_0 is Avogadro's number, m_e is the electron mass, r_e $(= e^2/m_e)$ is the classical electron radius, c is the speed of light, z is the atomic number of the absorbing material, A is the atomic weight of the absorbing material, $\gamma = 1/\sqrt{1-\beta^2}$, I is the mean excitation energy, and E_M $(= 2m_e c^2\beta^2/(1-\beta^2))$ is the maximum transferable energy in a single collision [52].

From the above equation, we can see that different charged particles (electron, pion, kaon, proton or deuteron) with the same momentum p passing through the TPC gas can cause different amount of mean energy loss. Figure 2.9 shows the negatively charged particles' energy loss dE/dx vs. momentum p. We can see that different charged particles have their own dE/dx vs. p band in the figure. Thus we can use the energy loss in the TPC to identify different charged particle types. Qualitatively speaking, from the above figure, we can identify charged pions and kaons with momentum up to about 0.75 GeV/c and identify protons and anti-protons with momentum up to about 1.1 GeV/c.

In order to quantitatively describe the particle identification, we define the variable $N_{\sigma\pi}$ (in the case of charged pion identification) as

$$N_{\sigma\pi} = [\frac{dE}{dx}_{meas.} - \langle\frac{dE}{dx}\rangle_\pi]/[\frac{0.55}{\sqrt{N}}\frac{dE}{dx}_{meas.}] \tag{2.11}$$

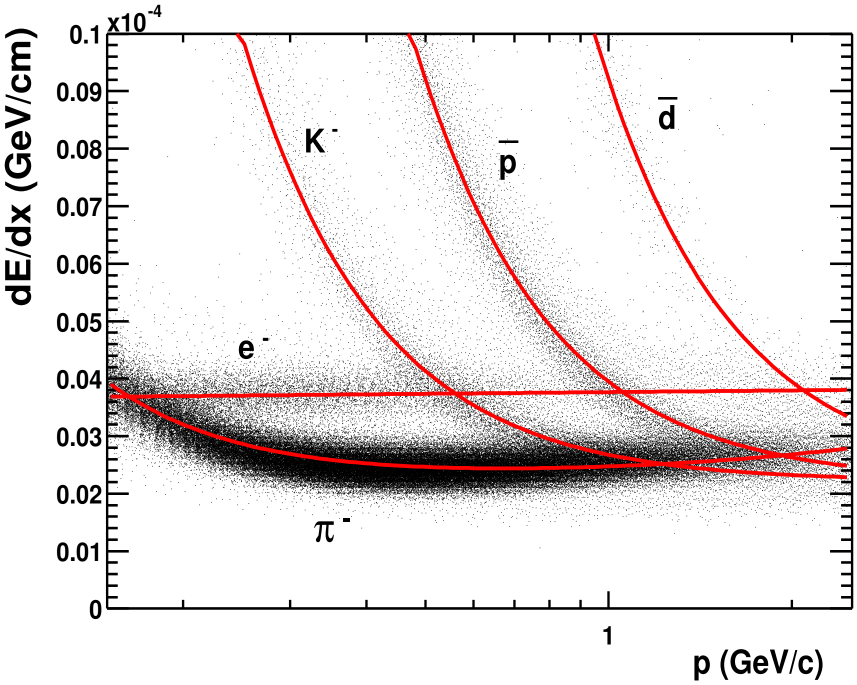

Figure 2.9: Negatively charged particles' ionization energy loss vs. momentum in TPC. The curves are the Bethe-Bloch function shown in Equation 2.10 for different particle species.

in which N is the number of hits for a track in the TPC, $\frac{dE}{dx}_{meas.}$ is the measured energy loss of a track and $\langle \frac{dE}{dx} \rangle_\pi$ is the mean energy loss for charged pions. In order to identify charged kaons, protons and anti-protons, we can have similar definition of $N_{\sigma K}$ and $N_{\sigma p}$. Thus we can cut on the variables $N_{\sigma\pi}$, $N_{\sigma K}$ and $N_{\sigma p}$ to select different particle species.

A specific part of the particle identification is the topological identification of neutral particles, such as the K_S^0 and Λ. These neutral particles can be reconstructed by identifying the secondary vertex, commonly called V0 vertex, of their charged daughter decay modes, $K_S^0 \to \pi^+\pi^-$ and $\Lambda \to p\pi^-$.

Chapter 3

Analysis Methods

3.1 Trigger

During the second RHIC run (2001-2002), RHIC performed Au+Au and p+p collisions at a nucleon-nucleon center-of-mass energy of $\sqrt{s_{NN}}$ = 200GeV. In the STAR detector, the experimental setup consisted of a Time Projection Chamber (TPC),

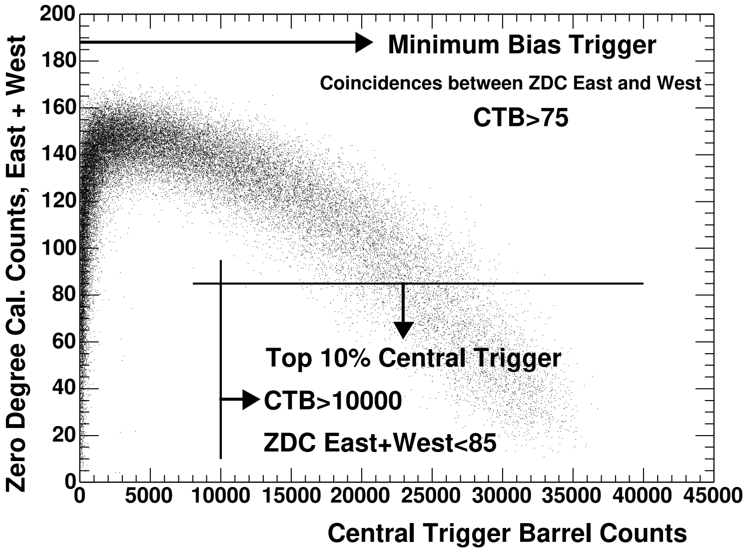

Figure 3.1: The ZDC (sum of East and West calorimeters) signal vs. the corresponding CTB signal in Au+Au collisions at $\sqrt{s_{NN}}$=200GeV.

a Central Trigger Barrel (CTB), a pair of Beam-Beam Counters (BBC) and two Zero Degree Calorimeters (ZDC) located upstream along the beam axis. The large solenoidal magnet provided a magnetic field of 0.5 Tesla.

In Au+Au collisions, the minimum bias trigger was defined by requiring greater than 75 CTB counts and coincidences between the two ZDC's which measured the spectator neutrons. CTB counts fewer than 75 together with coincidences between two ZDC's defined an Ultra-Peripheral Collision (UPC) trigger. Figure 3.1 shows the sum of the east and west ZDC counts vs. the CTB counts in Au+Au collisions at $\sqrt{s_{NN}}$=200GeV. Greater than 10,000 CTB counts and the sum of east and west ZDC counts less than 75 were required to trigger the top 10% central Au+Au collision events. In p+p collisions, the minimum bias trigger was defined using coincidences between two BBC's. The cross section of minimum p+p collisions is 31±3 mb while the total inelastic p+p collision cross section is 42 mb.

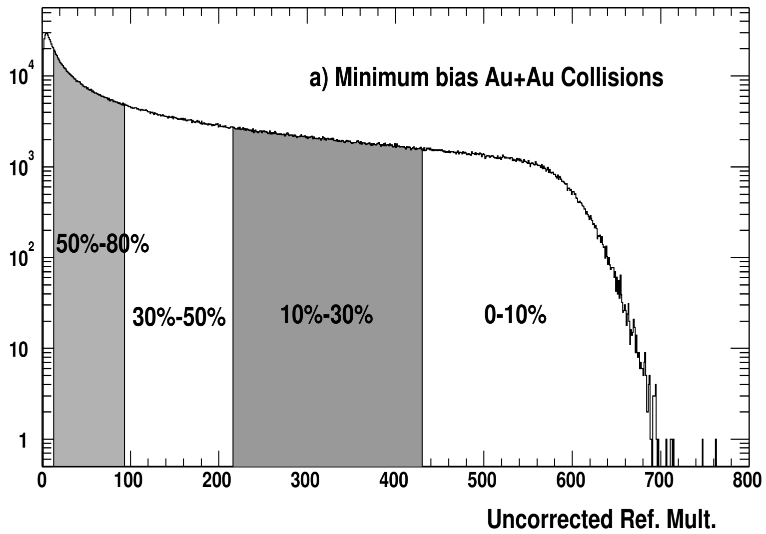

Figure 3.2: The uncorrected reference multiplicity distribution for minimum bias triggered Au+Au collision events. The four centrality regions used in this analysis are shown.

3.2 Event Selection

To roughly achieve uniform acceptance in the pseudo-rapidity range, the collision vertex was required to be within ±50cm along the beam line. About 2M top 10% central triggered and 2M minimum bias triggered Au+Au collision events and 6M minimum bias triggered p+p collision events were used in this analysis.
Figure 3.2 shows the uncorrected reference multiplicity distribution from minimum bias triggered Au+Au collisions. The reference multiplicity was defined as the number of charged primary tracks in a pseudo-rapidity (η) range $-0.5 < \eta < 0.5$ in each collision event. According to this uncorrected reference multiplicity, the events from minimum bias Au+Au collisions were then divided into four centrality bins from the most central to peripheral collisions: 0%-10%, 10%-30%, 30%-50% and 50%-80%. Table 3.1 lists the uncorrected reference multiplicity ranges for centrality definitions.

Centrality Bin	Uncorr. RefMult Range	Uncorr. N_{charge}	Corrected N_{charge}
0%-10%	RefMult $\geq$ 431	511.4	620.4
10%-30%	217 $\leq$ RefMult $<$ 431	313.7	354.0
30%-50%	94 $\leq$ RefMult $<$ 217	148.6	159.5
50%-80%	14 $\leq$ RefMult $<$ 94	44.1	48.3

Table 3.1: Centrality definitions for different uncorrected reference multiplicity ranges. Uncorrected N_{charge} stands for the average value of uncorrected reference multiplicity in certain centrality bin. The fourth column represents the efficiency corrected value of N_{charge}.

3.3 Track Selection

In this analysis, we observe the hadronic decay channels of $K^{*0}(892) \rightarrow K^{+}\pi^{-}$, $\overline{K^{*0}}(892) \rightarrow K^{-}\pi^{+}$ and $K^{*\pm}(892) \rightarrow K^{0}_{S}\pi^{\pm}$. In the following text, the term K^{*0} stands for K^{*0} and $\overline{K^{*0}}$ while K^{*} stands for K^{*0}, $\overline{K^{*0}}$ and $K^{*\pm}$ unless specified. The lifetime of the K^{*} is 3.89 fm/c so that the K^{*} meson will decay extremely close to the primary collision vertex and the daughters would appear to originate from the interaction point. In the case of the K^{*0}, we select charged kaon and charged pion candidates from primary tracks whose measured distance of closest approach (DCA) to the primary interaction vertex were less than 3.0 cm in Au+Au collision events. In p+p collision events, we selected primary tracks with their DCA to the primary collision vertex less than 4.0 cm. In the case of $K^{*\pm}$, first, a charged K^* would undergo a strong decay to produce a K_S^0 and a charged pion which we name as a daughter pion of the charged K^*. Second, the newly produced K_S^0 would undergo a weak decay via $K_S^0 \to \pi^+\pi^-$ with $c\tau$=2.67 cm. We name these two oppositely charged pions from K_S^0 decay as grand-daughter pions of the charged K^*. We select the charged daughter pion candidates from primary tracks and select K_S^0 candidates through their decay vertex geometries since STAR has shown its great ability in measuring this V0 shaped decay mode through the decay topology method.

In Au+Au collisions, charged kaon candidates for the K^{*0} analysis were selected by requiring their dE/dx to be within two standard deviations (2σ) of the expected value ($|N_{\sigma\pi}| < 2$) while a looser dE/dx cut of 3σ was used for charged pion candidates ($|N_{\sigma K}| < 3$). A pseudo-rapidity cut $|\eta| < 0.8$ was applied to all the kaon and pion candidate tracks in order to reduce the event-to-event multiplicity variations in the high pseudo-rapidity range. Kaons and pions were also required to have at least 15 fit points to assure the track fitting quality. Also, in order to avoid selecting split tracks, the ratio of number of fit points over maximum possible points was required to be greater than 0.55 for all the candidate tracks. Only the tracks with both their momenta (p) and transverse momenta (p_T) larger than 0.2 GeV/c were selected in order to enhance track quality. Although using the STAR TPC detector, we can only identify kaons and pions with momenta up to 0.75 GeV/c, we select tracks with momenta up to 10 GeV/c in order to keep the largest possible statistics for the K^{*0} analysis in Au+Au collisions. Doing this may lead to mis-identified correlated pairs and contaminate the K^{*0} invariant mass spectra. We will discuss this issue in detail in section 3.5.

In p+p collisions, we have enough statistics to precisely measure the K^{*0} invariant mass spectra and the K^{*0} mass and width distributions as a function of transverse momentum so that we need to have minimal contamination from mis-identified correlated pairs. Thus a clean PID cut was applied to the kaon candidate tracks which required kaon momenta $p < 0.7$ GeV/c and kaon transverse momenta $p_T < 0.7$ GeV/c. The pion momenta and transverse momenta cuts were kept the same as in Au+Au collisions. A tighter dE/dx cut of 2σ was also used for both the pion and the kaon candidate tracks ($|N_{\sigma\pi,K}| < 2$). All the other track cuts for both kaon and pion candidates in the K^{*0} analysis in p+p collisions were the same as in Au+Au collisions. In the case of the charged K^*, due to the extremely short lifetime of the charged K^*, the daughter pion should seem to originate from the primary collision vertex so that all the cuts applied to the daughter pion candidates were the same as the pion track cuts in K^{*0} analysis in Au+Au collisions. The grand-daughter charged pion candidates were selected from global tracks with their DCA's to the primary vertex greater than 0.5 cm to reconstruct the K_S^0 signals. Candidate grand-daughter charged pions

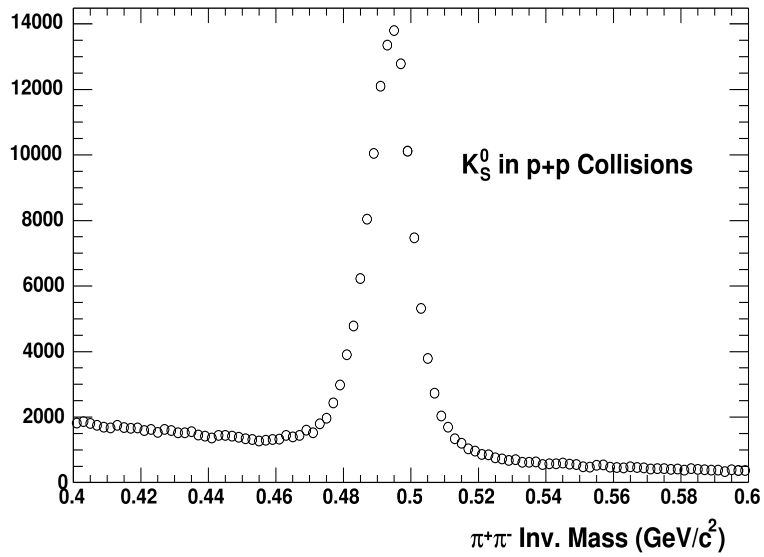

Figure 3.3: The $\pi^+\pi^-$ invariant mass distribution representing K_S^0 reconstructed from the decay topology method via $K_S^0 \rightarrow \pi^+\pi^-$ in p+p collisions.

were also required to have at least 15 hit points in the TPC and momenta greater than 0.2 GeV/c. Oppositely charged candidates, if their DCA to each other was less than 1.0 cm, were then paired to form neutral decay vertices which were required to be at least 2.0 cm in distance from the primary vertex. The reconstructed K_S^0 momentum vector was required to point back by a straight line to the primary vertex within 1.0 cm. Figure 3.3 shows the $\pi^+\pi^-$ invariant mass distribution representing the K_S^0 in p+p collisions. In order to reduce the combinatorial background, only the K_S^0 candidates with $\pi^+\pi^-$ invariant mass in the range between 0.48 and 0.51 GeV/c^2 were selected. When pairing the K_S^0 candidates with daughter pions to reconstruct the charged K^* signal, track ID's (unique numbers asigned to each track in the event reconstruction stage) were checked in order to avoid using the same track to be the daughter pion and grand-daughter pion.

In a summary, all the cuts used in K^* analysis are listed in Table 3.2

Cuts	K^{*0}		$K^{*\pm}$ in p+p	
	Au+Au	p+p	Daughter $\pi^\pm$	K_S^0
$N_{\sigma K}$	(-2.0, 2.0)	(-2.0, 2.0)		decayLength>2.0cm
$N_{\sigma\pi}$	(-3.0, 3.0)	(-2.0, 2.0)	(-2.0, 2.0)	dcaDaughters<1.0cm
Kaon p (GeV/c)	(0.2, 10.0)	(0.2, 0.7)		dcaV0PrmVx<1.0cm
Kaon p_T (GeV/c)	(0.2, 10.0)	(0.2, 0.7)		dcaPosPrmVx>0.5cm
Pion p (GeV/c)	(0.2, 10.0)	(0.2, 10.0)	(0.2, 10.0)	dcaNegPrmVx>0.5cm
Pion p_T (GeV/c)	(0.2, 10.0)	(0.2, 10.0)	(0.2, 10.0)	$M_{K_S^0}$: (0.48, 0.51)
NFitPnts	> 15	> 15	> 15	π^+: NTpcHits > 15
NFitPnts/MaxPnts	> 0.55	> 0.55	> 0.55	π^-: NTpcHits > 15
Pseudo-Rapidity η	$\|\eta\| < 0.8$	$\|\eta\| < 0.8$	$\|\eta\| < 0.8$	π^+: $p > 0.2$ GeV/c
DCA (cm)	< 3.0	< 4.0	< 4.0	π^-: $p > 0.2$ GeV/c
Pair Rapidity y	$\|y\|$ 0.5	$\|y\| < 0.5$	$\|y\| < 0.5$	

Table 3.2: List of charged kaon and charged pion track cuts and neutral kaon topological cuts used for K^* analysis in Au+Au and p+p collisions. The unit of $M_{K_S^0}$ is GeV/c^2.

3.4 Building the Signal

In relativistic heavy-ion collisions, the STAR TPC can record up to several thousand charged tracks per event originating from the primary collision vertex. It's impossible to build the K^{*0} signal by only selecting the kaon and pion daughters, because these tracks are indistinguishable from other primary tracks. Therefore, we use the following method to reconstruct the signal. By pairing each oppositely charged kaon and pion in an event, we can calculate the $K\pi$ pair invariant mass spectrum. Figure 3.4

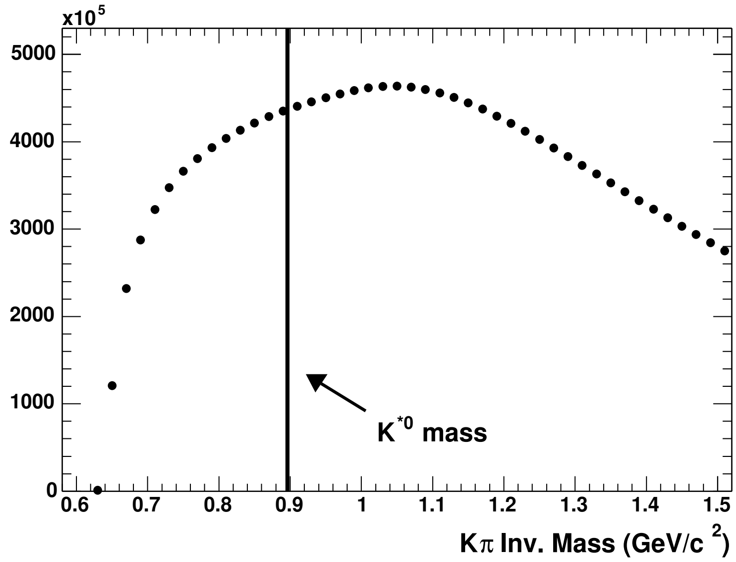

Figure 3.4: $K\pi$ invariant mass distribution from same-event pairs in minimum bias triggered Au+Au collisions. Symbols shown represent counts in 20MeV/c^2 bins.

shows the $K\pi$ invariant mass distribution from same-event pairs in minimum bias triggered Au+Au collisions. The invariant mass distribution derived in this manner is mostly from random combinatorial $K\pi$ pairs which have no correlation at all. The K^{*0} signal in this invariant mass spectrum is only a small fraction as big as $\sim$0.1% of the background in the K^{*0} mass range. We must subtract the huge amount of combinatorial background to make visible the real K^{*0} signal. There are two possible ways of calculating the background so that it may be subtracted: (1) the event-mixing technique: building a reference distribution calculated using uncorrelated oppositely charged kaons and pions from different events; (2) the like-sign technique: building a reference distribution calculated using kaons and pions with the same charge from the same event.

3.4.1 Event-Mixing Technique

The same-event $K\pi$ pair invariant mass spectrum contains a small subset of signal pairs for which the pair-partner momenta are in fact correlated (i.e. from the same parent K^*) and a large subset of signal pairs for which the pair-partner momenta

are not correlated. In order to subtract the subset of non-correlated pairs, a second mixed-event sample of pairs is formed, in which the first pair partner is taken from one event and the second pair partner is taken from another event. In doing this, the pair partners' momenta in the mixed-event sample are totally uncorrelated.
In order to keep as much as possible similar event structure between mixed events, we divided the whole data sample into 10 uniform multiplicity bins and 10 uniform vertex Z position bins. We then only select the second pair partner from events in the same multiplicity bin and the same vertex Z position bin as the event which the first pair partner was from.

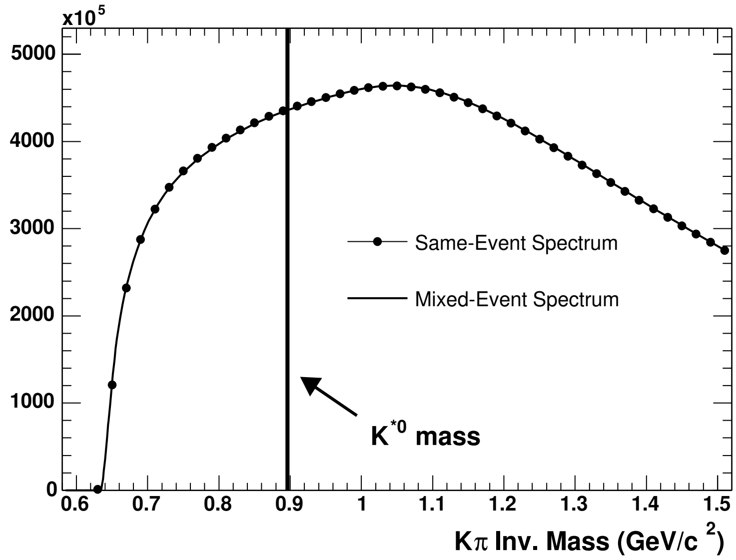

Figure 3.5: The same-event $K\pi$ pair invariant mass spectrum (solid symbols) and the mixed-event $K\pi$ pair invariant mass spectrum after normalization (solid curve).

In the same-event spectrum, we sampled $K_1^+\pi_1^-$ and $K_1^-\pi_1^+$ pairs. In the mixed-event spectrum, we sampled $K_1^+\pi_2^-$, $K_1^-\pi_2^+$, $K_2^+\pi_1^-$ and $K_2^-\pi_1^+$ pairs. The subscripts 1 and 2 stand for event number 1 and event number 2, respectively. We can choose the second pair partner from many other events to reduce the statistical errors in the mixed-event spectrum. We choose to mix with five other events so that the total number of entries in the mixed-event spectrum would be about ten times as much as the total number of entries in the same-event spectrum. Thus we need to normalize the mixed-event spectrum before the background subtraction for the same-event spectrum. In the same-event spectrum, the $K\pi$ pairs with their invariant mass greater than 1.1 GeV/c^2 are very unlikely to be correlated so that we calculate the normalization factor by taking the ratio of the number of entries in the same-event spectrum with invariant mass $>$ 1.1 GeV/c^2 to the number of entries in the mixed-event spectrum also with invariant mass $>$ 1.1 GeV/c^2. Figure 3.5 shows the same-event $K\pi$ pair invariant mass spectrum and the mixed-event $K\pi$ pair invariant mass spectrum after normalization. The mixed-event spectrum as the background is subtracted from the same-event spectrum as shown in Equation 3.1:

$$N_{K^{*0}}(m) = N_{K_1^+\pi_1^-}(m)+N_{K_1^-\pi_1^+}(m)-R\times\sum_{i=2}^{6}[N_{K_1^+\pi_i^-}(m)+N_{K_1^-\pi_i^+}(m)+N_{K_i^+\pi_1^-}(m)+N_{K_i^-\pi_1^+}(m)] \tag{3.1}$$

in which N stands for the count in a bin of $K\pi$ pair invariant mass with its bin center at m, and R represents the normalization factor. After the mixed-event background subtraction, the K^{*0} signal is visible as shown in the $K\pi$ pair invariant mass spectrum in Figure 3.6. Below the K^{*0} signal, there is a certain amount of residual background

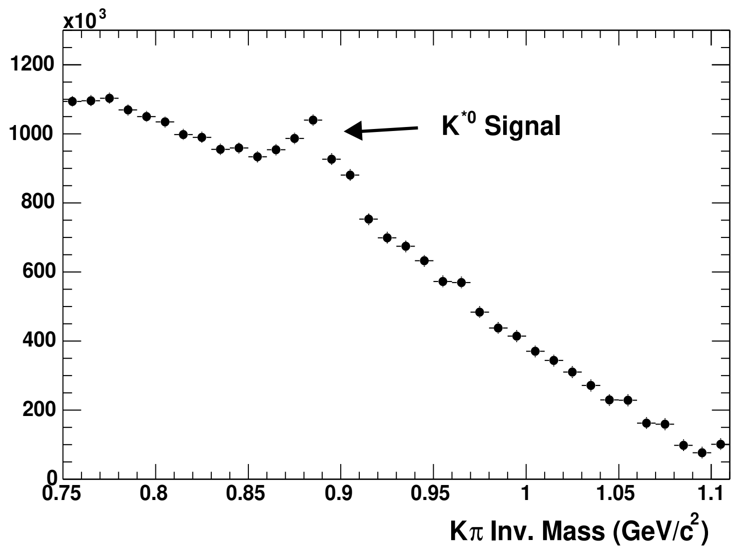

Figure 3.6: The $K\pi$ pair invariant mass spectrum after mixed-event background subtraction indicating K^{*0} signal.

which will be discussed in detail in section 3.5.
The event-mixing technique has been widely and successfully used in resonance production analysis besides K^*, such as ϕ [20], Δ^{++} [21], $\Lambda^*(1520)$ [23] and $\Sigma^*(1385)$ [22], in relativistic heavy ion collisions in RHIC. The event-mixing technique has also been tested in measuring the Λ production in Au+Au collisions at $\sqrt{s_{NN}}$=130 GeV with data taken during the first RHIC run in 2000. Results included in [54] are now discussed briefly here.
As a check on the event-mixing technique, we measured the Λ strange baryon through its weak decay channel $\Lambda \rightarrow p\pi^-$ and $\overline{\Lambda} \rightarrow \overline{p}\pi^+$. Considering its relatively large de-

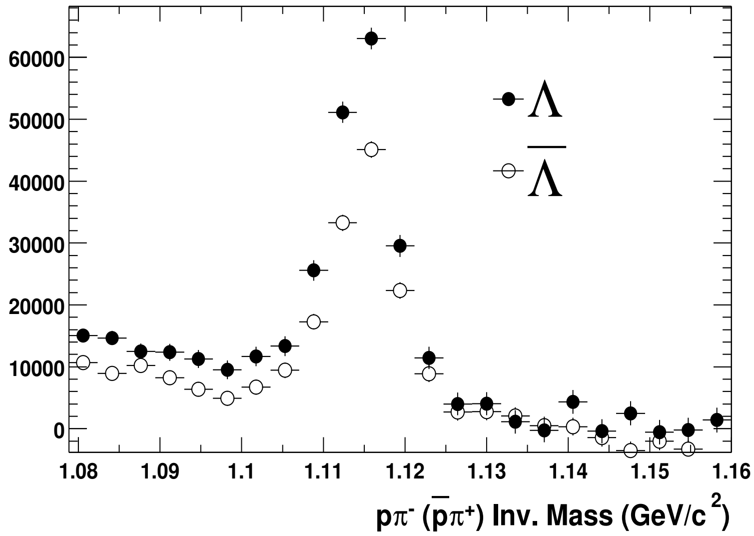

Figure 3.7: Invariant mass distribution of Λ (solid symbols) and $\overline{\Lambda}$ (open symbols) using the event-mixing technique from 197K minimum bias triggered Au+Au collisions events at $\sqrt{s_{NN}}$=130GeV.

cay length ($c\tau$=7.89 cm), we selected proton and anti-proton candidates and charged pion candidates from global tracks. The Λ and $\overline{\Lambda}$ signals are shown in the $p\pi^-$ and $\overline{p}\pi^+$ invariant mass spectrum after mixed-event background subtraction in Figure 3.7. Figure 3.8 shows the Λ and $\overline{\Lambda}$ rapidity density as a function of negative hadron multiplicity at mid-rapidity. The open symbols in Figure 3.8 are the results measured

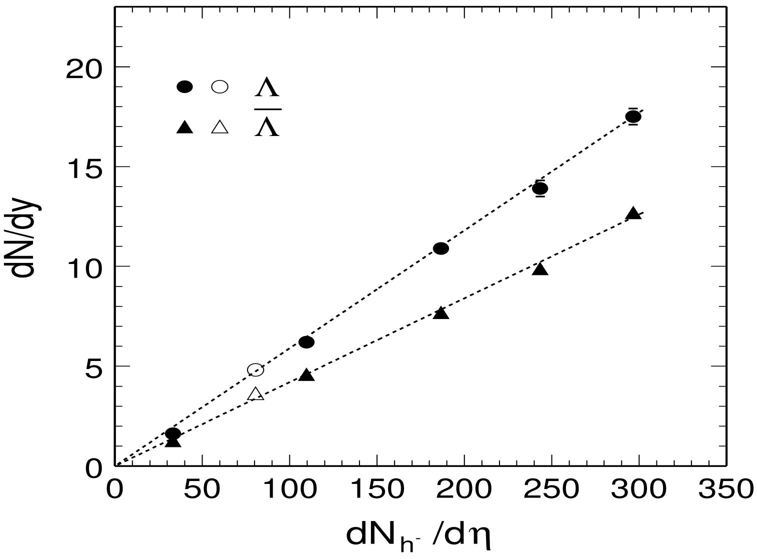

Figure 3.8: Λ and $\overline{\Lambda}$ rapidity density as a function of negative hadron multiplicity at mid-rapidity. Open symbols represent results from event-mixing technique and solid symbols stand for results from decay topology technique. Figure is taken from [54].

using the event-mixing technique while solid symbols are from the V0 decay topology measurement. We can see that the event-mixing results agreed well with the V0 measurements and the event-mixing technique was successful in measuring the Λ and $\overline{\Lambda}$ production.

3.4.2 Like-Sign Technique

Besides the event-mixing technique, another approach to subtract the subset of non-correlated pairs from the same-event $K\pi$ pair invariant mass spectrum is to use the like-sign technique. After the same-event sample of $K\pi$ pairs is formed in one event, a second like-sign set of pairs is formed, in which the pairs consist of pair partners which have the same charge sign and are taken from the same event.

In the same-event $K\pi$ pair invariant mass spectrum, we sampled $K_1^+\pi_1^-$ and $K_1^-\pi_1^+$ pairs and in the like-sign $K\pi$ pair invariant mass spectrum, we sampled $K_1^+\pi_1^+$ and $K_1^-\pi_1^-$ pairs. Since the number of positive tracks may not be the same as the number of negative tracks in relativistic heavy ion collision events, in order to correctly subtract the subset of non-correlated pairs in the same-event spectrum, the like-sign invariant mass spectrum was calculated as shown in Equation 3.2 after getting the $K_1^+\pi_1^+$ and $K_1^-\pi_1^-$ pair invariant mass spectra respectively:

$$N_{Like-Sign}(m) = 2 \times \sqrt{N_{K_1^+\pi_1^+}(m) \times N_{K_1^-\pi_1^-}(m)} \tag{3.2}$$

Figure 3.9 shows the same-event $K\pi$ pair invariant mass spectrum and the like-sign $K\pi$ pair invariant mass spectrum calculated using Equation 3.2. Thus the like-sign

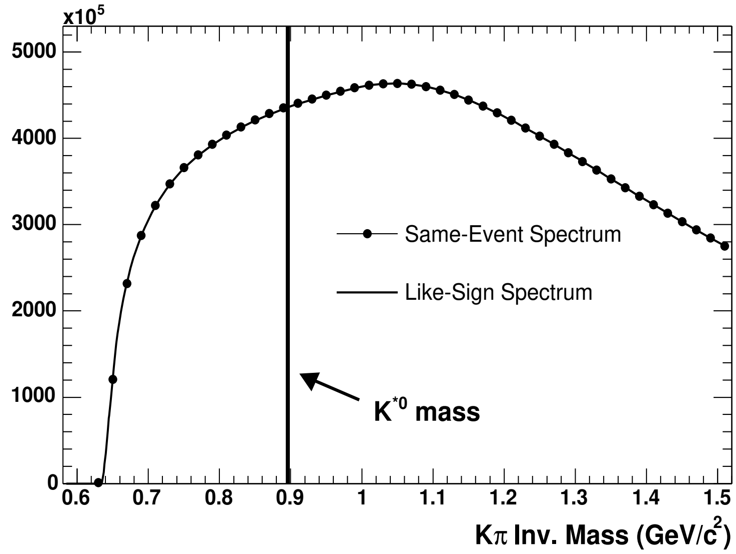

Figure 3.9: The same-event $K\pi$ pair invariant mass spectrum (solid symbols) and the like-sign $K\pi$ pair invariant mass spectrum (solid curve).

spectrum can be subtracted from the same-event spectrum in the way as shown in Equation 3.3:

$$N_{K^{*0}}(m) = N_{K_1^+\pi_1^-} + N_{K_1^-\pi_1^+} - 2 \times \sqrt{N_{K_1^+\pi_1^+}(m) \times N_{K_1^-\pi_1^-}(m)} \tag{3.3}$$

The like-sign background subtracted $K\pi$ pair invariant mass spectrum is shown in Figure 3.10 and a K^{*0} signal is thus visible.

Compared with the event-mixing technique, the like-sign technique has an advantage in that the same-event and like-sign pairs are taken from the same events so that there is no event structure difference between the like-sign spectrum and the same-event

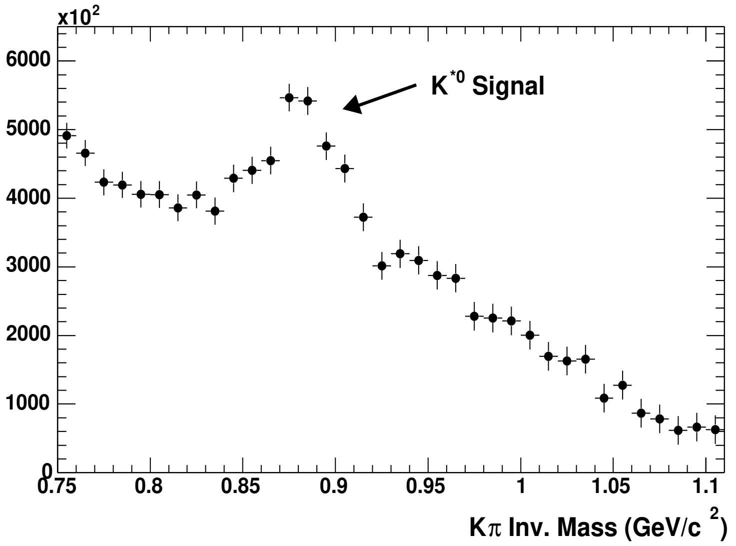

Figure 3.10: The $K\pi$ invariant mass spectrum after like-sign background subtraction indicating K^{*0} signal.

spectrum due to effects such as elliptic flow effect [56]. The like-sign technique has also been successfully applied in studying the $\rho^0(770)$ production [19] by measuring the decay channel $\rho^0 \to \pi^+\pi^-$ in Au+Au and p+p collisions at $\sqrt{s_{NN}}$=200 GeV in RHIC. In the $\pi^+\pi^-$ pair invariant mass spectrum, correlated $\pi^+\pi^-$ pairs may come from many possible particles such as ρ^0, K_S^0, ω, η, η' and f_0 so that the invariant mass spectrum might be complicated enough that we must avoid the event structure difference which might be brought by the event-mixing technique.
The short-coming of like-sign technique is that the counts in the like-sign background subtracted spectrum have larger statistical uncertainties than the counts in the mixed-event background subtracted spectrum, since by using event-mixing technique, we can sample the background oppositely charged $K\pi$ pairs by mixing one event with many other events.

In this K^{*0} analysis, reducing statistical errors is important so we use the event-mixing technique to reconstruct the K^{*0} signal while using the like-sign technique to study the sources of the residual background under the K^{*0} peak after mixed-event background subtraction which will be addressed in detail in Section 3.5.

3.5 Describing the Background

The event-mixing technique is in general effective in reconstructing resonance signals in heavy-ion collisions where the topological method used in K_S^0 and Λ reconstruction is not possible. Nevertheless, the mixed-event combinatorial background cannot perfectly reproduce the background in the same-event spectrum. Thus after mixed-event background subtraction, there is always a certain amount of residual background remaining under the resonance signal [55, 56]. In the case of the K^{*0} analysis, Figure 3.6 and the open star symbols in Figure 3.11 show the $K\pi$ pair invariant mass spectrum after mixed-event background subtraction, indicating the K^{*0} signal. Under the K^{*0} signal, there is a certain amount of residual background which has not been subtracted by the mixed-event spectrum. This residual background comes from three dominant sources: (1) elliptic flow effect in non-central Au+Au collisions; (2) correlated real $K\pi$ pair from particles' decay; (3) correlated but mis-identified pairs.

3.5.1 Elliptic Flow Effect

In non-central Au+Au collisions, the event in the plane perpendicular to the beam axis exhibits an elliptic shape. The long axis of the "ellipse" of the particle distribution in momentum space together with the beam axis defines the event's reaction plane. Each non-central Au+Au collision event has its unique reaction plane angle. Thus the azimuthal distributions for pion and kaon particles are different for different events. In event-mixing, the same-event $K\pi$ pair invariant mass spectrum obtained in one event will have different structure from the mixed-event invariant mass spectrum calculated from $K\pi$ pairs whose pair partners are from different events which have different reaction planes. This structure difference between the same-event and mixed-event spectra will lead to a residual background in the $K\pi$ invariant mass distribution after mixed-event background subtraction.

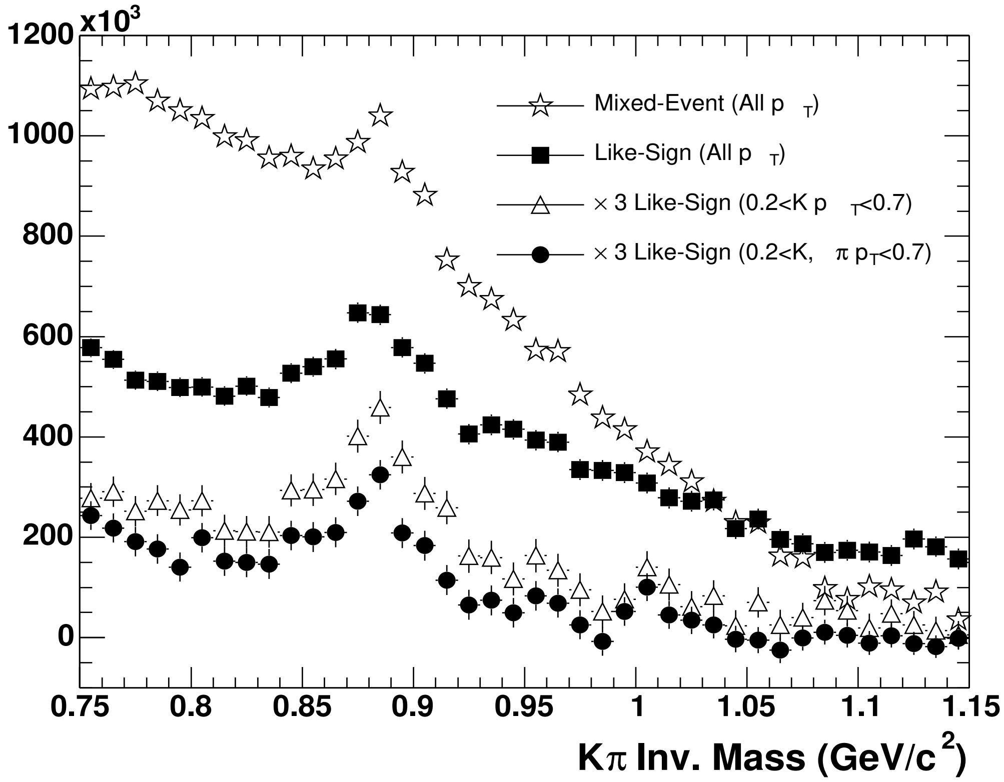

Figure 3.11: Different cuts from a like-sign study demonstrate the sources of background under the K^{*0} peak. The counts for the open squared symbols and the filled circle symbols have been scaled up by a factor of 3 in order to increase the visibility.

Using the like-sign technique, the same-event spectrum and the like-sign spectrum come from the same single event so that the elliptic flow effect can not cause this residual background. In Figure 3.11, the solid square symbols represent the $K\pi$ invariant mass distribution after like-sign background subtraction. The amplitude of the residual background after like-sign background subtraction is ~40% smaller than the amplitude of the residual background after the mixed-event background subtraction while the amplitude of the K^{*0} remains the same. The difference clearly shows the elliptic flow effect induced residual background.

3.5.2 Correlated Real $K\pi$ Pairs

Using the event-mixing technique, the subset of all correlated $K\pi$ pairs in the same-event spectrum cannot be subtracted by the mixed-event spectrum. In the same-event spectrum, besides the $K\pi$ pairs from K^{*0} decay, there are correlated $K\pi$ pairs from other particles with a decay mode into a $K\pi$ pair. None of these correlations are present in the mixed-event spectrum so that they are not subtracted away.

In the case of two-body decay modes, $K^*(1410)$, $K_0^*(1430)$, $K_2^*(1430)$, $K^*(1680)$, D^0 and many other particles can decay into an oppositely charged $K\pi$ pair. But the invariant mass reconstructed by using the exact daughter kaon and daughter pion from the decay of the above particles is larger than the K^{*0} mass so that the $K\pi$ pairs from the above particles' two-body decay don't contribute much to the residual background right under the K^* signal.

Some particles can decay into more than two final daughters and two of the final decay daughters can be counted as an oppositely charged $K\pi$ pairs, such as $K_1(1400)\rightarrow K\rho \rightarrow K\pi\pi$, $K^*(1410)\rightarrow K\rho \rightarrow K\pi\pi$, $K_2(1770)\rightarrow K\pi\pi$, etc. Thus the invariant mass calculated by these $K\pi$ pairs may have the same value as the K^{*0} mass so that these $K\pi$ pairs can contribute to the residual background.

3.5.3 Mis-Identified $K\pi$ Pairs

Through the energy loss (dE/dx) in the STAR TPC, kaon and pion particles can be identified only when their momenta are less than 0.7 GeV/c and protons can be identified only when their momenta are less than 1.1 GeV/c. In Au+Au collisions, we selected kaon and pion candidates with their momenta between 0.2 GeV/c and 10.0 GeV/c. Thus a pion (kaon) track with momentum greater than 0.7 GeV/c can be mis-identified as a kaon (pion) track. A proton track with momentum greater than 1.1 GeV/c can be mis-identified as either a kaon track or a pion track or both depending on whether we are selecting kaon or pion candidate tracks.

In the case of $\rho^0 \rightarrow \pi^+\pi^-$, if its positive (negative) pion daughter has a momentum greater than 0.7 GeV/c, it can be falsely reconstructed as a K^{*0} ($\overline{K^{*0}}$). If both daughters have momenta greater than 0.7 GeV/c, it can be mis-identified twice as both a K^{*0} and a $\overline{K^{*0}}$. The situation is the same for the following particles: $K_S^0 \rightarrow \pi^+\pi^-$, $\eta \rightarrow \pi^+\pi^-\pi^0$, $\omega \rightarrow \pi^+\pi^-(\pi^0)$, $f_0(980)\rightarrow \pi^+\pi^-$, etc. A similar situation can also exist for $\phi \rightarrow K^+K^-$ whose one or both kaon daughters can be mis-identified as pion(s). In the case of $\Lambda \rightarrow p\pi^-$ ($\overline{\Lambda} \rightarrow \overline{p}\pi^+$), if the proton (anti-proton) momentum is greater than 1.1 GeV/c, it can be mis-identified as a K^{*0} ($\overline{K^{*0}}$). In the case of $\Lambda^*(1520)\rightarrow pK^-$ ($\overline{\Lambda^*}(1520)\rightarrow \overline{p}K^+$), if the proton (anti-proton) momentum is greater than 1.1 GeV/c and the negative (positive) kaon momentum is less than 0.7 GeV/c, it can be mis-identified as a $\overline{K^{*0}}$ (K^{*0}). But when the proton (anti-proton) momentum is greater than 1.1 GeV/c and the negative (positive) kaon momentum is greater than 0.7 GeV/c, it can be mis-identified twice.

All the above particles can be falsely reconstructed as a K^{*0} or a $\overline{K^{*0}}$ or both if their daughter particles' momenta sit in a certain range. The invariant mass calculated from their mis-identified decay daughters will be different from their own mass and might be similar to the K^{*0} mass.

In Figure 3.11, the solid square symbols are for the $K\pi$ pair invariant mass spectrum after like-sign background subtraction with both the kaon and pion momenta in the range between 0.2 GeV/c and 10.0 GeV/c. Both the correlated real $K\pi$ pairs and mis-identified $K\pi$ pairs (with one or two daughters mis-identified) can contribute to the residual background. The open triangle symbols are for the spectrum after like-sign background subtraction with kaon momentum between 0.2 GeV/c and 0.7

GeV/c and pion momentum between 0.2 GeV/c and 10.0 GeV/c. Besides the correlated real $K\pi$ pairs' contribution, only the particles with one daughter mis-identified can contribute to the residual background. Compared to the solid square symbols, the residual background is reduced by ~90% and the K^{*0} is ~50% smaller in the open triangle symbols. The solid circle symbols represent the spectrum after like-sign background subtraction with both kaon and pion momentum between 0.2 GeV/c and 0.7 GeV/c so that no particle can be mis-identified as a K^{*0} or $\overline{K^{*0}}$ and only the correlated real $K\pi$ pairs can contribute to the residual background. Compared to the open triangle symbols, both the residual background and the signal are ~20% smaller than the open triangle symbols.

3.6 Extracting Mass and Width

The $K^*(892)$, a resonance vector meson, has J=1. The $K\pi$ invariant mass distribution for K^* should therefore be fit to a p-wave Breit-Wigner function [83]

$$F(M) = \frac{aM\Gamma M_0}{(M^2 - M_0^2)^2 + M_0^2\Gamma^2} \tag{3.4}$$

in which a is a constant parameter proportional to the yield of K^*, M is the $K\pi$ invariant mass, M_0 is the natural K^* mass, and

$$\Gamma(M) = [\frac{M^2 - (M_\pi + M_K)^2}{M_0^2 - (M_\pi + M_K)^2}]^{3/2}\frac{\Gamma_0 M_0}{M} \tag{3.5}$$

In Equation 3.5, Γ_0 is the K^* full width, M_π is the pion natural mass and M_K is the kaon natural mass.

In Au+Au collisions, besides direct production from partons [33], a K^* can also be generated through kaon and pion scattering in the hadron medium via $K + \pi \rightarrow K^* \rightarrow K + \pi$ [28]. The $K\pi$ invariant mass distribution for the K^* generated in this way might be modified by the initial kaon and pion phase space distribution. Thus the p-wave Breit-Wigner function should be multiplied by a phase space factor [81] (Equation 3.6) to fit the $K\pi$ invariant mass distribution. In p+p collisions, although the hadron medium might be much smaller than the medium in Au+Au collisions, a

K^* can also be re-produced through the same process [61].

$$P(M) = \frac{M}{\sqrt{M^2 + p_T^2}} e^{-\frac{\sqrt{M^2+p_T^2}}{T}} \tag{3.6}$$

Here p_T is the transverse momentum of the K^* and T is the temperature of the hadron medium. In this analysis, we use T=160 MeV in p+p collisions according to a statistical model calculation [82] which reasonably reproduces particle compositions. We use T=120 MeV in Au+Au collisions, since the observed K^* is presumably emitted close to the kinetic freeze-out stage and the hadron medium has already cooled down compared to the chemical freeze-out stage [81].

In the mixed-event background subtracted $K\pi$ invariant mass spectrum, there is a certain amount of residual background which can be reasonably represented by a linear function

$$B(M) = bM + c \tag{3.7}$$

in which b and c are two constant parameters.

In the end, we use Equation 3.8 to fit the $K\pi$ invariant mass spectrum

$$f(M) = F(M) \times P(M) + B(M) \tag{3.8}$$

in which a, b, c, M_0 and Γ_0 are five open parameters of the fit function. We can then extract the mass and full width of the K^* from the fit.

Figure 3.12 shows the $K\pi$ invariant mass spectrum in the mid-rapidity region $|y| < 0.5$ and with transverse momentum $p_T < 8.0$ GeV/c in top 10% central Au+Au collisions. Through the fit using Equation 3.8, we get the K^{*0} mass $M_0 = 893.7 \pm 1.1$ MeV/c^2 and full width $\Gamma_0 = 56.0 \pm 4.3$ MeV/c^2. Figure 3.13 shows the $K\pi$ invariant mass spectrum in the mid-rapidity region $|y| < 0.5$ and with transverse momentum $p_T < 1.6$ GeV/c in minimum bias triggered p+p collisions. Through the fit using Equation 3.8, we get the K^{*0} mass $M_0 = 887.2 \pm 0.5$ MeV/c^2 and full width $\Gamma_0 = 51.7 \pm 2.0$ MeV/c^2.

In order to get the K^{*0} mass and width distributions as a function of K^{*0} transverse momentum, we distribute both the $K\pi$ same-event invariant mass spectra and mixed-event invariant mass spectra into different transverse momentum bins. Then after

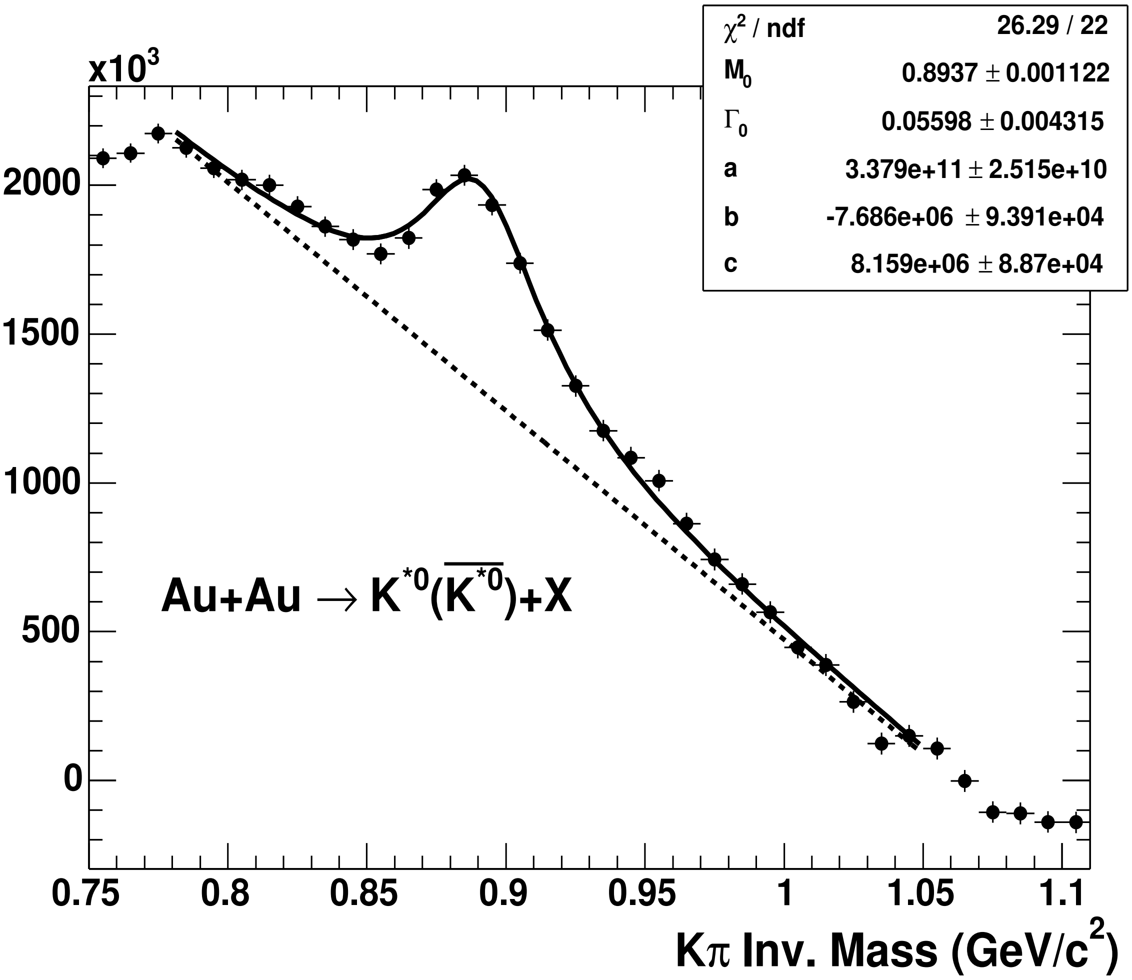

Figure 3.12: The $K\pi$ invariant mass distribution fit to Equation 3.9 to extract the K^{*0} mass and full width in top 10% central Au+Au collisions. The solid curve represents the fit function in Equation 3.8 and the dashed line represents the linear function in Equation 3.7. The units for the fit parameters M_0 and Γ_0 are GeV/c^2.

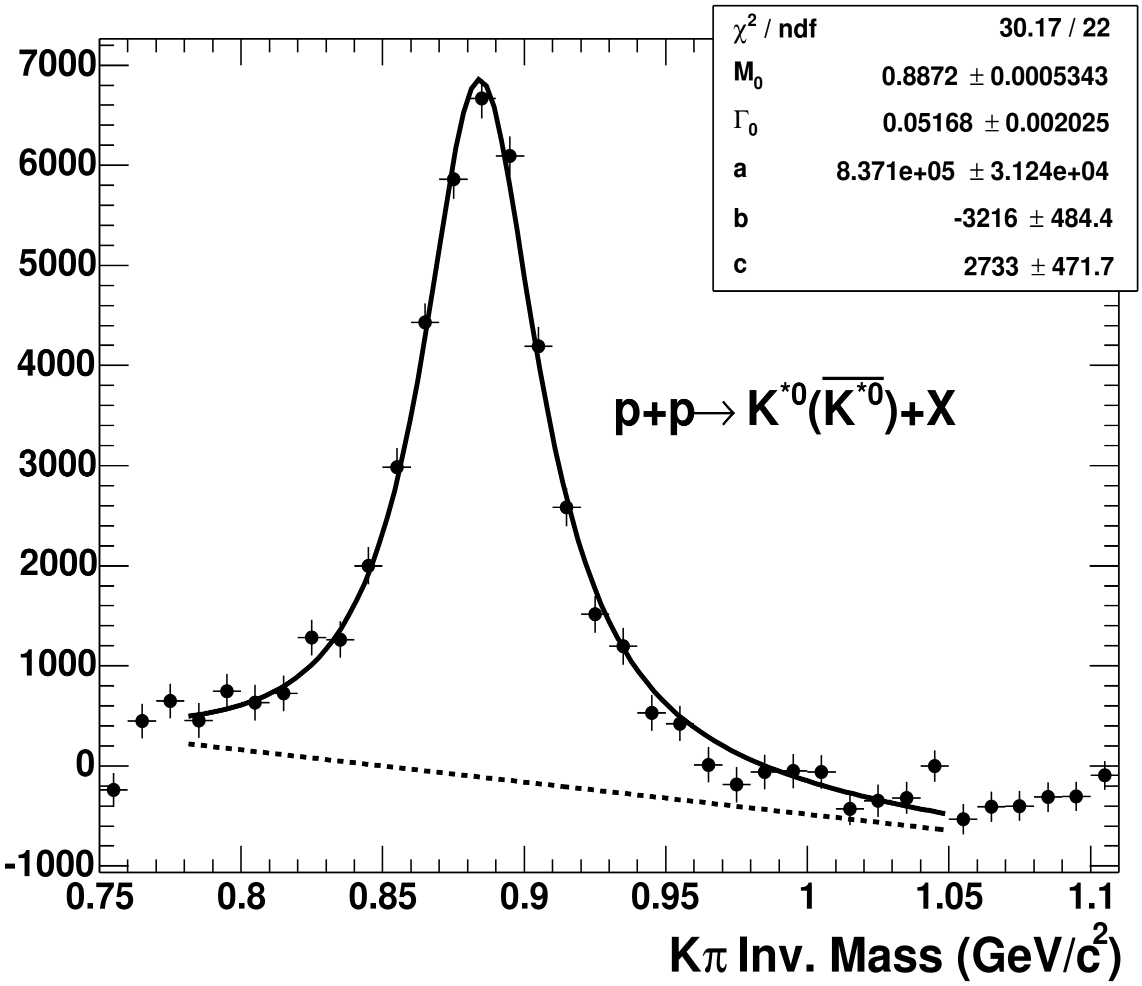

Figure 3.13: The $K\pi$ invariant mass distribution fit to Equation 3.8 to extract the K^{*0} mass and full width in p+p collisions. The solid curve represents the fit function in Equation 3.8 and the dashed line represents the linear function in Equation 3.7. The units for the fit parameters M_0 and Γ_0 are GeV/c^2.

mixed-event background subtraction in each transverse momentum bin, we fit the $K\pi$ invariant mass spectra using Equation 3.8 to get K^{*0} mass M_0 and full width Γ_0 in each transverse momentum bin. The results will be shown in Section 4.1

3.7 Extracting Yield

To extract the yield of K^* signal in certain transverse momentum range, the fit function in Equation 3.8 is simplified to [84]

$$f(M) = \frac{a}{2\pi \times 100} \frac{\Gamma_0}{(M - M_0)^2 + \Gamma_0^2/4} + bM + c \tag{3.9}$$

to reduce the statistical uncertainty for the yield after fit. In the above shown simplified Breit-Wigner function, a is the area of the Breit-Wigner distribution corresponding to the yield of the K^* signal. For the same reason, to reduce the statistical uncertainties of the fit, we fix the K^* mass, M_0, and full width, Γ_0, as the values which we have obtained from Section 3.6. The systematic difference for K^* yield between the methods using the simplified Breit-Wigner function and fixed mass and width parameters and the method using the fit function of Equation 3.8 will be discussed in Chapter 4.

Figure 3.14 shows the same $K\pi$ invariant mass spectrum as Figure 3.12 but the spectrum is fit to Equation 3.9 to extract the yield. Through the fit, we get the K^{*0} raw yield to be $5.66\times10^6 \pm 1.98\times10^5$. Figure 3.15 shows the same $K\pi$ invariant mass spectrum as Figure 3.13. Through the fit using Equation 3.9, we get the K^{*0} raw yield to be $5.64\times10^4 \pm 1087$. Figure 3.16 shows the $K_S^0\pi^{\pm}$ invariant mass spectrum in the mid-rapidity region $|y| < 0.5$ and with transverse momentum $p_T < 4.0$ GeV/c in minimum bias triggered p+p collisions. Through the fit using Equation 3.9, we get the $K^{*\pm}$ raw yield to be 9480 ± 497. The results of the K^{*0} and $K^{*\pm}$ raw yields from different transverse momentum bins in different Au+Au collision centralities and p+p collisions will be shown in Section 4.2 and 4.3.

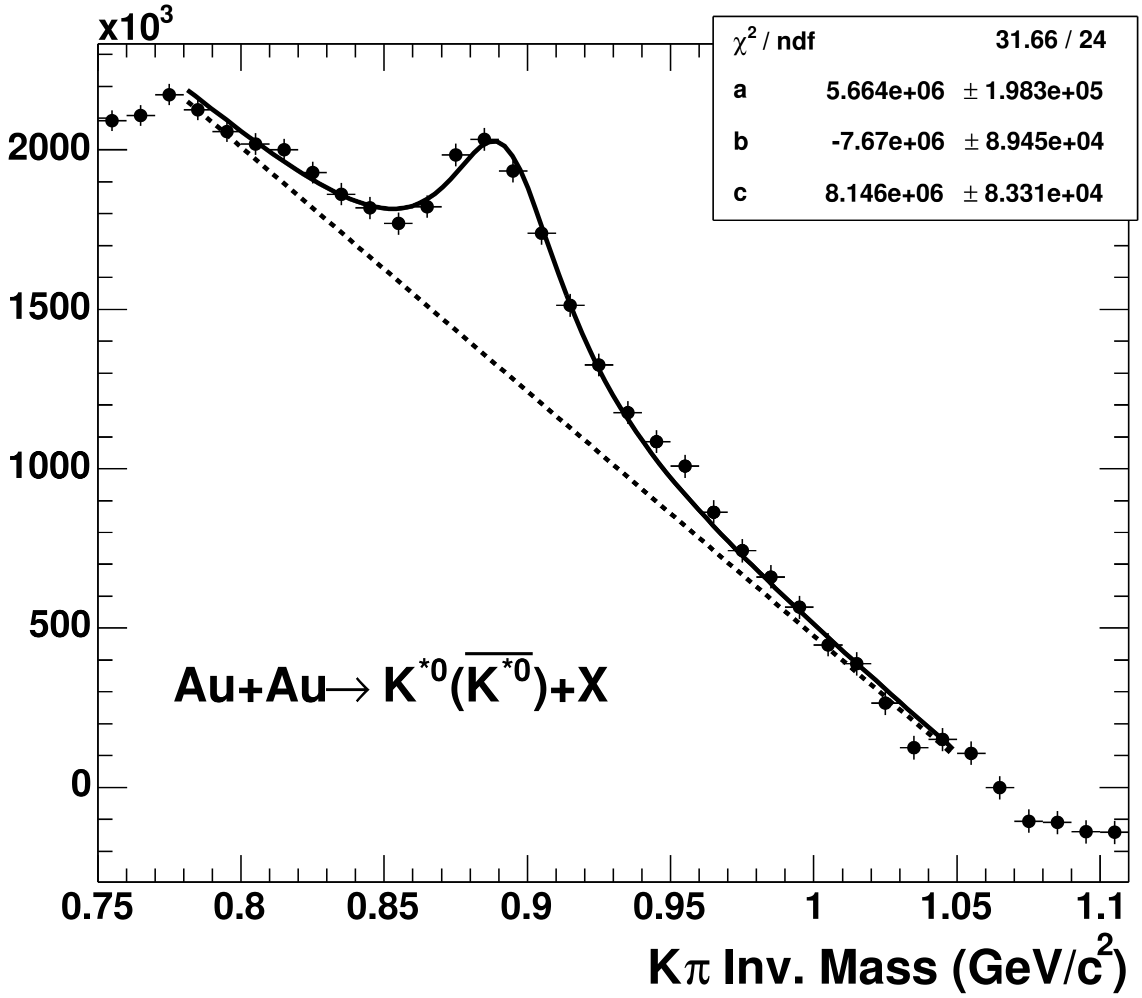

Figure 3.14: The $K\pi$ invariant mass distribution fit to Equation 3.9 to extract the K^{*0} yield in top 10% central Au+Au collisions. The solid curve represents the fit function in Equation 3.9 and the dashed line represents the linear function in Equation 3.7.

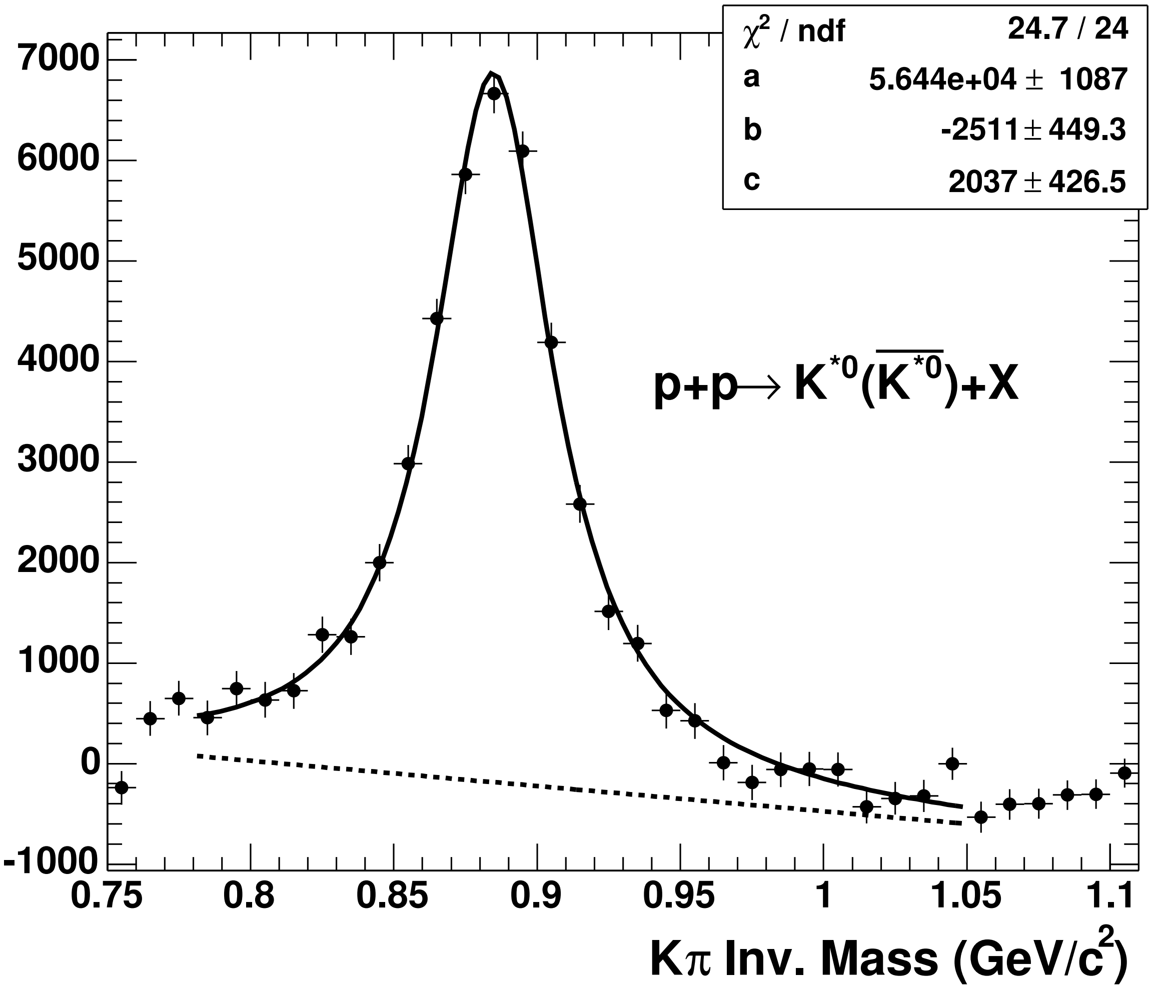

Figure 3.15: The $K\pi$ invariant mass distribution fit to Equation 3.9 to extract the K^{*0} yield in p+p collisions. The solid curve represents the fit function in Equation 3.9 and the dashed line represents the linear function in Equation 3.7.

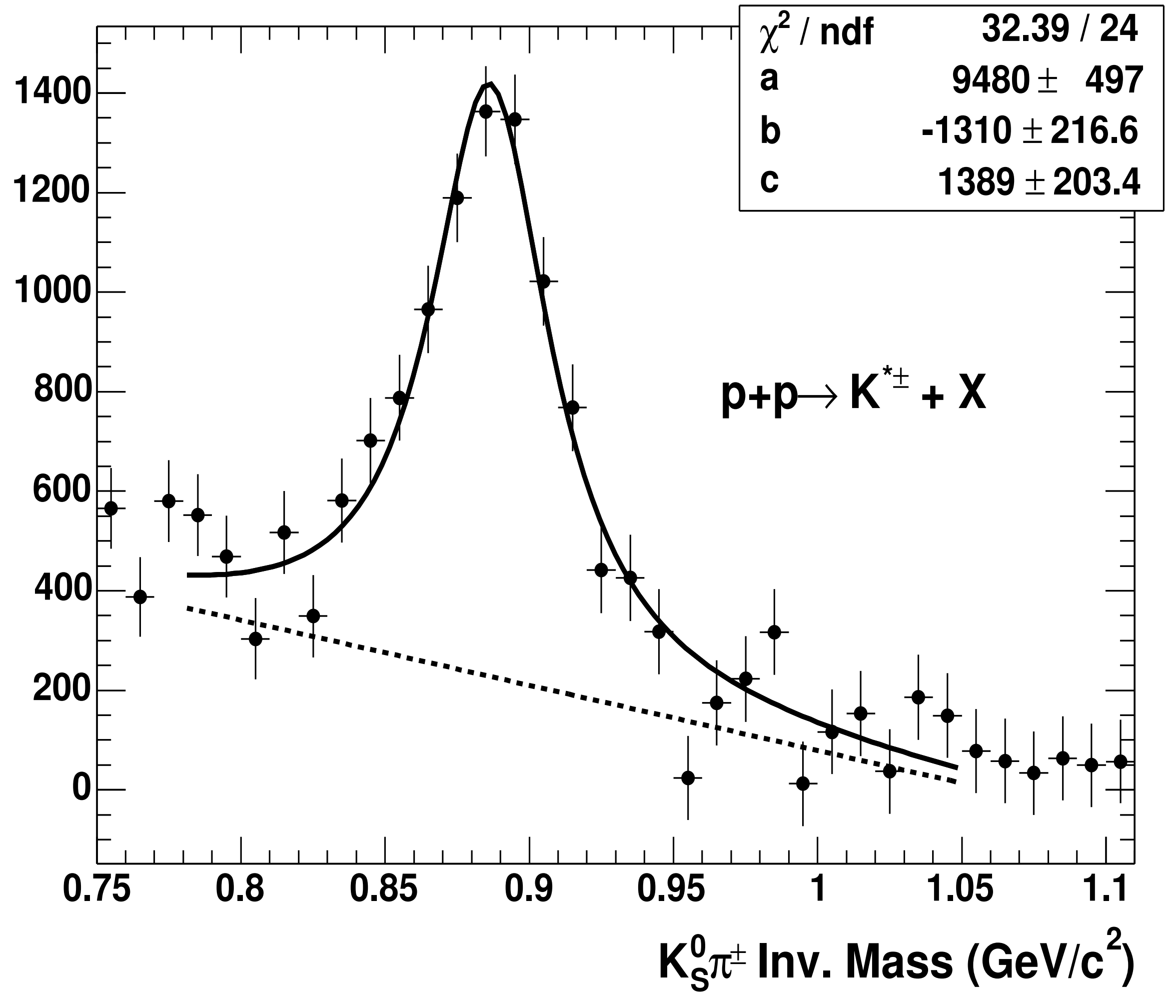

Figure 3.16: The $K_S^0\pi^{\pm}$ invariant mass distribution fit to Equation 3.9 to extract the $K^{*\pm}$ yield in p+p collisions. The solid curve represents the fit function in Equation 3.9 and the dashed line represents the linear function in Equation 3.7.

3.8 Efficiency Correction

Once the K^{*0} and $K^{*\pm}$ raw yields have been obtained from different transverse momentum bins in Au+Au and p+p collisions, the raw yields must be corrected for the total reconstruction efficiencies including detector acceptance, response, tracking efficiency, and dynamical cut effects.

The simulated K^{*0} and $K^{*\pm}$ mesons are generated using a flat p_T and a flat y distribution and pass through GSTAR [57] (the framework software package to run the STAR detector simulation using GEANT [58, 59]) and TRS (the TPC Response Simulator [57]). The K^* mesons are then decayed by GEANT via the decay channel $K^{*0} \to K\pi$ and $K^{*\pm} \to K_S^0\pi^\pm$. The simulated K^* mesons and their decay daughters are then combined with a real raw event and we call this combined event a simulated event. This simulated event is then passed through the standard STAR reconstruction chain and we call this event after reconstruction a reconstructed event. The reconstructed information of the decay daughters of K^* mesons in the reconstructed event is then associated with the Monte-Carlo information in the simulated event. Two more steps are needed to calculate the total reconstruction efficiencies of K^* raw yields: first, we get the total number of simulated K^{*0} and $K^{*\pm}$ mesons from simulated events in certain momentum bin; second, we find the associated decay daughter information in the reconstructed events and apply the same dynamical cuts which have been used in the real data analysis, and count the number of K^{*0} and $K^{*\pm}$ which pass these cuts and end up being reconstructed in this momentum bin. In the end, take ratio of the number obtained in the second step to the number obtained in the first step and this ratio is the total reconstructed efficiency for a certain transverse momentum bin in the mid-rapidity range. Efficiencies for different Au+Au collision centralities can also be calculated by selecting simulated and reconstructed events in these centralities.

The total reconstruction efficiencies for K^{*0} in different Au+Au collision centralities and p+p collisions, and for $K^{*\pm}$ in p+p collisions, are shown in Figure 3.17.

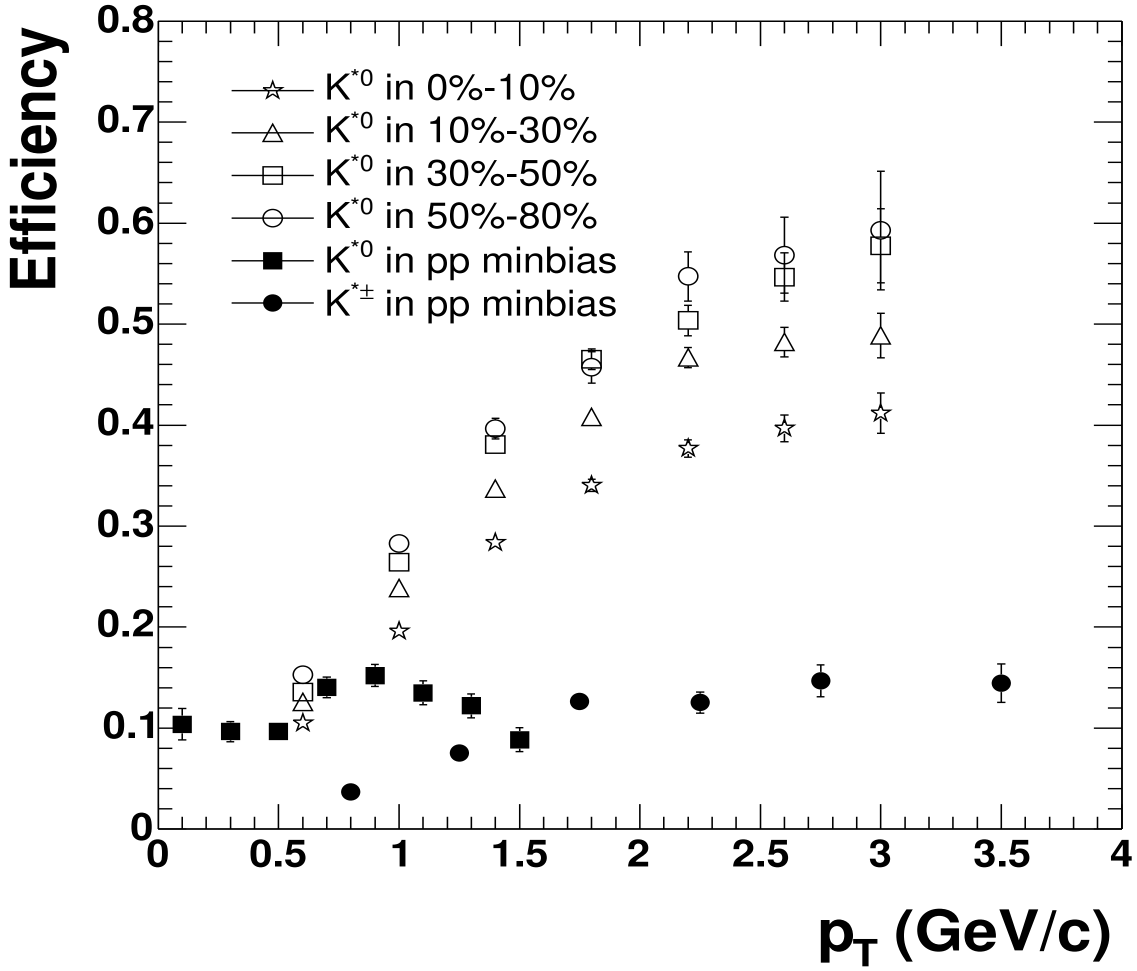

Figure 3.17: The total reconstruction efficiencies as a function of transverse momentum for K^{*0} in 0%-10%, 10%-30%, 30%-50% and 50%-80% Au+Au centralities and p+p collisions and $K^{*\pm}$ in p+p collisions.

3.9 Elliptic Flow Analysis

Elliptic flow v_2 and the reaction plane in Au+Au collisions have been defined in Section 1.1.6. In order to calculate the K^* elliptic flow v_2, we need to first estimate the reaction plane for each Au+Au collision event. The estimated reaction plane we call the event plane. Then we have two methods to calculate the K^* v_2: (1) According to Equation 1.7, we distribute the K^* yield as a function of $\phi - \Psi_r$ and fit with a simplified function of Equation 3.10 since v_1, v_3, v_4 and all higher components are close to zero and can be ignored.

$$N(\phi - \Psi_r) = N_0(1 + 2v_2 \cos[2(\phi - \Psi_r)]) \tag{3.10}$$

in which ϕ is the azimuthal angle of K^* in the momentum space; (2) According the definition of the second harmonic coefficient v_2 in Equation 1.7, we can get

$$v_2 =< \cos[2(\phi - \Psi_r)] > \tag{3.11}$$

in which <> indicates an average over all K^* in all events.
Method (1) gives us larger statistical uncertainties through the fit function, so we use method (2) to calculate the K^* elliptic flow in this analysis.

3.9.1 Estimation of Reaction Plane

The event plane can be independently determined for each harmonic of the anisotropic flow. For the second harmonic, the event plane angle Ψ_2 is defined by the equation

$$\Psi_2 = \frac{1}{2} \tan^{-1} \frac{\sum_i \omega_i \sin(2\phi_i)}{\sum_i \omega_i \cos(2\phi_i)} \tag{3.12}$$

The sums go over all the primary tracks used in the event plane determination, ϕ_i is the azimuthal angle in momentum space for the i-th primary track and the ω_i are the track weights [10, 52, 60]. Since the reaction plane is estimated by using a limited number of tracks, we will need to consider the limited resolution for determining the event plane. The track weights ω_i are used here to optimize the reaction plane resolution. In general the track weight ω is a combination of track azimuthal angle

(ϕ) weight ω_ϕ and transverse momentum (p_T) weight ω_{p_T}

$$\omega = \omega_\phi \times \omega_{p_T} \tag{3.13}$$

Considering the configuration of the TPC detector, because there are boundaries between sectors and different sectors are not identical in the azimuthal direction, the track reconstruction efficiency is not uniform as a function of azimuthal angle ϕ so that we need to correct each track used for reaction plane estimation by a track ϕ weight [52, 60]. In order to calculate ω_ϕ, tracks from all events are distributed in a function of ϕ, then we calculate

$$\omega_\phi = \frac{< N(\phi) >}{N(\phi)} \tag{3.14}$$

$N(\phi)$ is the count in an azimuthal angle bin with its bin center at ϕ and $< N(\phi) >$ is the average of $N(\phi)$ over all bins of ϕ.
The flow anisotropy increases with p_T and saturates when $p_T > 2$ GeV/c [12]. Thus

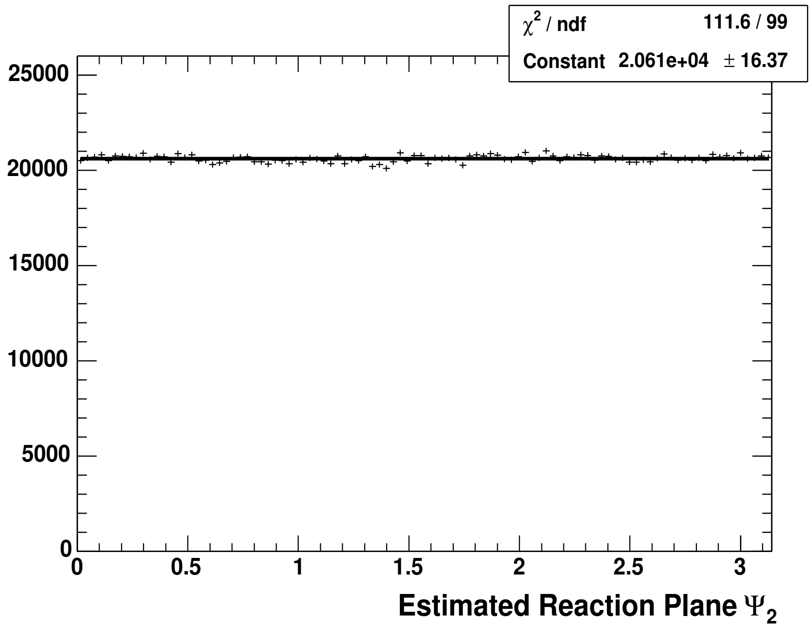

Figure 3.18: The estimated reaction plane distribution fit with a constant function in minimum bias triggered Au+Au collisions.

to optimize our determination of the reaction plane, tracks with different p_T need to be corrected for different p_T weights when estimating the reaction plane [52, 60]

$$\omega_{p_T} = \begin{cases} p_T/2 & \text{if } p_T < 2 \text{ GeV/c}, \\ 1 & \text{if } p_T \geq 2 \text{ GeV/c}. \end{cases} \tag{3.15}$$

Figure 3.18 shows the estimated reaction plane distribution in minimum bias triggered Au+Au collisions. The distribution is fit to a constant function, which fits quite well as we expect that it should.

3.9.2 Avoiding Auto Correlations

In general, if one track has already been used in the estimation of reaction plane, it should not be used again as a candidate kaon or pion track in calculating the $K\pi$ pair azimuthal angle with respect to the event plane angle. Otherwise, there is auto correlation between the pair azimuthal angle and the event plane angle [10, 52]. We must avoid this auto correlation in order to correctly measure the K^* elliptic flow. Using the event-mixing technique, we select a large amount of the primary tracks as kaon or pion candidates in reconstructing the K^* signal so that we cannot only use the remaining small number of primary tracks to estimate the reaction plane angle, otherwise we will have unacceptable resolution for the reaction plane. Therefore we use the following method to avoid the auto correlation.

For each $K\pi$ pair, we calculate the event plane angle by using all the other primary tracks except these kaon and pion candidate tracks. Equation 3.12 becomes

$$\Psi_2' = \frac{1}{2} \tan^{-1} \frac{\sum_i \omega_i \sin(2\phi_i) - \omega_K \sin(2\phi_K) - \omega_\pi \sin(2\phi_\pi)}{\sum_i \omega_i \cos(2\phi_i) - \omega_K \cos(2\phi_K) - \omega_\pi \cos(2\phi_\pi)} \tag{3.16}$$

The subscripts K and π stand for the kaon candidate track and pion candidate track, respectively. With this method, we avoided the auto correlation between the $K\pi$ azimuthal angle $\phi_{K\pi}$ and the event plane angle Ψ_2'.

3.9.3 K^* Elliptic Flow

Using the event-mixing technique, the K^{*0} signal is reconstructed in each $\cos[2(\phi_{K\pi} - \Psi_2')]$ bin. Figure 3.19 shows the K^{*0} yield as a function of $\cos[2(\phi_{K\pi} - \Psi_2')]$ in minimum bias triggered Au+Au collisions. After calculating the average of $< \cos[2(\phi_{K\pi} - \Psi_2')] >$, we get the K^{*0} elliptic flow, $v_2 = 0.074 \pm 0.040$.

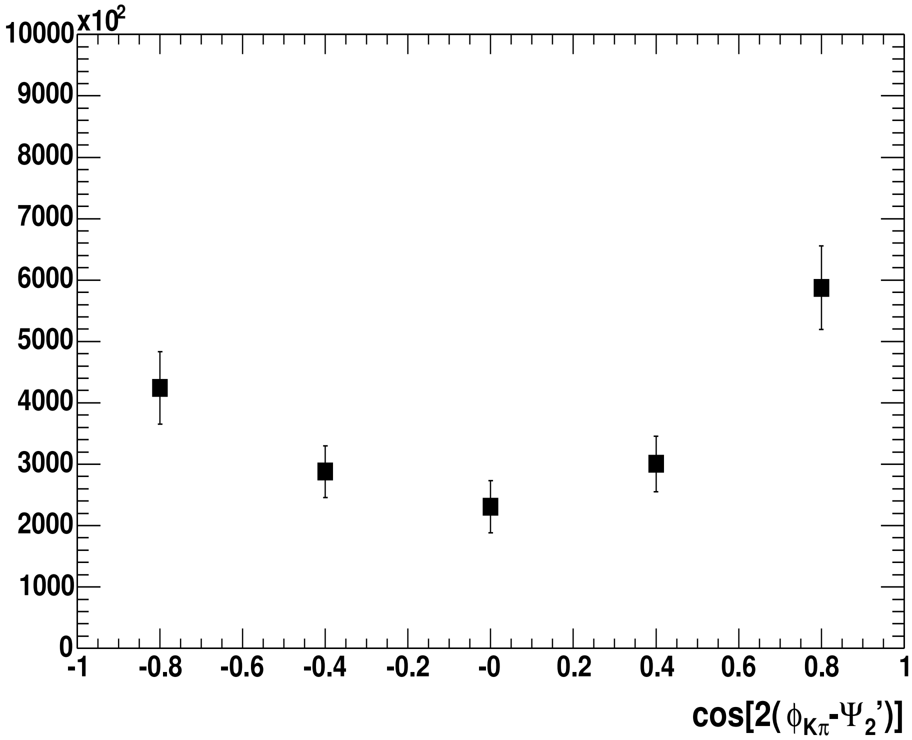

Figure 3.19: K^{*0} yield as a function of $\cos[2(\phi_{K\pi} - \Psi_2')]$ in minimum bias triggered Au+Au collisions.

3.9.4 Reaction Plane Resolution Correction

Since we use a limited number of tracks in each event to estimate the reaction plane, we will have a non-zero resolution for the reaction plane angle. This non-zero resolution makes the observed K^* elliptic flow v_2 always smaller than the true v_2. To get rid of this effect, we need to divide the observed v_2 by the reaction plane resolution

$$v_2 = v_2^{obs} / < \cos[2(\Psi_2 - \Psi_r)] > \tag{3.17}$$

We use Equation 3.18 to calculate the reaction plane resolution [10]

$$< \cos[2k(\Psi_2 - \Psi_r)] >= \frac{\sqrt{\pi}}{2\sqrt{2}} \chi_2 e^{-\chi_2^2/4} [I_{(k-1)/2}(\chi_2^2/4) + I_{(k+1)/2}(\chi_2^2/4)] \tag{3.18}$$

In the above equation, k=1, $\chi_2 = v_2\sqrt{2N}$ (N is the number of tracks used to estimate the reaction plane) and I_ν is the modified Bessel function of order ν.
There is another more simple way to calculate the reaction plane resolution with some approximations. First we randomly divide one event into two sub-events a and b and calculate the event planes Ψ_2^a and Ψ_2^b from these two sub-events [10]. Then

$$< \cos[2(\Psi_2^a - \Psi_2^b)] >=< \cos[2(\Psi_2^a - \Psi_r)] > \times < \cos[2(\Psi_2^b - \Psi_r)] > \tag{3.19}$$

If the two sub-events have equal multiplicity, we have

$$< \cos[2(\Psi_2^a - \Psi_r)] >= \sqrt{< \cos[2(\Psi_2^a - \Psi_2^b)] >} \tag{3.20}$$

We then assume the number (N) of tracks used in the full event reaction plane estimation is twice as large as the number of tracks in each sub-event and the resolution is proportional to $\sqrt{N}$, then the resolution is

$$< \cos[2(\Psi_2 - \Psi_r)] >= \sqrt{2} < \cos[2(\Psi_2^a - \Psi_r)] > \tag{3.21}$$

The reaction plane resolution calculated using Equation 3.18 for minimum bias triggered Au+Au collisions is 0.76 $\pm$ 0.01. Then we use this resolution to correct the K^{*0} observed v_2 in Section 3.9.4 and get $v_2 = 0.097 \pm 0.053$. Results for the K^{*0} v_2 as a function of p_T and as a function of collision centrality will be shown in Section 4.7.

Chapter 4

Results

4.1 Mass and Width Distribution

In strongly interacting matter at high temperature and high densities, dynamical interactions of the K^* resonance with the surrounding matter may cause the modification of the K^* mass, width and even the mass line shape due to the so-called in-medium effect. In the hadron gas, kaon and pion particles can re-generate K^* signals through $K\pi \to K^* \to K\pi$ so that the K^* resonance mass line shape might be affected by the kaon and pion initial phase space distributions. This re-generation channel can also interfere with the kaon and pion elastic scattering channel through $K\pi \to K\pi$. This interference may also modify the K^* properties [61]. Even though the size of the system formed in p+p collisions is smaller than in Au+Au collisions, interactions that may modify the K^* resonance are also expected [61]. Thus a measurement of the $K^*(892)$ mass, width and line shape in Au+Au an p+p collisions can provide very interesting information on possible in-medium effects.
The $K^{*0}(892)$ mass and width in each p_T bin at mid-rapidity ($|y| < 0.5$) are measured using the method described in Section 3.6 in minimum bias triggered p+p collisions and top 10% central triggered Au+Au collisions at $\sqrt{s_{NN}}$=200 GeV. As shown in Equation 3.9, the mixed-event background subtracted $K\pi$ invariant mass distribution in each p_T bin is fit to a p-wave Breit-Wigner function multiplied by a phase space factor plus a linear function representing the residual background.

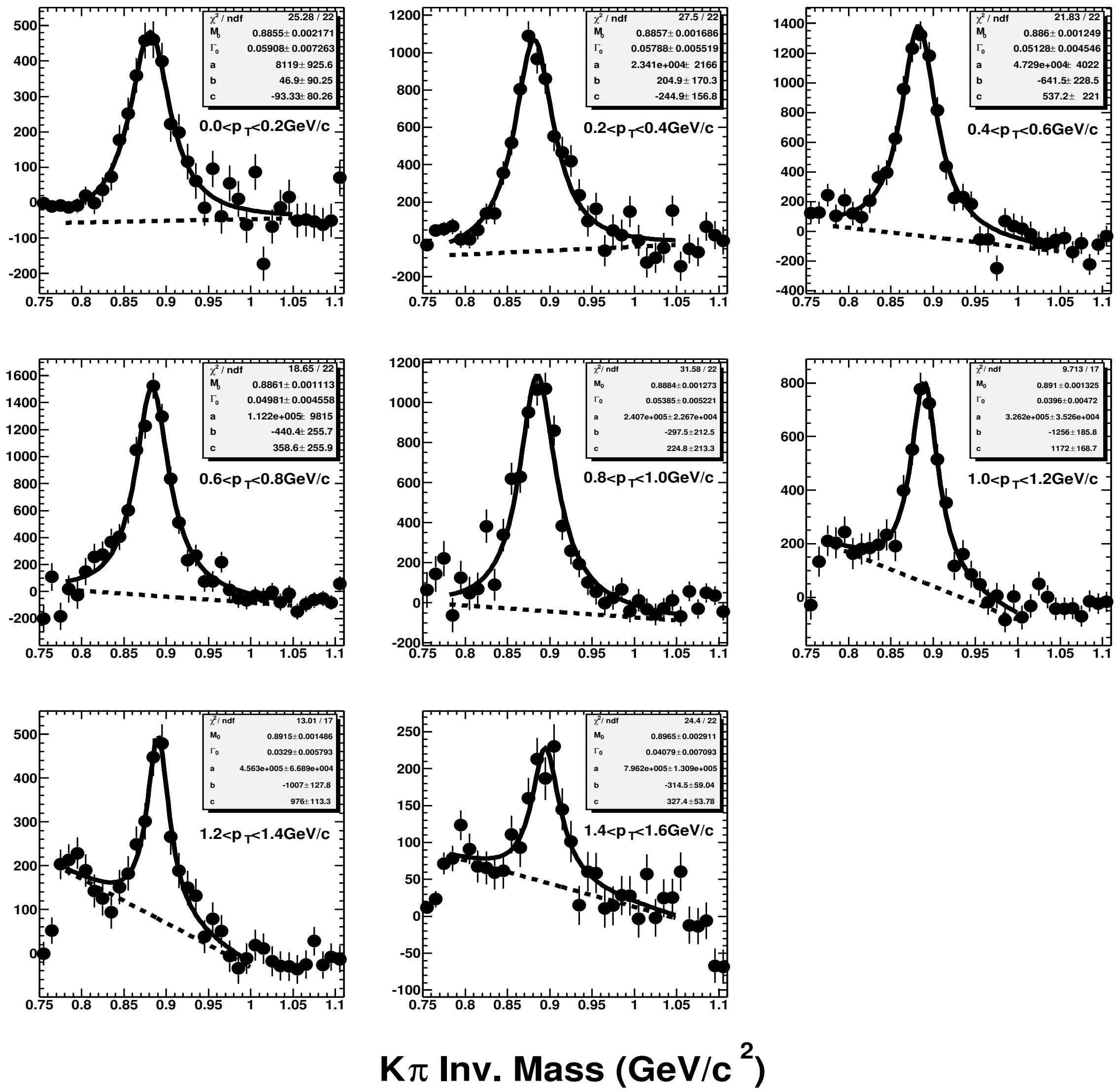

Figure 4.1: $K\pi$ invariant mass distributions from eight p_T bins fit to Equation 3.8 to extract the mass and width in minimum bias triggered p+p collisions. The solid curves stand for the fit function in Equation 3.8 and the dashed lines stand for the linear function in Equation 3.7. The units for the fit parameters M_0 and Γ_0 are GeV/c^2.

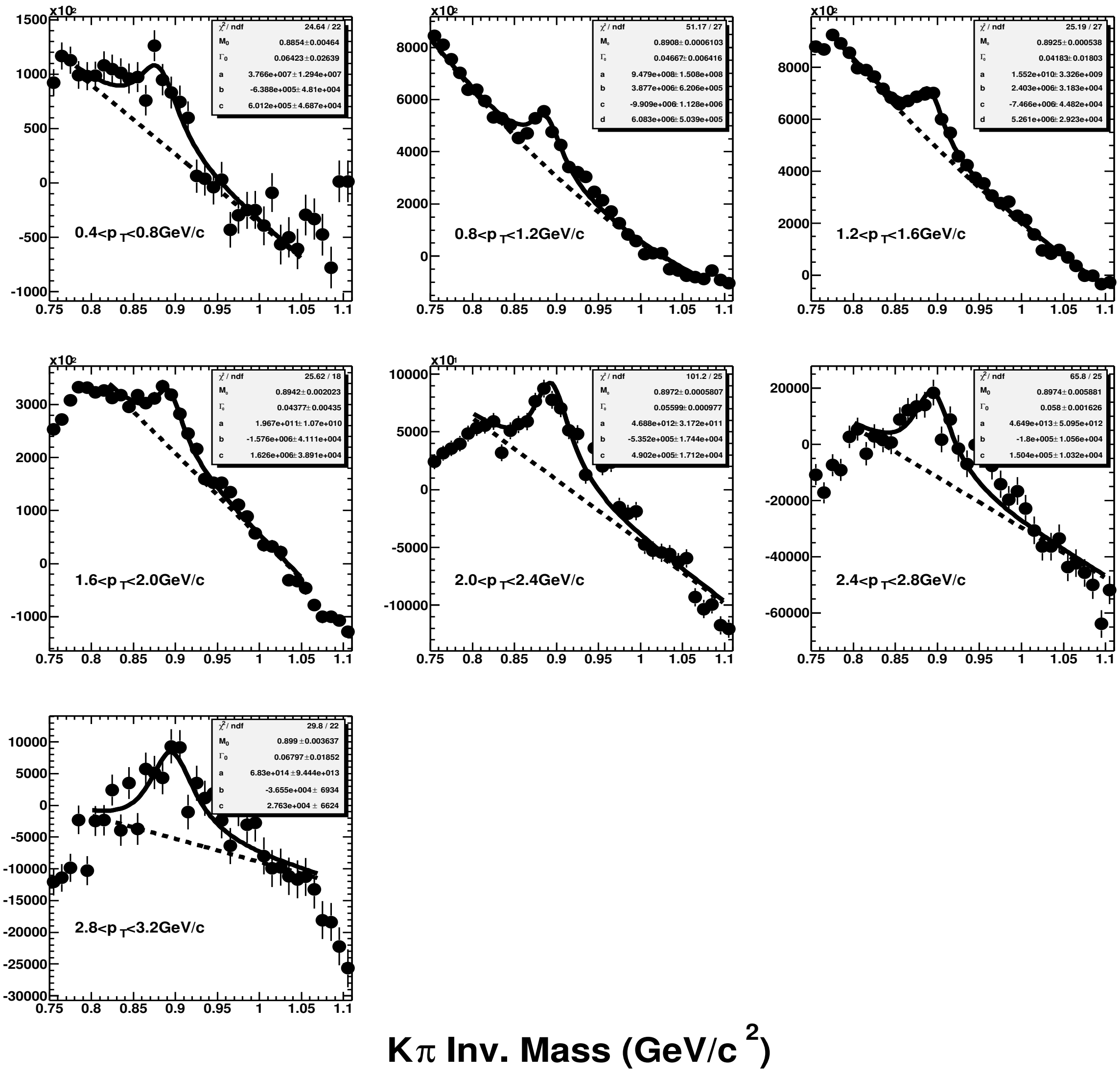

Figure 4.2: $K\pi$ invariant mass distributions from seven p_T bins fit to Equation 3.8 to extract the mass and width in top 10% central Au+Au collisions. The solid curves stand for the fit function in Equation 3.8 and the dashed lines stand for the linear function in Equation 3.7. The units for the fit parameters M_0 and Γ_0 are GeV/c^2.

Figure 4.1 shows the $K\pi$ invariant mass distribution in eight p_T bins (with each p_T bin width 0.2 GeV/c) in the p_T range between 0.0 and 1.6 GeV/c in p+p collisions. Figure 4.2 shows the $K\pi$ invariant mass distribution from seven p_T bins with bin width 0.4 GeV/c in the p_T range between 0.4 and 3.2 GeV/c in central Au+Au collisions. The fit range of the $K\pi$ invariant mass for most p_T bins is 0.78 to 1.05 GeV/c^2. In some p_T bins, the range has been slightly changed in order to get a better fit. In central Au+Au collisions, we use a second order polynomial function to describe the residual background in the two p_T bins of 0.8-1.2 GeV/c and 1.2-1.6 GeV/c to best represent the shape of the residual background.

p+p			Au+Au		
p_T	Mass±Stat±Sys	Width±Stat±Sys	p_T	Mass±Stat	Width±Stat
0.0-0.2	885.5±2.2±5.4	59.1±7.3±25	0.4-0.8	885.4±4.6	64.2±26
0.2-0.4	885.7±1.7±5.8	57.9±5.5±6	0.8-1.2	890.8±0.6	46.7±6.4
0.4-0.6	886.0±1.2±6.2	51.3±4.5±5	1.2-1.6	892.5±0.5	41.8±18
0.6-0.8	886.1±1.1±5.6	49.8±4.6±6	1.6-2.0	894.2±2.0	43.8±4.4
0.8-1.0	888.4±1.3±3.4	53.9±5.2±11	2.0-2.4	897.2±0.6	56.0±1.0
1.0-1.2	891.0±1.3±4.4	39.6±4.7±5	2.4-2.8	897.4±5.9	58.0±1.6
1.2-1.4	891.5±1.5±4.0	32.9±5.8±14	2.8-3.2	899.0±3.6	68.0±19
1.4-1.6	896.5±2.9±3.7	40.8±7.1±8			

Table 4.1: The K^{*0} mass and width for each p_T bin in minimum bias triggered p+p collisions and top 10% central triggered Au+Au collisions. The unit for p_T is GeV/c and the units for mass and width are MeV/c^2. Mass and width values in p+p collisions are listed together with statistical uncertainties and systematic uncertainties. Mass and width values in Au+Au collisions are listed with statistical uncertainties only.

The $K^{*0}(892)$ natural mass and width parameters in each p_T bin have been obtained through these fits in p+p and central Au+Au collisions and results are listed in Table 4.1. Detailed studies of systematic uncertainties in these quantities will be addressed for p+p collisions in Chapter 5. Due to limited statistics, we are unable to perform studies on systematic uncertainties for K^{*0} mass and width parameters in central Au+Au collisions. We expect that the RHIC run in 2004 for Au+Au collisions at $\sqrt{s_{NN}}$=200 GeV will provide enough statistics to precisely measure the K^{*0} mass in Au+Au collisions as a function of p_T and allow detailed study of systematic uncertainties.

The K^{*0} mass in p+p collisions (filled circle symbols) and central Au+Au collisions (star symbols) as a function of K^{*0} transverse momentum p_T are shown in Figure 4.3, in which the grey shadows represent the systematic uncertainties for the K^{*0} mass in p+p collisions and the solid straight line stands for the standard K^{*0} mass from the Particle Data Book [15] (896.1 MeV/c^2). The measured mass in each p_T bin is then compared to the mass from the Monte Carlo (MC) simulations which account for detector effects and all kinematic cuts in p+p collisions (dot-dashed curve) and central Au+Au collisions (dashed curve), respectively.

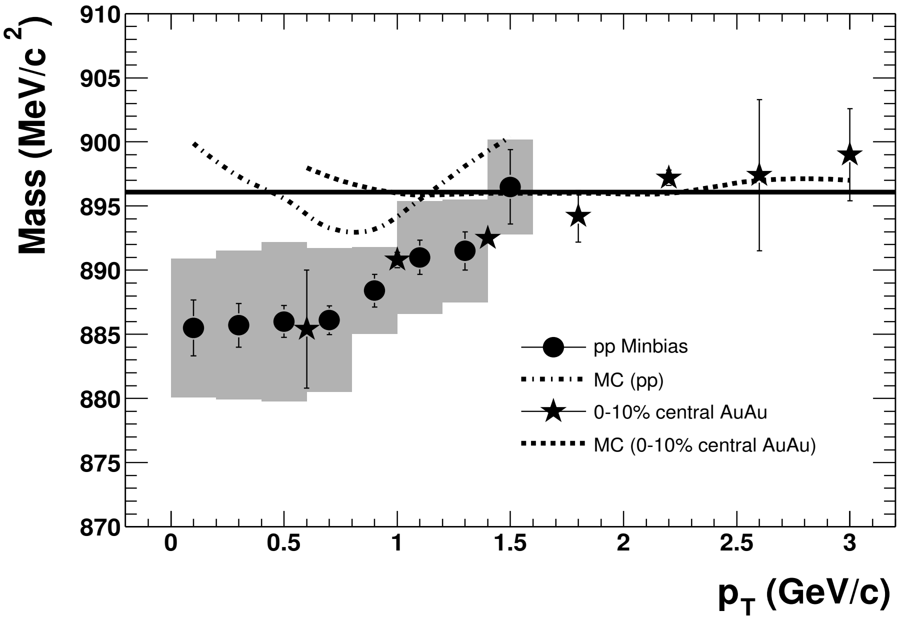

Figure 4.3: K^{*0} mass as a function of transverse momentum in p+p and top 10% central Au+Au collisions. The solid straight line stands for the standard K^{*0} mass (896.1 MeV/c^2). The dot-dashed (dashed) curve represents the MC results for K^{*0} mass in p+p (top 10% central Au+Au) collisions after considering detector effects and kinematic cuts. The grey shadows are for systematic uncertainties in p+p.

In this figure, we can see that the K^{*0} masses in both p+p and central Au+Au collisions increases as a function of p_T. In p+p collisions, the K^{*0} masses at low p_T (p_T <1.4 GeV/c) are significantly smaller than the MC results. The K^{*0} masses at p_T <1.6 GeV/c in top 10% central Au+Au collisions are also smaller than the MC results. Thus we observe a mass shift toward smaller mass at low p_T in both p+p and central Au+Au collisions and this mass shift decreases in magnitude as a function of K^{*0} transverse momentum.

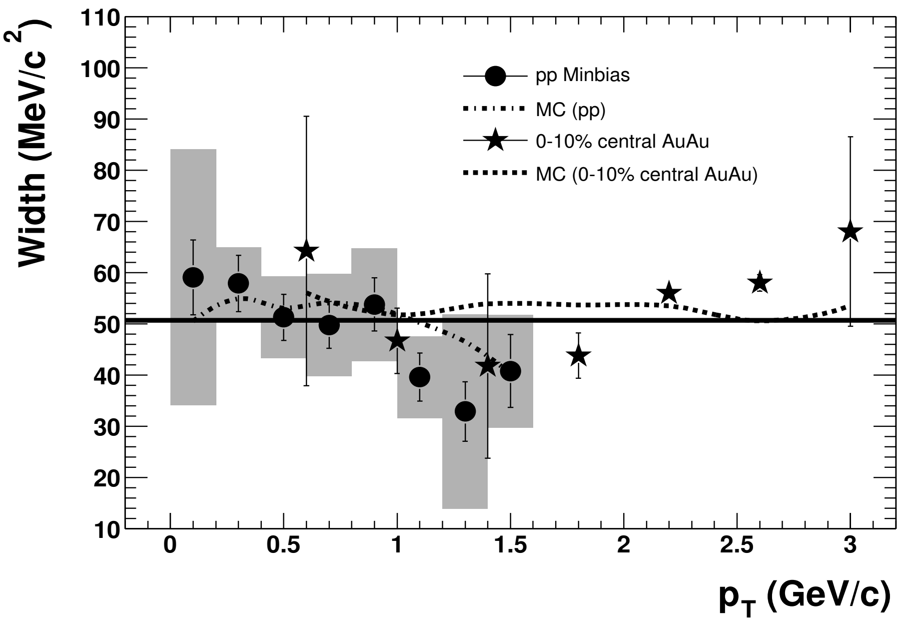

Figure 4.4: K^{*0} width as a function of transverse momentum in p+p and top 10% central Au+Au collisions. The solid straight line stands for the standard K^{*0} width (50.7 MeV/c^2). The dot-dashed (dashed) curve represents the MC results for K^{*0} width in p+p (top 10% central Au+Au) collisions after considering detector effects and kinematic cuts. The grey shadows represent systematic uncertainties in p+p.

Figure 4.4 shows the K^{*0} width as a function of p_T in p+p collisions (filled circle symbols) with systematic uncertainties (grey shadows) and central Au+Au collisions (star symbols). The straight line stands for the standard K^{*0} width from the Particle Data Book [15] which is 50.7 MeV/c^2. The measured K^{*0} width parameters are also compared to the MC results in p+p collisions (dot-dashed curve) and top 10% central Au+Au collisions (dashed curve), respectively. In this figure, we cannot see any significant difference between the measured K^{*0} width and the MC results in both p+p and Au+Au collisions. Thus no K^{*0} width broadening effect can be observed in either p+p or central Au+Au collisions.

4.2 Transverse Mass Spectra in Au+Au and p+p Collisions

The K^{*0} raw yields in each p_T bin at mid-rapidity ($|y| < 0.5$) are measured using the method described in Section 3.7 in top 10% central Au+Au, as well as in four different centralities (0-10%, 10%-30%, 30%-50% and 50%-80%) in minimum bias triggered Au+Au and minimum bias triggered p+p collisions at $\sqrt{s_{NN}}$=200 GeV.
Figure 4.5 shows the $K\pi$ invariant mass distributions from seven p_T bins with bin width 0.4 GeV/c in the p_T range between 0.4 and 3.2 GeV/c in central Au+Au collisions. The $K\pi$ invariant mass distributions from each p_T bin in the four centralities in minimum bias triggered Au+Au collisions have shapes similar to the distributions in central Au+Au collisions. Figure 4.6 shows the $K\pi$ invariant mass distributions from eight p_T bins with bin width 0.2 GeV/c in the p_T range between 0.0 and 1.6 GeV/c in p+p collisions.
Using the fit with the simplified Breit-Wigner function together with a linear function (second order polynomial function for two p_T bins in Au+Au collisions) representing the residual background as shown in Equation 3.10, the $K^{*0} + \overline{K^{*0}}$ raw yields are extracted for each p_T bin. Figure 4.7 shows the $(K^{*0} + \overline{K^{*0}})/2$ raw invariant yields $1/(2\pi)d^2N_{\mathrm{raw}}/p_T dp_T dy$ normalized by the total number of collision events at mid-rapidity $|y| < 0.5$ as a function of p_T in top 10% central triggered Au+Au, four centralities 0-10%, 10%-30%, 30%-50% and 50%-80% in minimum bias Au+Au and minimum bias p+p collisions. The data points for the top 10% central triggered Au+Au collisions are scaled by a factor of 2 in order to more easily show any difference of the 0-10% centrality bin in minimum bias Au+Au collisions.
The raw invariant yields in each p_T bin are then corrected for the total reconstruction efficiencies (as shown in Section 3.8) and the decay branching ratios. From the Particle Data Book [15], we find that ~100% of the K^{*0} mesons decay into the two $K\pi$ channels: (1) the decay channel into two oppositely charged daughters $K^{*0} \rightarrow K^+\pi^-$ and (2) the decay channel into two neutral daughters $K^{*0} \rightarrow K^0\pi^0$. Isospin calculations (Appendix B) show that 2/3 of the K^{*0} mesons decay into the channel with oppositely charged daughters and 1/3 decay into the channel with neutral daughters.

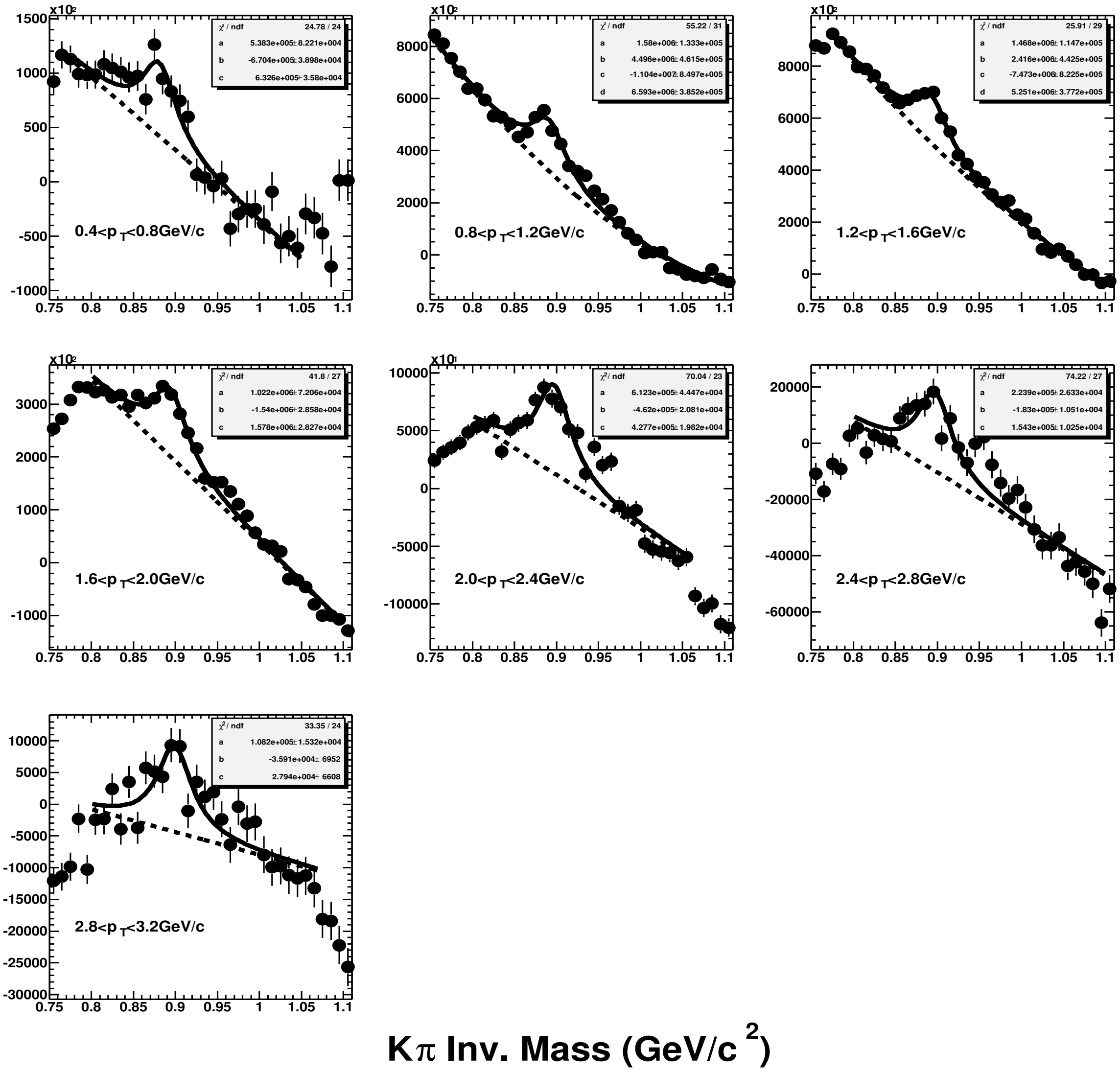

Figure 4.5: The $K\pi$ invariant mass distributions from seven p_T bins fit to Equation 3.9 to extract yield in top 10% central Au+Au collisions. The solid curves stand for the fit function in Equation 3.9 and the dashed lines stand for the linear function in Equation 3.7.

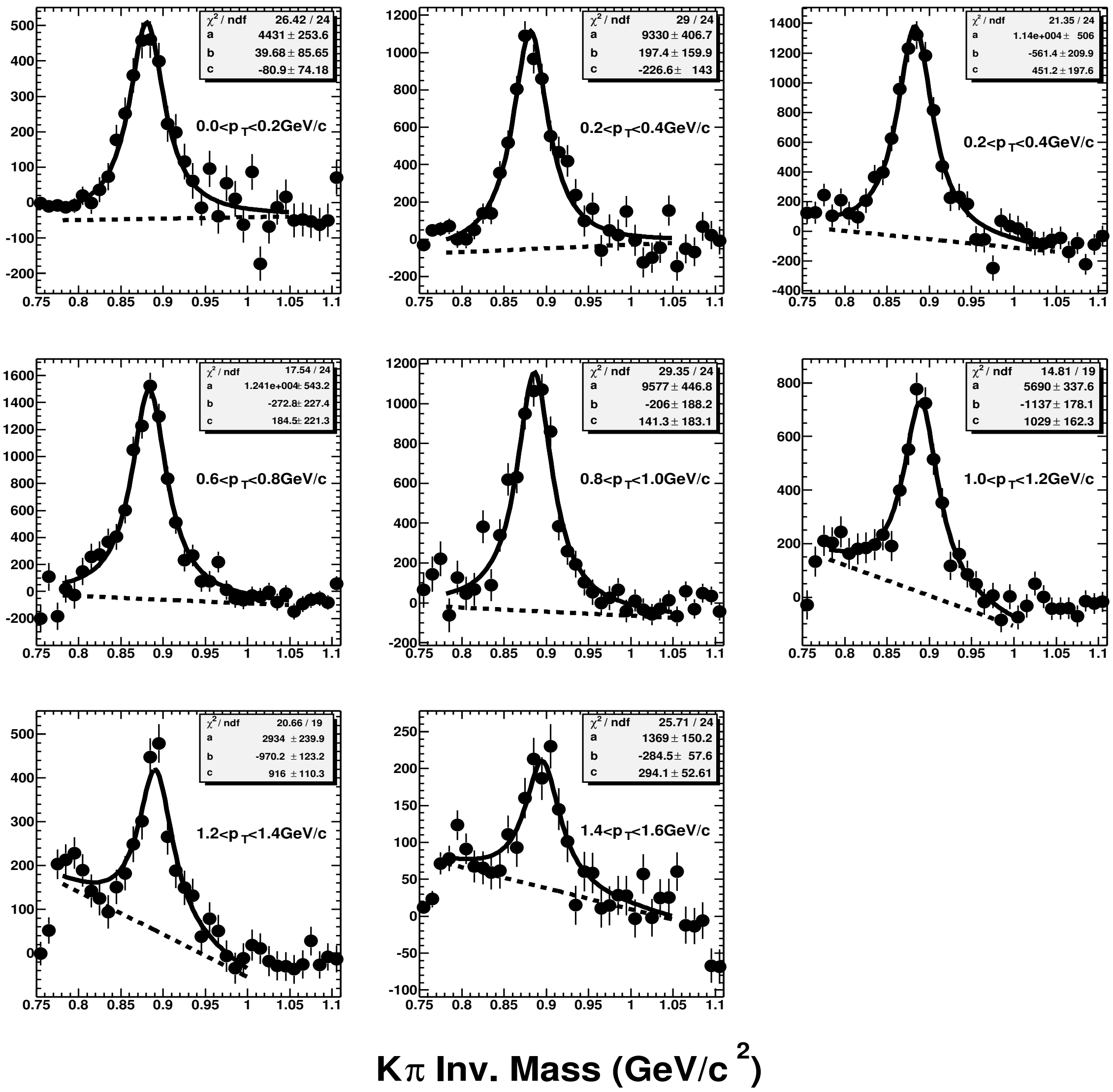

Figure 4.6: The $K\pi$ invariant mass distributions from eight p_T bins fit to Equation 3.9 to extract yield in p+p collisions. The solid curves stand for the fit function in Equation 3.9 and the dashed lines stand for the linear function in Equation 3.7.

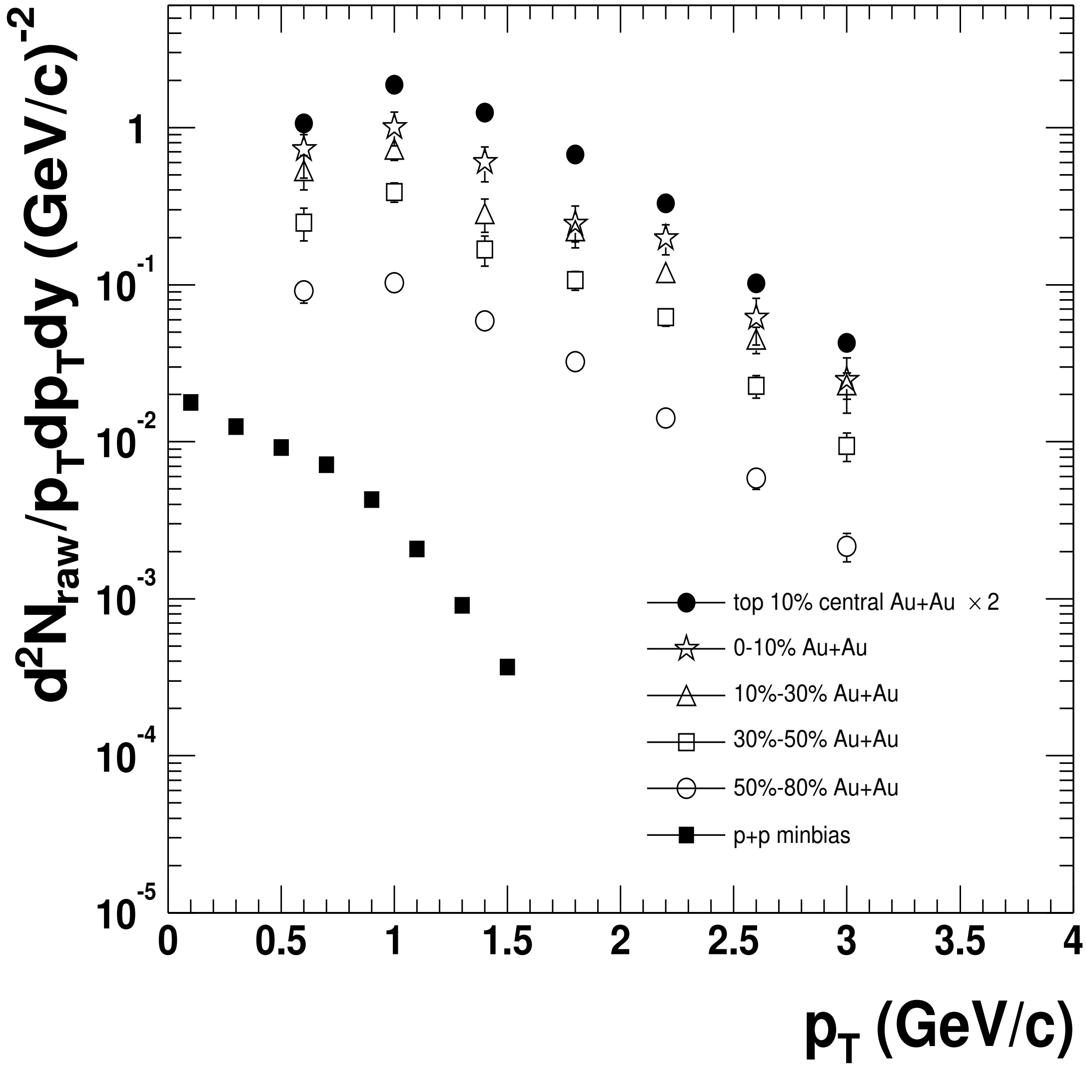

Figure 4.7: The $(K^{*0} + \overline{K^{*0}})/2$ raw yield $d^2N_{\text{raw}}/p_T dp_T dy$ as functions of p_T at mid-rapidity ($|y| < 0.5$) in p+p collisions and Au+Au collisions with different centralities.

Thus the K^{*0} yields have to be corrected by the branching ratio 2/3 since we measured the K^{*0} through the channel with two oppositely charged daughters.
The K^{*0} transverse mass m_T is defined as

$$m_T = \sqrt{m_0^2 + p_T^2} \tag{4.1}$$

in which m_0 is the K^{*0} natural mass 896.1 MeV/c^2 and p_T is the transverse momentum. We can see that

$$p_T dp_T = \frac{\sqrt{m_0^2 + p_T^2}}{2\sqrt{m_0^2 + p_T^2}} dp_T^2 = m_T dm_T \tag{4.2}$$

The total reconstruction efficiency and decay branching ratio corrected $(K^{*0} + \overline{K^{*0}})/2$ invariant yield at mid-rapidity is then

$$\frac{1}{2\pi p_T}\frac{d^2N}{dydp_T} = \frac{1}{2\pi m_T}\frac{d^2N}{dydm_T} \tag{4.3}$$

Table 4.2 lists the $(K^{*0} + \overline{K^{*0}})/2$ invariant yields $[1/(2\pi m_T)][d^2N/dydm_T]$ at mid-rapidity in each $m_T - m_0$ bin in central Au+Au and p+p collisions. Table 4.3 lists

$m_T - m_0$ (MeV/c^2)	top 10% central triggered Au+Au	$m_T - m_0$ (MeV/c^2)	minimum bias triggered p+p
0.182	1.21±0.19	0.006	(4.09±0.65)×10^{-2}
0.447	1.14±0.10	0.049	(3.09±0.35)×10^{-2}
0.766	(5.24±0.41)×10^{-1}	0.130	(2.26±0.22)×10^{-2}
1.115	(2.36±0.17)×10^{-1}	0.241	(1.21±0.10)×10^{-2}
1.479	(1.05±0.08)×10^{-1}	0.374	(6.70±0.57)×10^{-3}
1.854	(3.07±0.38)×10^{-2}	0.523	(3.68±0.39)×10^{-3}
2.235	(1.24±0.19)×10^{-2}	0.683	(1.77±0.22)×10^{-3}
		0.851	(9.90±0.17)×10^{-4}

Table 4.2: The $(K^{*0} + \overline{K^{*0}})/2$ invariant yields $[1/(2\pi m_T)][d^2N/dydm_T]$ at mid-rapidity in each $m_T - m_0$ bin in top 10% central Au+Au and minimum bias p+p collisions.

the $(K^{*0} + \overline{K^{*0}})/2$ invariant yields at mid-rapidity in each $m_T - m_0$ bin in 0-10%, 10%-30%, 30%-50% and 50%-80% centralities in minimum bias Au+Au collisions. The m_T for each $m_T - m_0$ bin is calculated from Equation 4.1 using the bin center

$m_T - m_0$	minimum bias triggered Au+Au			
(MeV/c^2)	0-10%	10%-30%	30%-50%	50%-80%
0.182	1.66±0.57	1.01±0.25	(4.37±1.04)×10^{-1}	(1.43±0.25)×10^{-1}
0.447	1.23±0.30	(7.30±1.10)×10^{-1}	(3.52±0.49)×10^{-1}	(8.69±1.10)×10^{-2}
0.766	(5.08±1.23)×10^{-1}	(2.01±0.48)×10^{-1}	(1.05±0.23)×10^{-1}	(3.54±0.50)×10^{-2}
1.115	(1.71±0.51)×10^{-1}	(1.29±0.20)×10^{-1}	(5.48±0.76)×10^{-2}	(1.69±0.20)×10^{-2}
1.479	(1.25±0.28)×10^{-1}	(6.11±0.88)×10^{-2}	(2.94±0.37)×10^{-2}	(6.21±0.83)×10^{-3}
1.854	(3.70±1.23)×10^{-2}	(2.23±0.43)×10^{-2}	(9.91±1.68)×10^{-3}	(2.47±0.41)×10^{-3}
2.235	(1.43±0.55)×10^{-2}	(1.13±0.22)×10^{-2}	(3.89±0.83)×10^{-3}	(8.70±2.00)×10^{-4}

Table 4.3: The $(K^{*0} + \overline{K^{*0}})/2$ invariant yields $[1/(2\pi m_T)][d^2N/dydm_T]$ at mid-rapidity in each $m_T - m_0$ bin in 0-10%, 10%-30%, 30%-50% and 50%-80% centralities in minimum bias Au+Au collisions.

of each corresponding p_T bin.

Figure 4.8 shows the transverse mass distributions of the $(K^{*0} + \overline{K^{*0}})/2$ invariant yields at mid-rapidity ($|y|$ <0.5) in central Au+Au, four centralities (0-10%, 10%-30%, 30%-50% and 50%-80%) in minimum bias Au+Au, and p+p collisions. The distributions show an exponentially decreasing behavior with m_T and we would like to use an exponential function to fit the distributions to extract the K^{*0} mid-rapidity yield dN/dy and the inverse slope parameter T. Thus we define an exponential function in Equation 4.4

$$\frac{1}{2\pi m_T}\frac{d^2N}{dydm_T} = a \times e^{-(m_T-m_0)/b} \tag{4.4}$$

It's obvious that the parameter b in the above equation is the inverse slope parameter T. In order to get dN/dy, we integrate both sides of Equation 4.4 with respect to transverse mass and get

$$\int_{m_0}^{+\infty} \frac{1}{2\pi m_T}\frac{d^2N}{dydm_T} m_T dm_T = \frac{1}{2\pi}\frac{dN}{dy} \tag{4.5}$$

$$\int_{m_0}^{+\infty} a \times e^{-(m_T-m_0)/T} m_T dm_T = aT(m_0 + T) \tag{4.6}$$

So we have

$$a = \frac{dN/dy}{2\pi T(m_0 + T)} \tag{4.7}$$

Then we can use the exponential function shown in the right side of Equation 4.8 to fit the K^{*0} transverse mass distributions in Figure 4.8

$$\frac{1}{2\pi m_T}\frac{d^2N}{dydm_T} = \frac{dN/dy}{2\pi T(m_0+T)}e^{-(m_T-m_0)/T} \tag{4.8}$$

The two open parameters in the above fit function are the K^{*0} mid-rapidity yield dN/dy and the inverse slope parameter T.
Through the exponential fit, we extract the K^{*0} yield dN/dy at mid-rapidity $|y| < 0.5$ and the inverse slope parameter T in central Au+Au, minimum bias Au+Au and p+p collisions and results are listed in Table 4.4. The mid-rapidity yield dN/dy and the

	dN/dy	T (MeV)
top 10% central	10.18±0.46±1.58	427.0±9.7±46.4
0-10%	10.48±1.45±1.63	428.1±30.9±46.5
10%-30%	5.86±0.56±0.91	446.2±22.5±48.5
30%-50%	2.81±0.25±0.44	427.0±18.2±46.4
50%-80%	0.815±0.059±0.127	401.8±14.4±43.6
p+p	$(5.93\pm0.23\pm0.39)\times10^{-2}$	223.4±9.1±9.1

Table 4.4: The K^{*0} mid-rapidity yield dN/dy and the inver slope parameter T in top 10% central Au+Au, four centralities 0-10%, 10%-30%, 30%-50% and 50%-80% in minimum bias Au+Au and minimum bias p+p collisions.

inverse slope parameter T in Table 4.4 are listed as "values ± statistical uncertainties ± systematic uncertainties". Detailed studies concerning systematic uncertainties are discussed in Chapter 5.
In Table 4.4, we can see that the K^{*0} mid-rapidity yield dN/dy is increasing from p+p collisions to peripheral Au+Au collisions to central Au+Au collisions. The inverse slope parameters, T, in Au+Au collisions are significantly larger than in p+p collisions. It is consistent with the UrQMD model predictions [28] that the K^* daughter particles' re-scattering effect is p_T dependent. Although with larger statistical uncertainties, the dN/dy and T values extracted in the 0-10% centrality bin in minimum bias Au+Au collisions match the results in top 10% central Au+Au collisions within uncertainties.

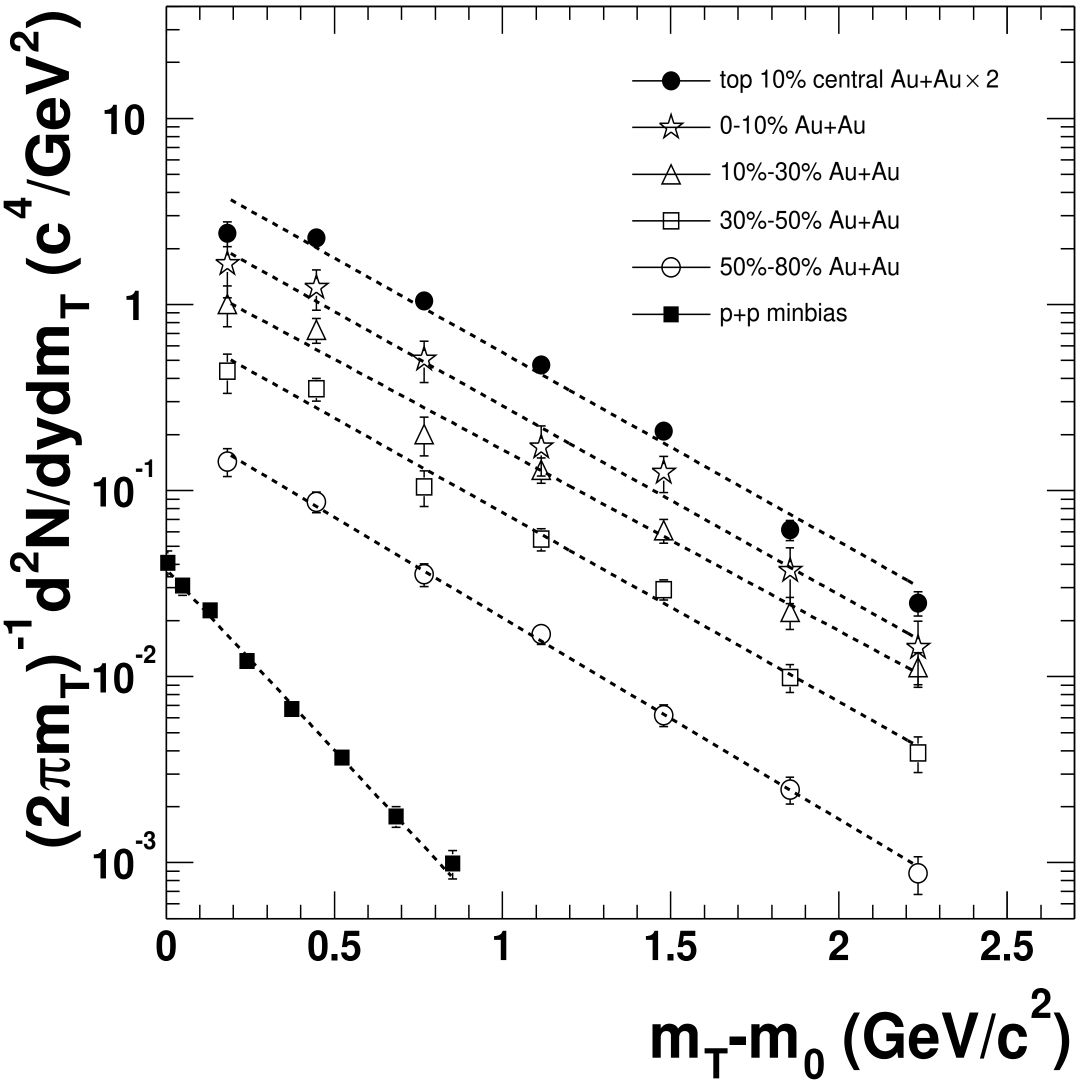

Figure 4.8: The $(K^{*0} + \overline{K^{*0}})/2$ efficiency corrected invariant yields as functions of $m_T - m_0$ at mid-rapidity ($|y| < 0.5$). This is fit to Equation 4.8 to extract dN/dy and the inverse slope parameters in p+p and Au+Au collisions. The dashed lines represent the fit function in Equation 4.8.

4.3 Transverse Momentum Spectrum in p+p Collisions

In p+p collisions, theoretical calculations indicate that particle production is dominated by hard processes, such as gluon fusion, mini-jets, etc., at moderate p_T ($\sim$1.5 $< p_T <$ 4 GeV/c) while soft processes dominate at low p_T ($p_T <$ 1.5GeV/c) [62]. Thus we expect to observe a power-law shape in the p_T distribution at $p_T >$ 1.5 GeV/c of the K^* invariant yield $1/(2\pi p_T)d^2N/dydp_T$ at mid-rapidity because hard processes give a power-law shape.

In p+p collisions, due to the fact that we cut on the kaon daughter momentum $p <$ 0.7 GeV/c, we only measure the K^{*0} spectrum for $p_T <$ 1.6 GeV/c. In this range, the soft processes dominate, so that the simple exponential function can fit the K^{*0} transverse mass spectrum well. Fortunately, we can measure the $K^{*\pm}$ signals with p_T up to 4.0 GeV/c so that we can test whether the overall K^* transverse momentum can be well fit by a power-law function or not.

Figure 4.9 shows the $K^0_S\pi^{\pm}$ invariant mass distributions for six p_T bins in the p_T range between 0.6 and 4.0 GeV/c in p+p collisions. The invariant mass distribution for each p_T bin is fit with a simplified Breit-Wigner function plus a linear function representing the residual background, as shown in Equation 3.10, to extract the $K^{*\pm}$ yields in each p_T bin. In Equation 3.10, we fix the $K^{*\pm}$ mass (M_0= 891.7 MeV/c^2) and the full width (Γ_0= 50.8 MeV/c^2) according to the Particle Data Book. Figure 4.10 shows the $(K^{*+}+K^{*-})/2$ together with the $(K^{*0}+\overline{K^{*0}})/2$ raw yield, $d^2N_{\mathrm{raw}}/dydp_T$, as a function of p_T in p+p collisions.

The raw yields for $K^{*\pm}$ in each p_T bin are then corrected for the total reconstruction efficiencies and the decay branching ratios. In the case of K^{*+}, $\sim$100% of the K^{*+} meson decays into the two following $K\pi$ channels: (1) the decay channel with a neutral kaon $K^{*+}\rightarrow K^0\pi^+$ and (2) the decay channel with a neutral pion $K^{*+}\rightarrow K^+\pi^0$. Isospin calculations (Appendix B) show that 2/3 of the K^{*+} mesons decay into the neutral kaon channel and 1/3 decay into the neutral pion channel. Since we measure the K^{*+} signal by selecting the K^0_S candidates via $K^0_S\rightarrow\pi^+\pi^-$, we also have to consider that only half of the K^0 mesons decay as a K^0_S and the other half decay

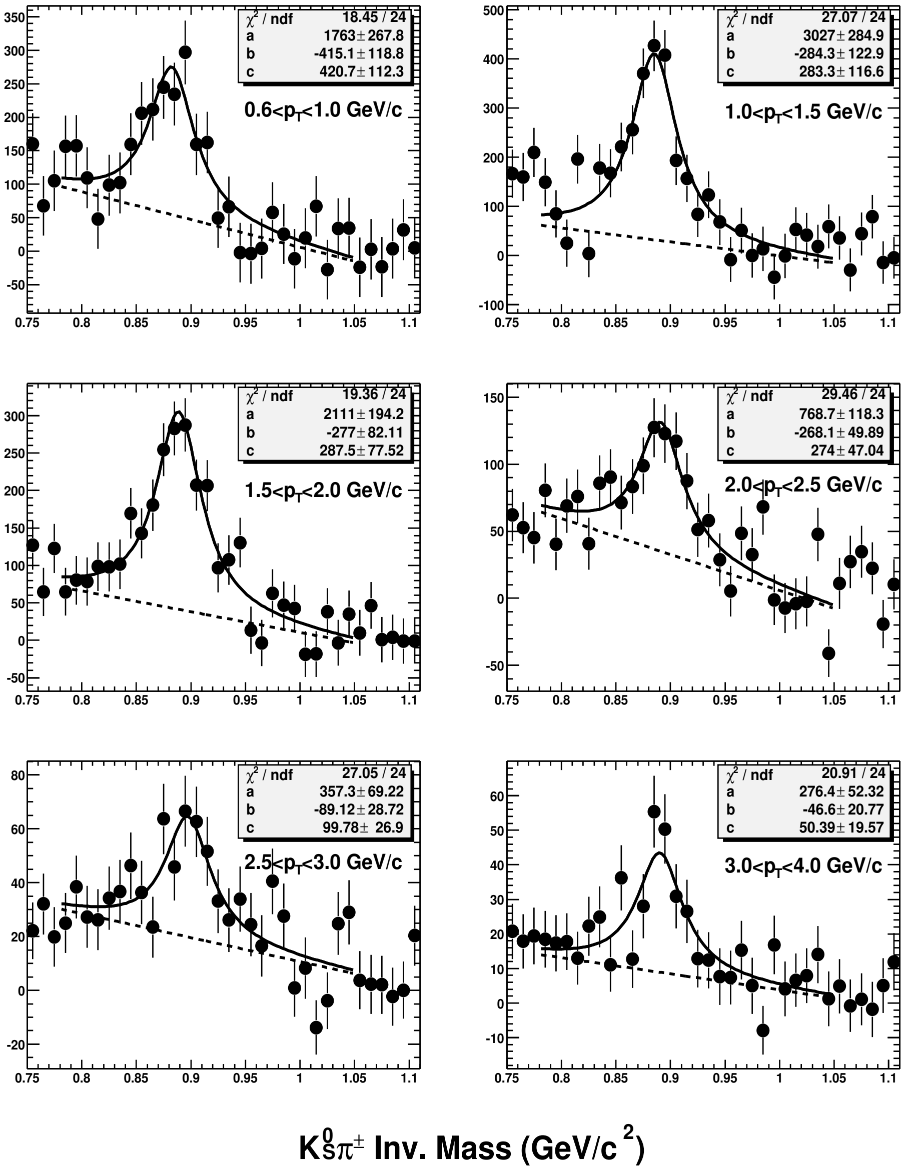

Figure 4.9: The $K_S^0\pi^\pm$ invariant mass distributions from six p_T bins fit to Equation 3.9 to extract yield in p+p collisions. The solid curves stand for the fit function in Equation 3.9 and the dashed lines stand for the linear function in Equation 3.7.

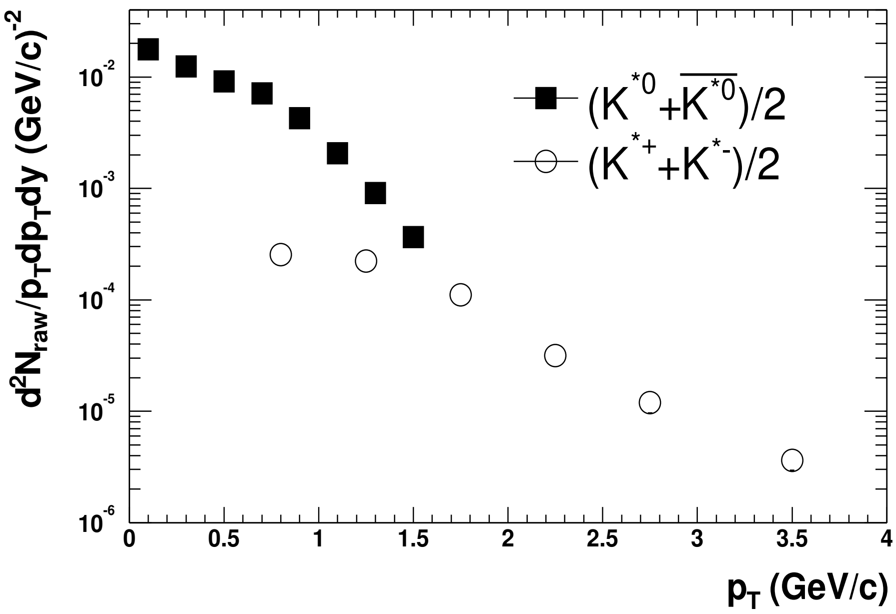

Figure 4.10: The $(K^{*0} + \overline{K^{*0}})/2$ and $(K^{*+} + \overline{K^{*0-}})/2$ raw yield $d^2N_{\rm raw}/p_T dp_T dy$ as functions of p_T at mid-rapidity ($|y| < 0.5$) in p+p collisions.

p_T (GeV/c)	$(K^{*+} + K^{*-})/2$	p_T (GeV/c)	$(K^{*0} + \overline{K^{*0}})/2$
0.6-1.0	$(6.88\pm1.04)\times10^{-3}$	0.0-0.2	$(4.09\pm0.65)\times10^{-2}$
1.0-1.5	$(2.97\pm0.28)\times10^{-3}$	0.2-0.4	$(3.09\pm0.35)\times10^{-2}$
1.5-2.0	$(8.81\pm0.81)\times10^{-4}$	0.4-0.6	$(2.26\pm0.22)\times10^{-2}$
2.0-2.5	$(2.52\pm0.39)\times10^{-4}$	0.6-0.8	$(1.21\pm0.10)\times10^{-2}$
2.5-3.0	$(8.15\pm1.57)\times10^{-5}$	0.8-1.0	$(6.70\pm0.57)\times10^{-3}$
3.0-4.0	$(1.75\pm0.33)\times10^{-5}$	1.0-1.2	$(3.68\pm0.39)\times10^{-3}$
		1.2-1.4	$(1.77\pm0.22)\times10^{-3}$
		1.4-1.6	$(9.90\pm0.17)\times10^{-4}$

Table 4.5: The $(K^{*+}+K^{*-})/2$ and $(K^{*0}+\overline{K^{*0}})/2$ invariant yields $1/(2\pi p_T)d^2N/dydp_T$ at mid-rapidity in each p_T bin in minimum bias p+p collisions.

as a K_L^0 which we do not observe. The branching ratio for $K_S^0 \to \pi^+\pi^-$ is 68.61% according to the Particle Data Book [15]. The total decay branching ratio is then 2/3×1/2×68.61%=22.87%. Similar calculations also lead to a total decay branching ratio 22.87% in the case of K^{*-}.

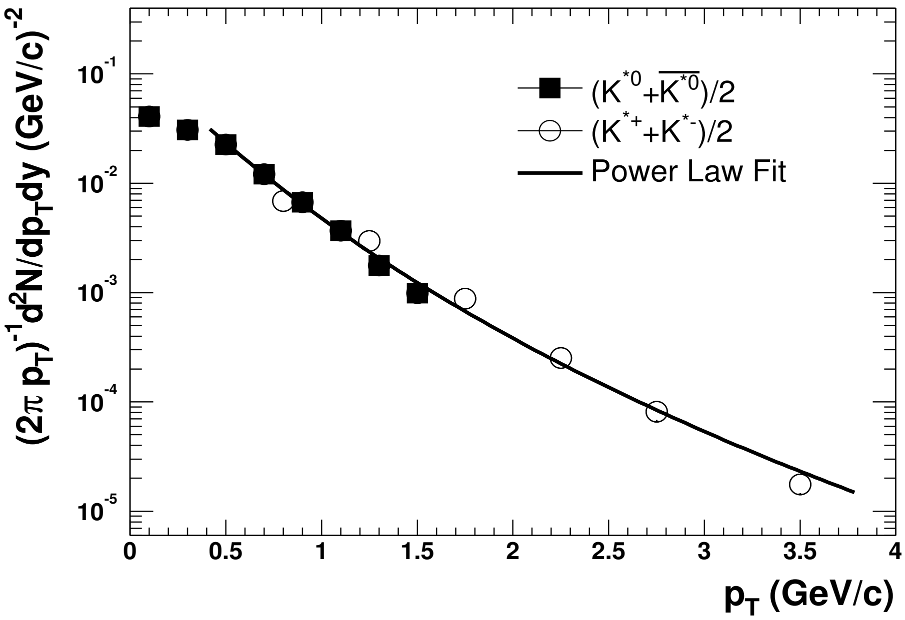

Figure 4.11: The invariant yields for both $(K^{*0} + \overline{K^{*0}})/2$ and $(K^{*+} + \overline{K^{*-}})/2$ as a function of p_T at mid-rapidity ($|y| < 0.5$), fit to Equation 4.9 to extract $\langle p_T \rangle$ in p+p collisions.

The invariant yields, $[1/(2\pi p_T)][d^2N/dydp_T]$ at mid-rapidity in each p_T bin in p+p collisions are listed in Table 4.5 and are shown in Figure 4.11 for both $(K^{*+}+K^{*-})/2$ and $(K^{*0} + \overline{K^{*0}})/2$. The K^* overall spectrum in the range p_T >0.5 GeV/c is then fit with a power-law function defined in the right side of Equation 4.9

$$\frac{1}{2\pi p_T}\frac{d^2N}{dydp_T} = a(1 + \frac{p_T}{\langle p_T \rangle \frac{n-3}{2}})^{-n} \tag{4.9}$$

in which the parameter a is a constant value proportional to the mid-rapidity yield, the parameter n is the order of the power law and $\langle p_T \rangle$ is the mean value of the transverse momentum which is extracted from the fit.

The first two data points for $(K^{*0}+\overline{K^{*0}})/2$ in the p_T bins of 0.0-0.2 GeV/c and 0.2-0.4

GeV/c cannot be well fit by the power-law function due to the reason that in the very low p_T region particle production is dominated by soft processes while the power-law function is to describe hard processes. We don't calculate the K^* mid-rapidity yield, dN/dy, using the extracted parameter a because the yield is mainly determined by the low p_T part for which this fit does not work well.

In Figure 4.11, we can see that the K^* transverse momentum spectrum is well fit by the power-law function in the range $p_T > 0.5$ GeV/c indicating that the hard processes are the dominant processes at the intermediate p_T region for K^* production in p+p collisions. The mean transverse momentum extracted from the power-law fit is 695.5±21.6 MeV/c.

4.4 Particle Ratios

The quark contents of the $K^*(892)$ resonances are $d\overline{s}$ (K^{*0}), $\overline{d}s$ ($\overline{K^{*0}}$), $u\overline{s}$ (K^{*+}) and $\overline{u}s$ (K^{*-}), while the quark contents for the ground state K mesons are $d\overline{s}$ (K^0), $\overline{d}s$ ($\overline{K^0}$), $u\overline{s}$ (K^+) and $\overline{u}s$ (K^-). Thus the K^* resonance and the stable K meson with the same charge have identical quark content. The K^* resonance is a vector meson with total spin S=1 while the stable K is a pseudo-scalar meson with total spin S=0. Since the pseudo-scalar and vector mesons differ only in the relative orientation of the quark spins, the difference in their masses must be attributed to spin-related interactions. Thus the masses of the pseudo-scalar and vector mesons can be approximately calculated by the following meson mass formula [63]

$$M(\text{meson}) = m_1 + m_2 + A\frac{(\vec{S_1}\cdot\vec{S_2})}{m_1 m_2} \tag{4.10}$$

in which A is a fit parameter, m and $\vec{S}$ represent the mass and the spin of a quark, the subscripts 1 and 2 stand for the two quarks in the meson. The spin-related term is

$$\vec{S_1}\cdot\vec{S_2} = \begin{cases} 1/4\hbar^2 & \text{for vector mesons,} \\ -3/4\hbar^2 & \text{for pseudo-scalar mesons.} \end{cases} \tag{4.11}$$

In the case of the K^* resonance and the stable K meson, by selecting $m_u = m_d =$ 310 MeV/c^2 and $m_s =$ 483 MeV/c^2, we obtain $M_{K^*} =$ 896 MeV/c^2 and $M_K =$ 484

MeV/c^2 whereas the observed meson masses are $M_{K^{*0}} = 896.1$ MeV/c^2 and $M_{K^0_S} = 497.7$ MeV/c^2. Thus by measuring the K^*/K ratio in relativistic heavy ion collisions, we can probe the spin-related interactions under extreme conditions.

As discussed in Section 1.2.3, due to the resonance daughter particles' re-scattering effects and resonance re-generation effects in the hadron gas medium, the measurements of resonance yields compared to their corresponding stable particles, such as K^*/K, ρ/π, Δ/p, etc, can give us information on the fireball evolution between chemical and kinetic freeze-out in relativistic heavy ion collisions.

The K^* and ϕ mesons have a very small mass difference and their total spin difference is ΔS =0. The quark content for the ϕ meson is $s\bar{s}$. Thus the ϕ/K^* ratio might be a good signature to study the strangeness enhancement effect in relativistic heavy ion collisions [55].

The kaon [64] and ϕ [65] production in Au+Au and p+p collisions at $\sqrt{s_{NN}}$=200 GeV have also been measured using the STAR detector at RHIC. Thus the K^*/K and ϕ/K^* particle ratios can be calculated for different centralities in Au+Au collisions and in p+p collisions. The results are listed in Table 4.6. In the ratio calculations, we use the $(K^{*0} + \overline{K^{*0}})/2$ mid-rapidity yields dN/dy as the K^* yields and use the $(K^+ + K^-)/2$ mid-rapidity yields dN/dy as the K yields. The ϕ meson mid-rapidity yields dN/dy are used as the ϕ yields. The uncertainties shown in the table are the square root of the quadratic sum of the corresponding statistical and systematic uncertainties. The K^* yields in 0-10% centrality are the results in top 10% central

	K^*/K	ϕ/K^*
0-10%	0.2046±0.0333	0.5953±0.1231
10%-30%	0.2195±0.0401	0.6331±0.1384
30%-50%	0.2550±0.0458	0.5836±0.1313
50%-80%	0.2690±0.0464	0.5276±0.1058
p+p	0.3889±0.0286	0.4553±0.0629

Table 4.6: The K^*/K and ϕ/K^* ratios for different centralities in Au+Au collisions and in p+p collisions.

Au+Au collisions.

Figure 4.12 shows the K^*/K, ϕ/K^*, ρ/π [66] and Δ/p [67] ratios as a function of

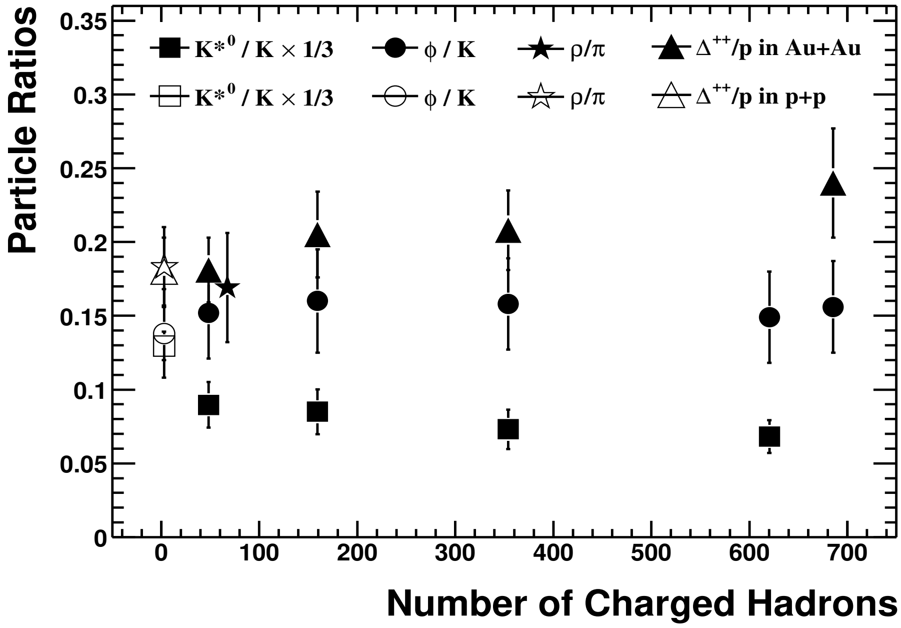

Figure 4.12: The K^{*0}/K, ϕ/K^{*0}, ρ/π and Δ/p ratios as a function of number of charged hadrons in p+p (open symbols) and Au+Au (solid symbols) collisions.

number of charged hadrons in Au+Au and p+p collisions. In this figure, we can see that the K^*/K ratios in Au+Au collisions are about a factor of 2 smaller than the ratio in p+p collisions. This K^*/K ratio suppression in Au+Au collisions might be due to the fact that the K^* daughter particles' re-scattering effect destroys part of the K^* signal. Detailed discussions about this issue will be addressed in Section 6.2. In Au+Au collisions, although the K^*/K ratio slightly decreases as a function of number of charged hadrons, the decrease is not significant due to the uncertainties of the data points. The ρ/π and Δ/p ratios are also shown in this figure for comparison and their physics implications will be discusses in Chapter 6.

Figure 4.13 and Figure 4.14 show the K^*/K and ϕ/K^* ratios in different collision systems at various collision energies [68, 69, 70, 71, 72, 73, 74, 75, 76], respectively. The K^*/K and ϕ/K^* ratios at $\sqrt{s_{NN}}$ = 200 GeV are the ratios in top 10% central Au+Au collisions and the ratios at $\sqrt{s_{NN}}$= 130 GeV [55] are in the top 14% central Au+Au collisions. In Figure 4.13, we can see that the K^*/K ratios in elementary collisions are flat as a function of $\sqrt{s}$ considering uncertainties, whereas the K^*/K

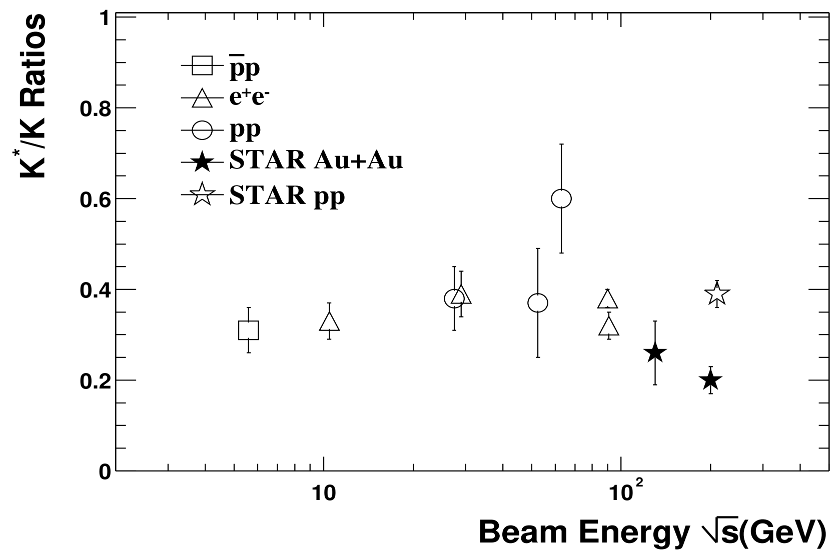

Figure 4.13: The K^{*0}/K ratios in different collision systems with various collision energies.

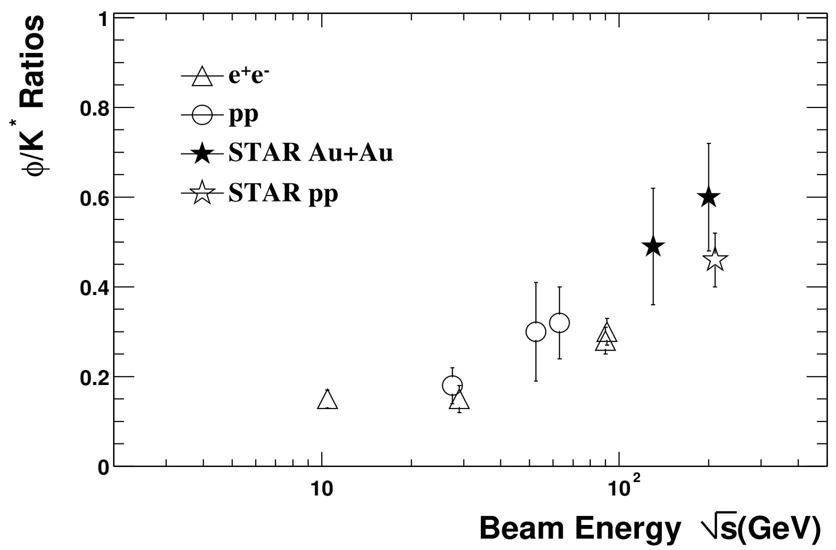

Figure 4.14: The ϕ/K^{*0} ratios in different collision systems with various collision energies.

ratio in Au+Au collisions at $\sqrt{s_{NN}} = 200$GeV is significantly smaller than the ratios in elementary collisions. In Figure 4.14, we can see that the ϕ/K^* ratio increases as a function of collision energy.

4.5 $\langle p_T \rangle$ Distribution

In the hadron phase between chemical and kinetic freeze-out, the resonances with higher p_T have a greater chance to escape the hadron medium, decay outside the fireball and avoid the daughter particles' re-scattering effects so that high p_T resonances have a greater chance to be detected than low p_T resonances [28]. Thus we expect to measure a higher $\langle p_T \rangle$ distribution in relativistic heavy ion collisions than in elementary collisions, such as p+p collisions.

Since we have measured the K^* exponentially decreasing transverse mass spectra and the inverse slope parameters T in different centralities in Au+Au collisions and in p+p collisions, in order to calculate the K^* mean transverse momentum $\langle p_T \rangle$, we can use

$$\langle p_T \rangle = \int_0^\infty p_T \frac{1}{2\pi p_T} \frac{d^2N}{dy dp_T} p_T dp_T / \int_0^\infty \frac{1}{2\pi p_T} \frac{d^2N}{dy dp_T} p_T dp_T \tag{4.12}$$

Then

$$\langle p_T \rangle = \int_0^\infty p_T^2 e^{-(\sqrt{p_T^2+m_0^2}-m_0)/T} dp_T / \int_0^\infty p_T e^{-(\sqrt{p_T^2+m_0^2}-m_0)/T} dp_T \tag{4.13}$$

The $\langle p_T \rangle$ results for different centralities in Au+Au collisions and in p+p collisions calculated using Equation 4.13 are listed in Table 4.7 as values $\pm$ statistical uncer-

	$\langle p_T \rangle$ (GeV/c)
0-10%	1.080±0.025±0.117
10%-30%	1.117±0.056±0.121
30%-50%	1.080±0.046±0.117
50%-80%	1.031±0.037±0.112
p+p	0.679±0.028±0.028

Table 4.7: The K^* $\langle p_T \rangle$ in different centralities of Au+Au collisions and in p+p collisions.

tainties $\pm$ systematic uncertainties. The $\langle p_T \rangle$ in 0-10% centralities is from the top

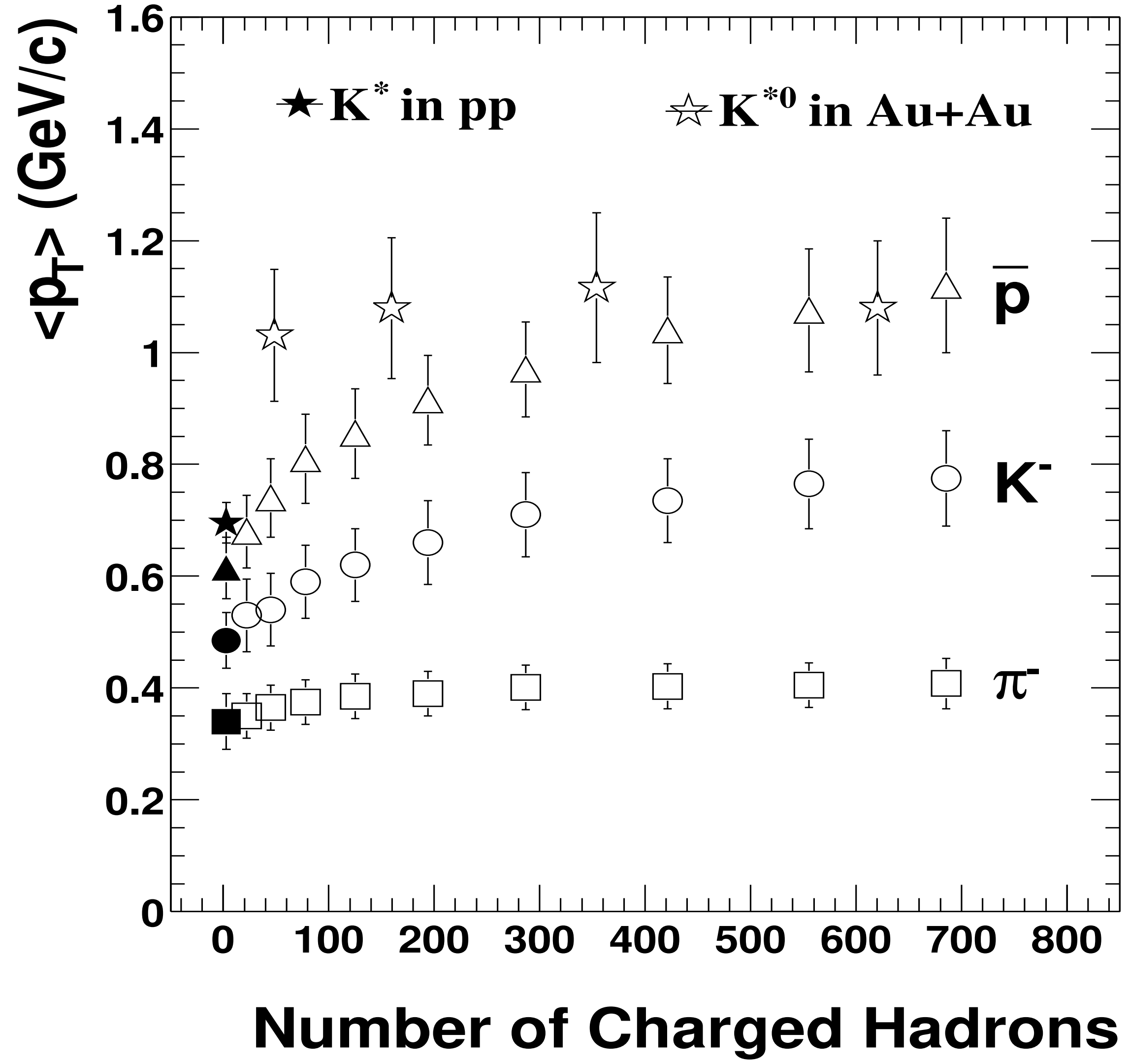

Figure 4.15: The K^* $\langle p_T \rangle$ as a function of number of charged hadrons compared to π^-, K^- and $\overline{p}$ in p+p (solid symbols) and Au+Au (open symbols) collisions.

10% central triggered Au+Au collisions. The $\langle p_T \rangle$ in p+p collisions calculated in this way is smaller than the $\langle p_T \rangle$ obtained from the power-law fit to the K^* transverse momentum spectrum.

Figure 4.15 shows the K^* $\langle p_T \rangle$ as a function of number of charged hadrons in different centralities in Au+Au collisions and in minimum bias p+p collisions. The data point for K^* $\langle p_T \rangle$ in p+p collisions is from the power-law fit to the K^* p_T spectrum. For comparison, the $\langle p_T \rangle$ for $\overline{p}$, K^- and π^- [64] are also shown in this figure.

From this figure, we observe a significant increase of the K^* $\langle p_T \rangle$ from p+p collisions to Au+Au collisions. This is consistent with our initial picture that high p_T resonances have a larger chance to be detected than low p_T resonances so that a larger $\langle p_T \rangle$ value is expected in Au+Au collisions.

4.6 Nuclear Modification Factor

The nuclear modification factor R_{AA} (Equation 1.5) or R_{CP} (Equation 1.6) of the $K^*(892)$ meson is important in differentiating between mass and particle species ordering. Current STAR measurements of identified hadrons, such K^0_S and Λ, show that the R_{CP} of Λ differs from that of K^0_S [77]. It is important to determine whether this difference is related to the particle masses or the type of particles (whether it is a meson or a baryon) since there is a significant mass difference between K^0_S and Λ. However, the K^* resonance is a meson with its mass close to the Λ baryon. Thus a measurement of the K^* nuclear modification factor, R_{AA} or R_{CP}, and the comparison to that of the K^0_S and Λ will give us information on this subject.

We have measured the K^{*0} invariant yields for seven p_T bins in top 10% central Au+Au collisions. We also measured the K^{*0} and $K^{*\pm}$ invariant yields as a function of p_T in minimum bias p+p collisions and fit these with a power-law function. Since the p_T spectra in both Au+Au and p+p collisions have the same rapidity and pseudorapidity ranges, we can just calculate the K^* R_{AA} by taking the ratio of the invariant yields in Au+Au collision to those in p+p collisions for each p_T bin, then scaling by $1/T_{AA}$. Although the p_T spectra in Au+Au and p+p don't have the same p_T bins, we can use the invariant yields calculated by the power-law fit function in p+p collisions

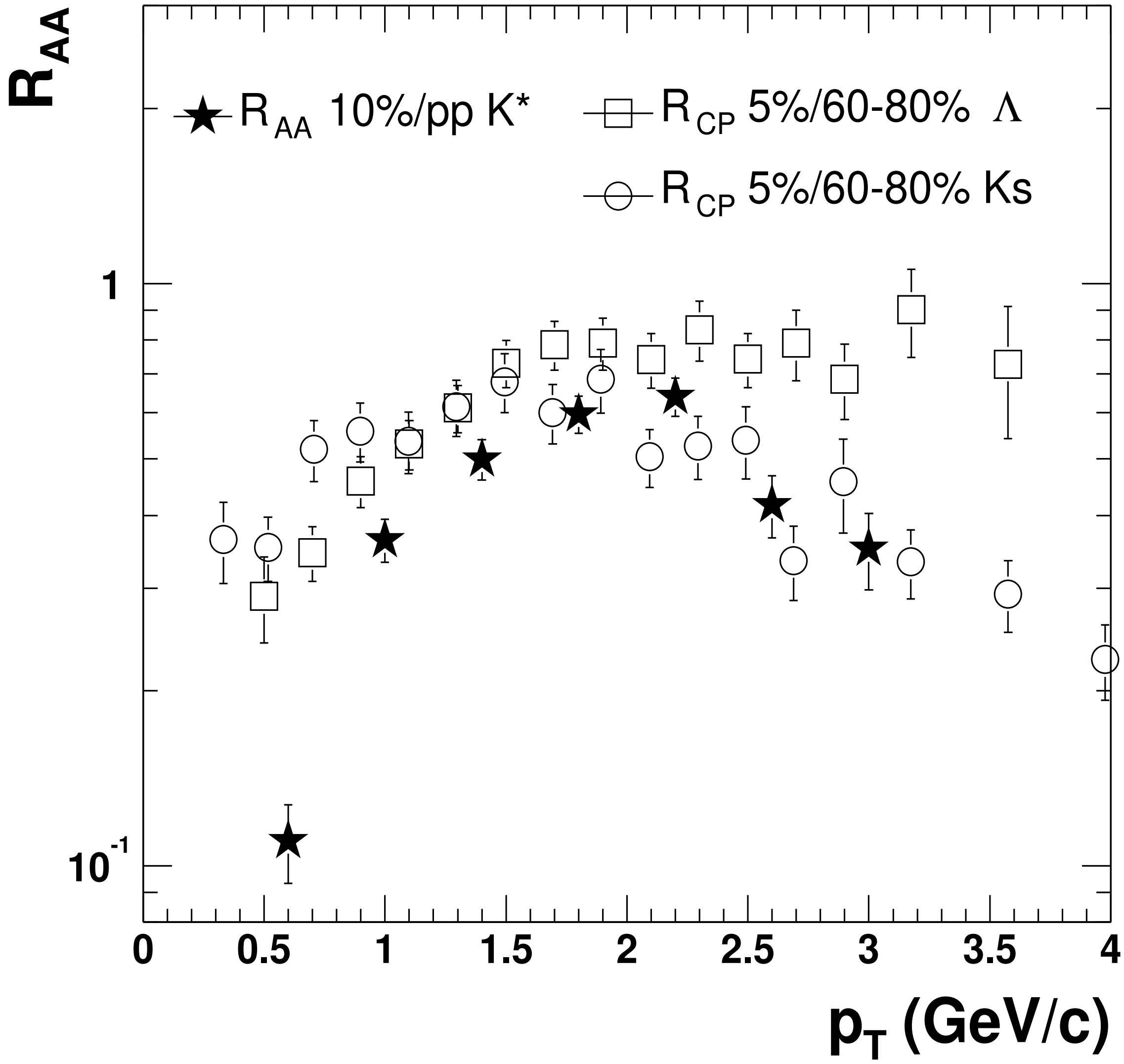

Figure 4.16: The K^* nuclear modification factor R_{AA} as a function of p_T compared to K_S^0 and Λ R_{CP}.

for the p_T value corresponding to each bin center in the Au+Au spectrum.
Figure 4.16 shows the K^* nuclear modification factor R_{AA} (top 10% central Au+Au / p+p) as a function of p_T along with R_{CP} (top 5% central Au+Au / 60%-80% peripheral Au+Au) of K^0_S and Λ. In this figure, we can see that the values of K^* R_{AA} at p_T <∼1.6 GeV/c are significantly smaller than the R_{CP} of both K^0_S and Λ. This is likely due to the loss of low p_T K^* signals in the hadron gas medium related to the daughter particles' re-scattering effect. At p_T >∼ 1.6GeV/c, the K^* R_{AA} values are close to the K^0_S R_{CP} and significantly different from the Λ R_{CP}. This gives us evidence that the nuclear modification factor R_{AA} or R_{CP} more likely depends on the particle types rather than the particle masses.

4.7 Elliptic Flow

In non-central Au+Au collisions, the hot-dense medium in both momentum space and coordinate space has an elliptic shape in the plane perpendicular to the beam axis. In the early stages after the collision, the ellipse in momentum space is perpendicular to that in coordinate space so that as the evolution of the fireball goes on, the ellipse in coordinate space will become more circular. If the evolution time is long enough, the ellipse in coordinate space might become elliptic again with the same orientation as the elliptic shape in momentum space [10].
Although measurements of the hadron elliptic flow v_2 in the STAR experiment [12] gave us information on the elliptic shape of the fireball in momentum space, it is difficult to determine the elliptic shape of the medium in coordinate space in the late stages. Fortunately, the K^* resonance provides a good signal which is sensitive to the medium shape in coordinate space due to the K^* daughter particles' re-scattering effect. If a K^* resonance decays inside the hadron medium, its kaon and pion daughter particles might be re-scattered by the particles inside the hadron gas. And this re-scattering effect depends on the shape of the medium in coordinate space. K^* resonances flying toward the long axis of the ellipse in coordinate space should have a larger re-scattering effect since there are more particles along the long axis than along the short axis of the elliptic shaped hadron medium. Thus a measurement of

K^* elliptic flow v_2 and its comparison to the hadron v_2 can give us information on the medium shape in coordinate space at the late stages. If there exists an elliptic shaped medium in coordinate space perpendicular to the ellipse in momentum space at the late stages of the collisions, we expect to observe a larger K^* v_2 than the hadron v_2. On the other hand, if the ellipse in coordinate space is identical to that in momentum space, we expect to observe a smaller K^* v_2.

Using the methods described in Section 3.9, we measured the K^{*0} elliptic flow v_2 as a function of p_T (shown in Figure 4.17) and as a function of collision centrality (shown in Figure 4.18) and compared to the charged hadron elliptic flow v_2. The data points shown in both figures have statistical uncertainties only. Results shown in Figure 4.17 are obtained from all minimum bias triggered Au+Au collisions. Results shown in Figure 4.17 are obtained from the entire K^{*0} p_T range from 0.4 to 3.2 GeV/c.

From the comparisons in both figures, due to limited statistics for the K^* analysis, we do not observe significant differences between the K^* v_2 and the charged hadron v_2 except in the most peripheral data point of K^{*0} v_2 in Figure 4.18. We expect to acquire more statistics in the RHIC IV run in 2004 which might give us $\sim$40M minimum bias triggered Au+Au collisions (an increase by a factor of 20) so that we can precisely measure the K^* elliptic flow v_2 to determine the medium shape in coordinate space.

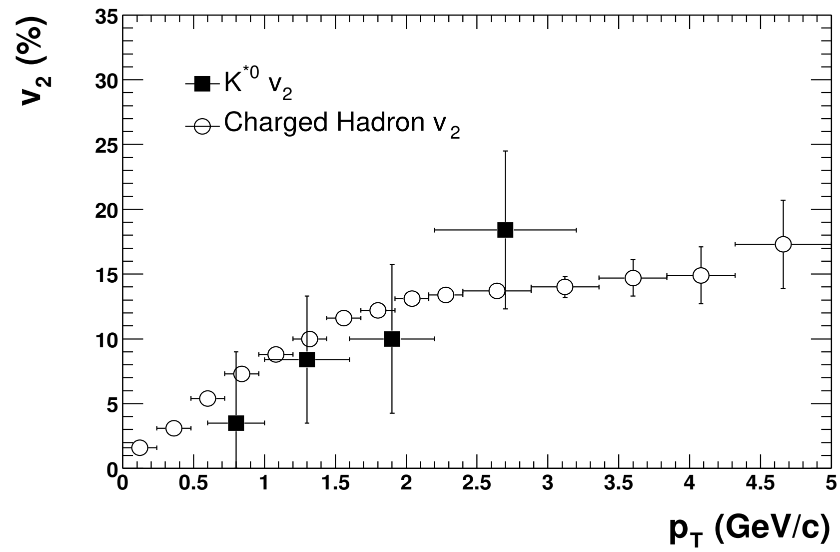

Figure 4.17: The K^{*0} elliptic flow v_2 as a function of p_T in minimum bias triggered Au+Au collisions compared to the charged hadron v_2.

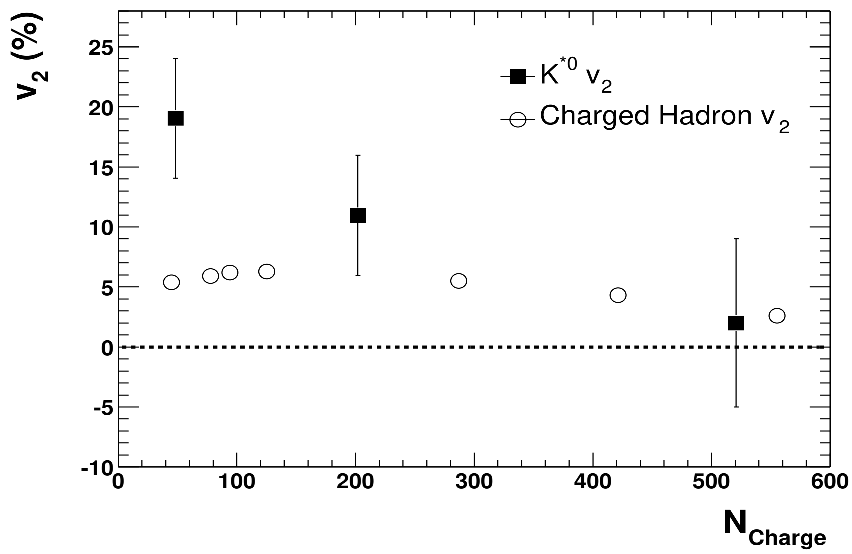

Figure 4.18: The K^{*0} elliptic flow v_2 as a function of collision centrality compared to the charged hadron v_2.

Chapter 5

Systematic Uncertainties

In this analysis, the available data for p+p collisions allow us to precisely measure the K^{*0} mass and width as a function of transverse momentum. Thus we are able to perform systematic uncertainty studies. We also measured the K^{*0} mass and width as a function of transverse momentum in top 10% central Au+Au collisions. Due to limited statistics, we are unable to perform studies of systematic uncertainties on the mass and width measurements. In the coming RHIC IV Au+Au run in 2004, we expect to have enough statistics to precisely measure the K^{*0} mass and width with systematic uncertainty studies.

STAR also measured the K^{*0} spectra in Au+Au collisions at $\sqrt{s_{NN}}$=130 GeV during the first RHIC run in 2000 [55]. With approximately 440,000 top 14% most central Au+Au collision events, the systematic uncertainty for the K^{*0} mid-rapidity yield dN/dy and the inverse slope parameter T were estimated to be 25% and 10%, respectively. In this analysis, we use about 2M top 10% central triggered Au+Au collision events and about 6M minimum bias triggered p+p collision events at $\sqrt{s_{NN}}$=200 GeV. The systematic uncertainties for the K^{*0} dN/dy and T have been significantly reduced and detailed studies are shown in this chapter.

5.1 Systematic Uncertainties for K^{*0} Mass in p+p Collisions

By Using Equation 3.9 to fit the $K\pi$ invariant mass spectrum after mixed-event background subtraction in p+p collisions, the K^{*0} natural mass and width parameters in p_T bins are extracted. A significant K^{*0} mass shift at low p_T is then observed, while no obvious K^{*0} width change is seen. In order to study the systematic uncertainties for K^{*0} mass in p+p collisions, we must consider the systematic effects from the particle types (K^{*0} vs. $\overline{K^{*0}}$), the mixed-event background subtraction methods, different functions representing the residual background, different sets of dynamical cuts, track types (primary tracks vs. global tracks), detector effects.

5.1.1 Particle Types

In this analysis, we measure the K^{*0} mass and width by adding K^{*0} and $\overline{K^{*0}}$ together in order to increase the statistics. We have to study the systematic uncertainties induced in doing this. Thus after we obtain $K^+\pi^-$ and $K^-\pi^+$ pair invariant mass spectra separately from same events and mixed events, we subtract the mixed-event background for K^{*0} and $\overline{K^{*0}}$ respectively as shown in Equation 5.1 and 5.2

$$N_{K^{*0}}(M) = N_{K_1^+\pi_1^-} - R_{K^{*0}} \times \sum_{i=2}^{6}(N_{K_1^+\pi_i^-} + N_{K_i^+\pi_1^-}) \tag{5.1}$$

$$N_{\overline{K^{*0}}}(M) = N_{K_1^-\pi_1^+} - R_{\overline{K^{*0}}} \times \sum_{i=2}^{6}(N_{K_1^-\pi_i^+} + N_{K_i^-\pi_1^+}) \tag{5.2}$$

Then we fit the background subtracted invariant mass spectra with the function in Equation 3.9 to extract the mass and width in each p_T bin for the K^{*0} and $\overline{K^{*0}}$, respectively. The differences in each p_T bin for extracted mass and width values between the $K^{*0} + \overline{K^{*0}}$ and the K^{*0} or $\overline{K^{*0}}$ are listed in Table 5.1 and Table 5.2, respectively.

5.1.2 Background Subtraction Methods

As described in Section 3.4.1, once the same-event and mixed-event $K\pi$ pair invariant mass spectra are obtained, the mixed-event background is subtracted as

$$N_{K^{*0}}(M) = N_s(M) - R \times N_m(M) \tag{5.3}$$

in which the subscripts s and m stand for the same-event spectrum and mixed-event spectrum, respectively, and R is the normalization factor. This background subtraction method is effective in reconstructing the K^{*0} signals for each p_T bin. Then we fit the background subtracted spectrum with Equation 5.4 to extract the K^{*0} mass and width values. Nevertheless, since the mixed-event background cannot perfectly represent the other $K\pi$ pairs in the same-event spectrum, we have to check the systematic uncertainties caused by this mixed-event background subtraction method.

$$f(M) = ag(M) + B(M) = ag(M) + bM + c \tag{5.4}$$

in which we define $g(M)$ as

$$g(M) = \frac{1}{a}F(M) \times P(M) = \frac{M\Gamma M_0}{(M^2 - M_0^2)^2 + M_0^2\Gamma^2} \times \frac{M}{\sqrt{M^2 + p_T^2}} e^{-\frac{\sqrt{M^2+p_T^2}}{T}} \tag{5.5}$$

In this analysis, we use two methods to study the systematic uncertainties induced by the mixed-event background subtraction method.
In method (1), we obtain an invariant mass distribution $n(M)$ by

$$n(M) = N_s(M)/N_m(M) \tag{5.6}$$

Then we fit the invariant mass distribution $n(M)$ with Equation 5.7 to extract the K^{*0} natural mass in each p_T bin.

$$f_1(M) = a[1 + bg(M)] \tag{5.7}$$

In method (2), we fit the same-event spectrum $N_s(M)$ with Equation 5.8 to extract the K^{*0} natural mass and in each p_T bin.

$$f_2(M) = ag(M) + bM^2 + cM + d \tag{5.8}$$

The differences in p_T bins for extracted mass and width values between the mixed-event background subtraction method and method (1) or method (2) are listed in Table 5.1 and Table 5.2, respectively. By using method (1) and method (2), K^{*0} signals in some p_T bins may not be reconstructed effectively. In these cases, the differences in corresponding p_T bins are listed as "N/A" in Table 5.1 and Table 5.2.

5.1.3 Residual Background Functions

By using the event-mixing technique, since the mixed-event invariant mass spectrum cannot perfectly describe the other $K\pi$ pairs in the same-event spectrum, there is always a certain amount of residual background in the mixed-event background subtracted invariant mass spectrum. In this analysis, we use a linear function as shown in Equation 3.8 to represent the residual background. In order to study the systematic uncertainties induced by this linear residual background function, we use both a second order polynomial function and an exponential function to represent the residual background as shown in Equations 5.9 and 5.10, respectively

$$B_1(M) = bM^2 + cM + d \tag{5.9}$$

$$B_2(M) = b \times e^{-c(M-d)} \tag{5.10}$$

The differences in p_T bins between the linear function method and the second polynomial function method or the exponential function method for extracted mass and width values are listed in Table 5.1 and Table 5.2, respectively.

5.1.4 Dynamical Cuts Effect

The systematic uncertainties on K^{*0} mass induced by various dynamical cuts, such as the tracks' number of fit points cut, the ratio of number of fit points to number of possible points cut, the track pseudo-rapidity cut, the track measured DCA cut, the dE/dx cut, etc, are at the level of 0.1 MeV/c^2. The largest amount of systematic uncertainties induced by the dynamical cuts comes from the kaon and pion momentum cuts.

As discussed in Section 3.3, in this analysis, we select kaon candidates' momentum and transverse momentum in the range $0.2 < p(\text{and } p_T) < 0.7$ GeV/c and pion candidates' momentum and transverse momentum in the range $0.2 < p(\text{and } p_T) < 10.0$ GeV/c in order to reduce the amount of residual background and thus precisely measure the K^{*0} mass and width values as a function of p_T in p+p collisions. We use two different sets of track momentum cuts to check the systematic uncertainties due to this reason: (1) kaon candidates: $0.2 < p(\text{and } p_T) < 10.0$ GeV/c and pion candidates: $0.2 < p(\text{and } p_T) < 10.0$ GeV/c; (2) kaon candidates: $0.2 < p(\text{and } p_T) < 0.7$ GeV/c and pion candidates: $0.2 < p(\text{and } p_T) < 0.7$ GeV/c. By using the cut set (1), we will have a larger amount of residual background. And by using the cut set (2), we will lose some of the statistics. The K^{*0} signals with $p_T > 0.8$ GeV/c cannot be effectively reconstructed in both cases so that we can only study the systematic uncertainties for K^{*0} mass and width values with $p_T < 0.8$ GeV/c. Results are listed in Table 5.1 and Table 5.2.

5.1.5 Track Types

In the event reconstruction stage, we force a global track with DCA<3.0 cm to pass through the collision vertex and re-fit this track to get a primary track. Thus the momentum is slightly different between a primary track and its associated global track. In this analysis, we use primary tracks as kaon and pion candidate tracks and use global tracks to check the systematic uncertainties on K^{*0} mass and width values induced in using primary track momentum only. The differences in p_T bins for extracted mass and width values between using the primary track momentum and using the global track momentum are listed in Table 5.1 and Table 5.2, respectively.

5.1.6 Detector Effects

Once a collision event happens and charged tracks go through the STAR TPC detector, the gas in the TPC will be ionized and the TPC will be full of charged ions. If the charged ions cannot completely disappear before next collision event happens, these charges would be deposited inside the TPC by each collision event. These deposited charges in the TPC are called space charges. The space charges will change the electric field inside the TPC and thus affect the measurement of track momentum. Studies [78] have shown that this space charge effect will change the magnitude of the momentum of the positive/negative charged tracks by plus/minus 2% per GeV/c. The space charge effect will also change the opening angle of each oppositely charged pair by 4 mrad.

According to independent studies using the RICH detector [79], the charged tracks' transverse momentum measured by the TPC should be corrected by

$$\Delta p_T = 0.007 \times p_T^2 \tag{5.11}$$

All the above detector effects will affect the observed K^{*0} natural mass and width values, since we use charged track momentum measured by the TPC detector to reconstruct the K^{*0} signals. Using Monte Carlo simulations, we find that these space charge effects will change the K^{*0} mass by about ± 3.0 MeV/c^2 and change the K^{*0} width by ± 2.0 MeV/c^2 in each p_T bin.

In a summary, the systematic uncertainties in p_T bins in minimum bias triggered p+p collisions for K^{*0} mass and width values are listed in Table 5.1 and Table 5.2, respectively. The total systematic uncertainties are calculated as shown in Equation 5.12 and 5.13 for each p_T bin

$$\Delta M(p_T) = \sqrt{\sum_i \Delta M_i(p_T)} \tag{5.12}$$

$$\Delta \Gamma(p_T) = \sqrt{\sum_i \Delta \Gamma_i(p_T)} \tag{5.13}$$

p_T (GeV/c)	0.0-0.2	0.2-0.4	0.4-0.6	0.6-0.8	0.8-1.0	1.0-1.2	1.2-1.4	1.4-1.6
K^{*0} only	-2.6	-1.7	+1.2	-1.7	+0.7	-1.4	+0.4	+0.1
$\overline{K^{*0}}$ only	+3.1	+1.7	-1.5	+1.9	-0.7	+3.2	+0.3	+0.1
Method (1)	N/A	N/A	-3.7	-0.5	-0.1	-1.8	-2.6	-2.2
Method (2)	-2.4	-0.2	-0.5	-0.8	-1.0	N/A	N/A	N/A
Backgrnd 6.9	+0.2	+0.1	-0.2	-0.1	+0.2	+0.1	-0.2	-0.2
Backgrnd 6.10	-0.1	+0.1	+0.1	+0.2	-0.1	-0.1	+0.1	+0.2
Cut Set (1)	+0.2	-0.2	-0.1	+2.4	N/A	N/A	N/A	N/A
Cut Set (2)	+0.9	+1.2	-1.3	-3.4	N/A	N/A	N/A	N/A
Global Track	-2.7	-4.6	-3.5	-2.7	-1.0	-1.4	+2.6	+0.2
Detector Eff	$\sim \pm 3.0$							
Total Sys Err	±5.4	±5.8	±6.2	±5.6	±3.4	±4.4	±4.0	±3.7

Table 5.1: Systematic uncertainties in p_T bins for the K^{*0} natural mass in minimum bias triggered p+p collisions. Units for extracted mass differences are MeV/c^2.

p_T (GeV/c)	0.0-0.2	0.2-0.4	0.4-0.6	0.6-0.8	0.8-1.0	1.0-1.2	1.2-1.4	1.4-1.6
K^{*0} only	+7	-2	+2	-2	+9	+5	+10	+1
$\overline{K^{*0}}$ only	-11	+2	-3	+3	-9	+5	-7	+1
Method (1)	N/A	N/A	-3	+5	-5	+2	+12	+7
Method (2)	-22	-6	+5	+4	-3	N/A	N/A	N/A
Backgrnd 6.9	+2	-1	+2	-1	-1	+2	-2	+2
Backgrnd 6.10	-1	+1	-2	-2	+2	-1	+2	+1
Cut Set (1)	+2	-2	-1	+2	N/A	N/A	N/A	N/A
Cut Set (2)	+1	+2	-3	-4	N/A	N/A	N/A	N/A
Global Track	+2	-2	+5	+7	-2	-2	+9	+8
Detector Eff	$\sim \pm 2.0$							
Total Sys Err	±25	±7	±8	±10	±11	±8	±19	±11

Table 5.2: Systematic uncertainties in p_T bins for the K^{*0} width in minimum bias triggered p+p collisions. Units for extracted width differences are MeV/c^2.

5.2 Systematic Uncertainties for Yield and Inverse Slope

In order to study the systematic uncertainties on the K^{*0} mid-rapidity yield dN/dy and the inverse slope parameter T, we need to consider the systematic effects from the fit functions for the K^{*0} signal, residual background functions, particle types, all kinds of dynamical cut effects and detector effects. We use the top 10% central triggered Au+Au collision events to study the systematic uncertainties for different centralities in Au+Au collisions.

5.2.1 Fit Functions

To extract the yield of the K^* in a certain transverse momentum range, we use a simplified Breit-Wigner function shown in Equation 3.10 for the K^* signal and fix the natural mass and width parameters as the values obtained from Section 3.10. Thus we have to study the systematic effects on the K^* yields induced in doing this way. Our studies show that by using Equation 3.9 with open natural mass and width parameters in the fit function, the K^{*0} yield is changed by -2.49% and -0.63% in top 10% central triggered Au+Au collisions and minimum bias triggered p+p collisions, respectively.

5.2.2 Residual Background Functions

In this analysis, we use a linear function as shown in Equation 3.8 to represent the residual background in the mixed-event background subtracted invariant mass spectrum. Thus in order to study the systematic effects on the K^{*0} yields induced by this linear background method, we use both a second order polynomial function (Equation 5.9) and an exponential function (Equation 5.10) to represent the residual background.

Our studies show that using the second order polynomial function to represent the residual background changes the K^{*0} yield by -8.30% and +3.43% in top 10% central Au+Au collisions and p+p collisions, respectively. Using the exponential function to represent the residual background changes the K^{*0} yield by +12.05% and +2.05% in top 10% central Au+Au and p+p collisions, respectively.

5.2.3 Particle Types

When calculating the K^{*0} mid-rapidity yield dN/dy and the inverse slope parameter T, we add the K^{*0} and $\overline{K^{*0}}$ together to increase the statistics. Thus we study the systematic uncertainties of this by reconstructing the K^{*0} and $\overline{K^{*0}}$ separately. Results on the systematic uncertainties induced by different particle types are listed in Table 5.3.

5.2.4 Dynamical Cut Effects

The systematic uncertainties in the K^{*0} mid-rapidity yield, dN/dy, and inverse slope parameter induced by various dynamical cuts mostly come from the tracks' number of fit points cut. Thus we cut on the tracks' number of fit points greater than 20 to study the systematic uncertainties. Results are listed in Table 5.3.

5.2.5 Detector Effects

The Au+Au and p+p collision data used in this analysis were taken with a magnetic field of +0.5 Tesla (defined as full field) and -0.5 Tesla (defined as reversed full field) inside the TPC separately. Different magnetic fields result in different systematic effects in the measurement of K^{*0} dN/dy and T. Thus by analyzing data taken with full field and reversed full field, systematic uncertainties on the K^{*0} dN/dy and T are listed in Table 5.3.

The STAR TPC detector consists of two identical parts located at the east side and west side along the beam direction and separated by a center foil. The charged tracks measured by the east/west side of the TPC are defined to have negative/positive pseudo-rapidity η values. By reconstructing K^{*0} signal by using tracks with negative/positive pseudo-rapidity, we have results on the systematic uncertainties for the K^{*0} dN/dy and T due to this east-west side difference of the TPC detector which are listed in Table 5.3.

In order to achieve roughly uniform acceptance over the pseudo-rapidity range, we require the collision vertex in both Au+Au and p+p collision events to be within $\pm$ 50 cm along the beam direction. Then we select events with |VertZ| $<$ 25 cm in top 10% central triggered Au+Au collisions and |VertZ| $<$ 75 cm in minimum bias triggered p+p collisions, respectively, to study the systematic uncertainties induced by this collision vertex cut. Results are listed in Table 5.3.

In a summary, the systematic uncertaities on the K^{*0} mid-rapidity yield dN/dy and the inverse slope parameter T in Au+Au and p+p collisions are listed in Table 5.3 as percentages.

	dN/dy in p+p	T in p+p	dN/dy in Au+Au	T in Au+Au
Fit Functions	-0.63%	0	-2.49%	0
Backgrnd 6.9	+3.43%	0	-8.30%	0
Backgrnd 6.10	+2.05%	0	+12.05%	0
K^{*0} only	+5.46%	-2.04%	+1.77%	-1.10%
$\overline{K^{*0}}$ only	-5.17%	+1.59%	-1.12%	+2.81%
Full Field	-1.74%	-3.45%	+1.73%	+0.87%
Rev. Full Field	+0.77%	+1.00%	-1.40%	+1.33%
West TPC	-0.53%	-0.68%	-0.86%	+1.99%
East TPC	-0.34%	-0.45%	+8.97%	+0.07%
NFitPnts Cut	-0.15%	+0.50%	+4.38%	+0.12%
VertZ Cut	+0.22%	+0.77%	-0.90%	+2.20%
Total Sys Err	±6.5%	±4.09%	±15.53%	±10.86%

Table 5.3: Systematic uncertainties in percentages for the mid-rapidity yield dN/dy and the inverse slope parameter T in minimum bias triggered p+p collisions and top 10% central triggered Au+Au collisions.

Chapter 6

Discussion

6.1 In-Medium Effects and Mass Modification

In Figure 6.1, a downward K^{*0} mass shift up to $\sim$10 MeV/c^2 is observed in both p+p and top 10% central Au+Au collisions and this downward mass shift is p_T dependent. In the STAR experiment, we have also observed a downward ρ^0 mass shift

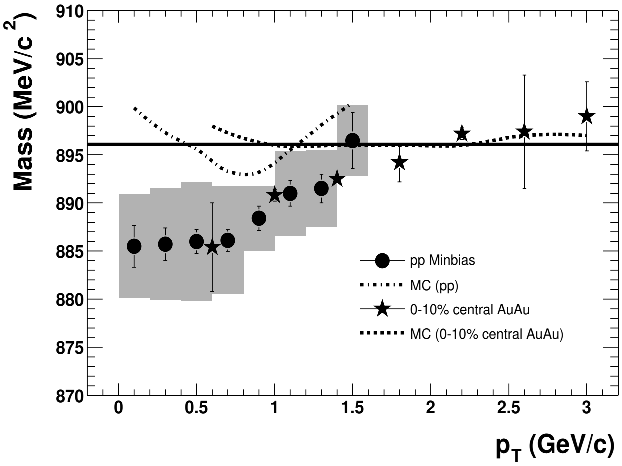

Figure 6.1: K^{*0} mass as a function of transverse momentum in p+p and top 10% central Au+Au collisions. The solid straight line stands for the standard K^{*0} mass (896.1 MeV/c^2). The dot-dashed (dashed) curve represents the MC results for K^{*0} mass in p+p (top 10% central Au+Au) collisions after considering detector effects and kinematic cuts. The grey shadows represent systematic uncertainties in p+p.

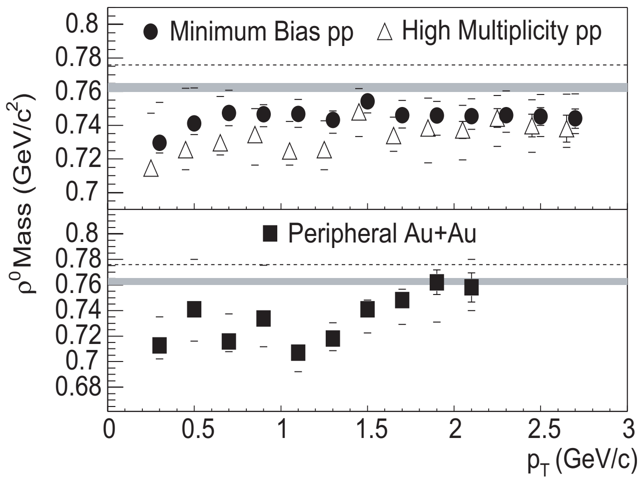

Figure 6.2: The ρ^0 mass as a function of p_T for minimum bias p+p (filled circles), high multiplicity p+p (open triangles), and peripheral Au+Au (filled squares) collisions. The dashed lines represent the average of the ρ^0 mass measured in e^+e^-. The shaded areas indicate the ρ^0 mass measured in p+p collisions. Figure is taken from [66].

up to ~50 MeV/c^2 in both minimum bias triggered p+p collisions and peripheral Au+Au collisions shown in Figure 6.2 [66]. The p_T dependence of the ρ^0 mass has similar behavior to the K^{*0} mass. The Δ^{++} mass as function of number of charged hadrons in Au+Au and p+p collisions has also be measured and a downward mass shift up to ~20 MeV/c^2 has been observed [67]. No significant change of the K^{*0}, ρ^0 or Δ^{++} width has been observed.

All the above measurements for K^{*0}, ρ^0 and Δ^{++} mass shifts suggest that the properties of the resonances in the hot-dense medium have been modified by an in-medium effect. The K^{*0} lifetime is 4 fm/c, the ρ^0 lifetime is about 1.2 fm/c and the Δ^{++} lifetime is about 1.5 fm/c. All these three resonance species may decay inside the hadron medium before the accumulated in-medium effects might be released. Thus the reconstructed K^{*0}, ρ^0 and Δ^{++} can give us information on their properties inside the medium with high temperature and high densities. The K^{*0} natural width is 50.7 MeV/c^2, the ρ^0 natural width is 150 MeV/c^2 and the Δ^{++} natural width is about 120 MeV/c^2. Thus these resonances themselves provide relatively large space for the in-medium effect to modify their masses.

In the case of the ϕ and $\Lambda^*(1520)$ resonances, their lifetimes are about 40 fm/c for

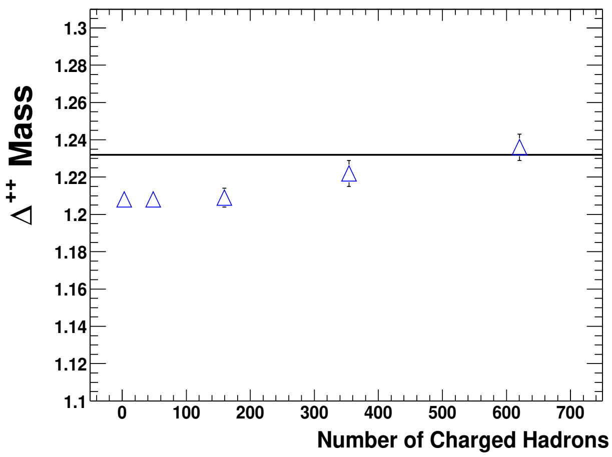

Figure 6.3: The Δ^{++} mass as a function of number of charged hadrons in p+p (first symbol from left) and Au+Au (four right symbols) collisions. Figure is taken from [67].

ϕ and 13 fm/c for $\Lambda^*(1520)$. They may also undergo an in-medium effect and their properties might be changed when they are inside the hadronic medium. However, their relatively larger lifetimes, compared to the K^{*0}, ρ^0 and Δ^{++} resonances, might allow them to decay after the kinetic freeze-out when all the in-medium effects have disappeared. From the measurements in the STAR experiment, we do not observe a significant mass shift for the ϕ meson [65] and the mass shift ($<$ 3 MeV/c^2) for the $\Lambda^*(1520)$ [23] is also negligible considering the relatively large statistical uncertainties in Au+Au and p+p collisions.

Resonances with large p_T may have more chances to escape the medium earlier than the kinetic freeze-out stage and thus when they decay outside the fireball, their accumulated in-medium effect might have disappeared. Thus the high p_T resonances properties might be less likely to be modified by the in-medium effect. This may explain the observed K^{*0} and ρ^0 mass p_T dependence.

6.2 Re-Scattering and Re-Generation Effects and Evolution Properties

From Figure 6.4, we can see that the K^*/K ratios in Au+Au collisions are significantly smaller than the ratio in p+p collisions. This suppression in Au+Au collisions is expected from the K^* daughter particles' re-scattering effect in the hadron medium which destroys part of the primordial K^* yield. As discussed in Section 1.2.5, the UrQMD transport model calculations [28] also predict that the high p_T K^* resonances are more likely to be reconstructed than the low p_T K^*. Thus larger inverse slope parameters in Au+Au collisions are also expected. Our measurements of the K^{*0} transverse mass spectra and the inverse slope parameters in Au+Au and p+p collisions have confirmed this UrQMD model prediction. As shown in Table 4.4, the inverse slope parameters measured in Au+Au collisions are significantly larger than that in p+p collisions. Figure 4.14 shows that the K^* $\langle p_T \rangle$ in Au+Au collisions are significantly larger than that in p+p collisions which also demonstrates the same UrQMD prediction.

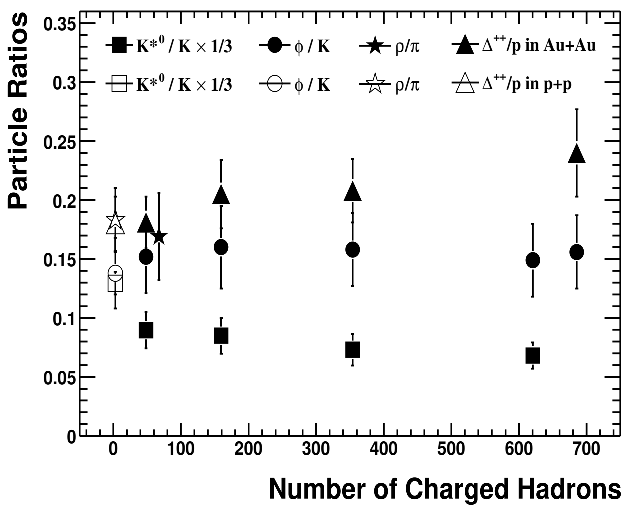

Figure 6.4: The K^{*0}/K, ϕ/K, ρ/π and Δ/p ratios as a function of number of charged hadrons in p+p (open symbols) and Au+Au (solid symbols) collisions.

Different resonances decay into different hadronic daughters and different hadronic daughters may have different interaction cross sections with the pions which are the predominant hadrons in the medium. Thus the relative yields of the resonances destroyed by the daughter particles' re-scattering effect should be different for different resonances. On the other hand, the amount of resonance signals re-produced by the re-generation effect in the hadron medium should also be different due to the same reason. Considering the above discussions, the differences between the observed resonances yields and their corresponding primordial yields might be different for different resonances, such as K^{*0}, ρ^0, ϕ, Δ^{++}, etc.

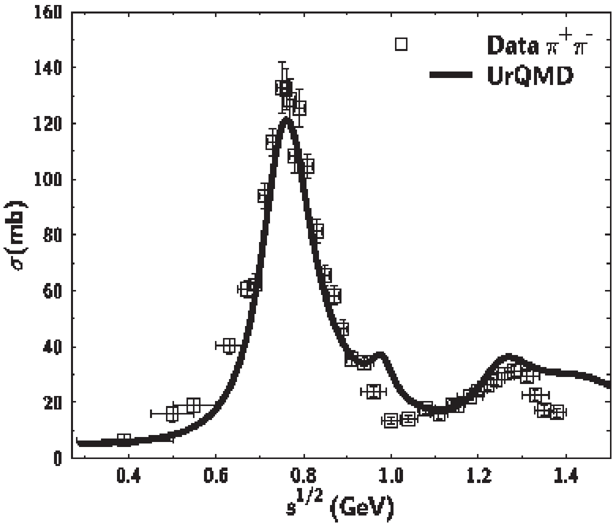

Figure 6.5: The total cross section of $\pi^+\pi^-$ scattering as a function of c.m. energy $\sqrt{s}$. Figure is taken from [37].

Figure 6.5 shows the $\pi^+\pi^-$ interaction cross sections as a function of collision energy and Figure 6.6 shows the π^-K^+ interaction cross sections from UrQMD calculations [37]. From these two figures, we can see that the total cross section for pion-pion interactions is about a factor of 5 larger than the total cross section for pion-kaon interactions. The K^{*0} decays to a kaon and a pion. As long as at least one of its daughters is re-scattered by the hadrons in the medium, we will lose this K^{*0} signal. Thus the re-scattering effect should be mostly determined by the pion-pion

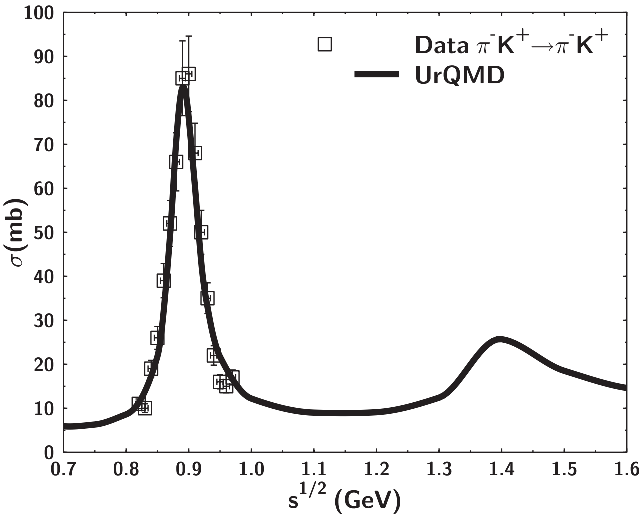

Figure 6.6: The total cross section of $\pi^- K^+$ scattering as a function of c.m. energy $\sqrt{s}$. Figure is taken from [37].

interaction section since the dominant species inside the medium is pions and the kaon-pion re-scattering is negligible compared to the pion-pion interactions. On the other hand, the cross section for kaon-pion interaction to re-produce the K^{*0} signals is relatively small so that the re-generation cannot compensate the loss of the K^{*0} signals due to the daughter particles' re-scattering effect. Thus we observe a K^*/K suppression in Au+Au collision compared to p+p collisions.

In the case of $\rho^0 \to \pi^+\pi^-$, the cross section for the daughter pions re-scattered by the medium pions is the same as the cross section for two medium pions scatter with each other to produce the ρ^0 signals. Thus we do not expect to observe any significant ρ^0/π ratio difference between Au+Au and p+p collisions. In Figure 6.4, the ρ/π ratios in p+p and Au+Au demonstrate our prediction.

In the case of the ϕ resonance, it has a relatively larger lifetime (~40 fm/c) compared to K^{*0}, ρ and Δ^{++}. It has much larger chances to decay after the kinetic freeze-out and thus avoid the re-scattering effect. The cross section for K^+K^- interaction to re-create ϕs is also relatively smaller. Thus in the case of the ϕ resonance, both the re-scattering and the re-generation effects are weak so that the ϕ/K ratio in Au+Au collisions is not expected to be much different from the ratio in p+p collisions.

Figure 6.7 shows the π^+p interaction cross sections as a function of collision energy. The total cross section for proton-pion interactions is about 1.3 times of the total cross section for pion-pion interactions. Thus we would expect to see that the Δ^{++} signals re-produced by the re-generation effect might exceed the signals destroyed by the re-scattering effect. In Figure 6.4, we can see that the Δ^{++}/p ratios in Au+Au collisions are slightly larger than the ratio in p+p collisions. Considering the data uncertainties, no significant suppression for the Δ^{++}/p ratio suppression in Au+Au can be observed compared to the ratio in p+p collisions.

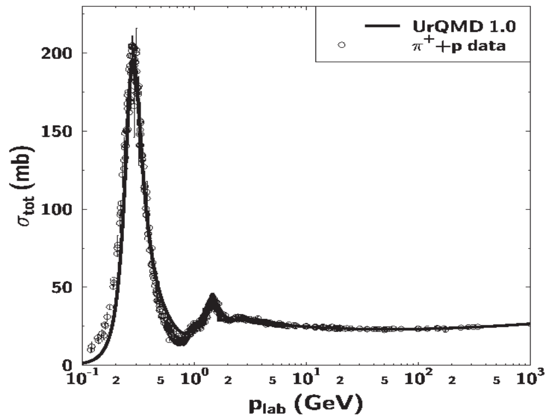

Figure 6.7: The total cross section of π^+p scattering as a function of laboratory momentum p_{lab}. Figure is taken from [37].

6.3 Time Scale Estimation between Freeze-Outs

In Figure 4.12 and 4.13, we can see that the K^*/K ratios in Au+Au collisions are significantly smaller than the ratio in p+p collisions. Statistical model calculations [80] also predict that the K^*/K ratio in central Au+Au collisions is about 0.37 which is also significantly larger than the ratios we have measured in Au+Au collisions. This is due to the fact that the K^* decay daughter particles' re-scattering effect in the hadron gas medium destroys a portion of the K^* signals in Au+Au collisions. Thus we can use the K^*/K ratio difference between Au+Au collisions and p+p collisions (or the statistical model predictions in Au+Au) to estimate the time between the chemical freeze-out stage and the kinetic freeze-out stage.

First, we define t_C as the time at the chemical freeze-out stage when the abundances of the mesons and baryons emerging from a pre-hadronic state are expected to be fixed by hadronization temperature and chemical fugacities. We also define t_K as the time at the kinetic freeze-out stage when all hadrons stop interacting. Thus in order to calculate the time $\Delta t = t_K - t_C$, we have make the following assumptions: (1) we assume that all the thermally produced K^* signals appear at the chemical freeze-out stage t_C; (2) we lose all the K^* signals which decay inside the hadron gas medium due to the daughter particles' re-scattering effect; (3) we ignore the re-generation effect. Thus the time difference between the chemical freeze-out and the kinetic freeze-out can be calculated as

$$\frac{K^*}{K}|_{t_K} = \frac{K^*}{K}|_{t_C} e^{-\Delta t/\tau} \tag{6.1}$$

In the above equation, τ is the K^* lifetime which is 4 fm/c. We use the measured K^*/K ratio in the top 10% central Au+Au collisions which is 0.2046 ± 0.0333 as the ratio at t_K and use the measured K^*/K ratio in p+p collisions which is 0.3889 ± 0.0286 as the ratio at t_C. Thus we can get the time between the chemical freeze-out and the kinetic freeze-out $\Delta t = 3 \pm 1$ fm/c.

Now let's go back to check our assumptions. Not all the thermally produced K^* signals can appear exactly at t_C. Part of them may appear even earlier. This fact may imply a smaller Δt value for the time scale between the chemical and kinetic freeze-outs. But the time allowed for the K^* thermal production before the chemical freeze-out might be very short [28]. Thus the necessary correction to the calculated Δt value is expected to be small. Second, we cannot guarantee that all the K^* signals decay inside the fireball will be destroyed. Some high p_T K^* resonances may escape the fireball and decay before the kinetic freeze-out stage. In this case, we still can detect these high p_T K^* signals. This effect imply a larger Δt for the time difference between the chemical and kinetic freeze-outs. Third, the kaon and pion particles inside the hadron gas medium may interact with each other to re-produce part of the K^* signals due to the re-generation effect. This would make the time Δt larger than calculated. Due to the discussions above, our value of Δt should be considered as a rough estimation and probably a lower limit on the time between the chemical and kinetic freeze-outs.

On the other hand, due to the relatively large interaction cross sections between the K^* decay pion daughter and the pion particles in the hadron gas medium, very few K^* signals which decay inside the medium can be detected. Second, the total amount of high p_T K^* resonance which can escape the fireball should be much smaller than the amount of the low p_T K^* resonances which mainly determine the total K^* total yield (due to the exponentially decreasing behavior in the K^* transverse mass spectra in Au+Au collisions). Third, the interaction cross sections between the medium kaon and pion particles are about a factor of 5 smaller than the pion-pion interaction cross sections. Thus the re-generation effect cannot compensate much of the lost K^* resonance due to the daughter particles' re-scattering effect. From these discussions, we can qualitatively conclude that the real time difference between the two freeze-outs is not expected to be much larger than our calculated Δt.

As discussed in Section 1.2.5, the UrQMD transport model [28] considers the flavor and chemistry changing processes predominantly before the chemical freeze-out stage and the elastic and pseudo-elastic processes between the chemical and kinetic freeze-outs. In Figure 1.1, we can see that at $t \sim 6$ fm/c, the elastic processes exceed the flavor and chemistry changing inelastic processes so that the system reaches the chemical freeze-out point. At $t \sim 11$ fm/c, the elastic interaction rate starts to exponentially decrease so that the system reaches the kinetic freeze-out stage. Thus from the UrQMD calculations, we can see that the time scale between the chemical and kinetic freeze-outs is about 5 fm/c in Pb+Pb at 160A GeV which is consistent with our measurement that the time scale is not much larger than 3 ± 1 fm/c.

G. Torrieri and J. Rafelski [33] have theoretically studied the strange hadron resonances as a signature of freeze-out dynamics. They started with the thermally produced resonances at the chemical stage and then considered the re-scattering effect for the resonance decay products in the hadron fireball. Finally they performed a quantitative analysis on how the suppression of the observability of the resonances can

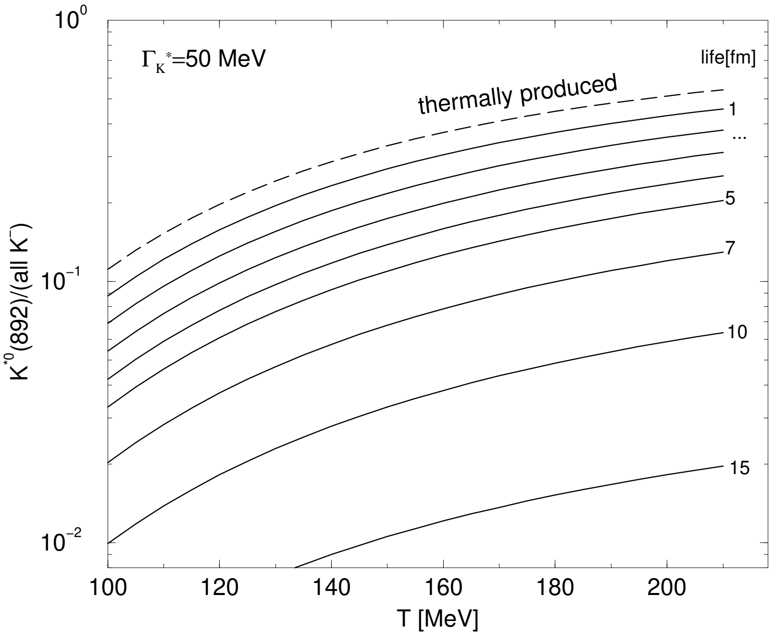

Figure 6.8: Thermally produced (dashed line) and observable (solid lines) of K^{*0}/K ratio vs. the chemical freeze-out temperature T. The solid lines correspond to evolution after chemical freeze-out of 1,2,3,4,5,7,10,15,20 fm/c, respectively. Figure is taken from [33].

constrain both the chemical freeze-out temperature and the lifetime of the hadron interaction phase evolving between the chemical and the kinetic freeze-out conditions. Figure 6.8 shows the thermally produced (dashed line) and the observable (solid lines) K^{*0}/K ratio as a function of the chemical freeze-out temperature T for different time intervals between the chemical and kinetic freeze-outs. For Au+Au collisions at $\sqrt{s_{NN}}$, we reasonably select the temperature at chemical freeze-out to be $T = 160$ MeV [6, 80]. Thus according to our measured K^*/K ratio at the top 10% central Au+Au collisions, we can read from the figure that the time scale between two freeze-outs is between 4 and 6 fm/c which is also consistent with our calculations.

G. Torrieri and J. Rafelski [33] also used the combined K^{*0}/K and $\Lambda(1520)/\Lambda$ ratios to constrain both the chemical freeze-out temperature and the interacting phase lifetime as shown in Figure 6.9. Since at RHIC, the $\Lambda(1520)$ resonance can also be reconstructed [23], we expect to soon be able to use both the K^*/K and $\Lambda(1520)/\Lambda$

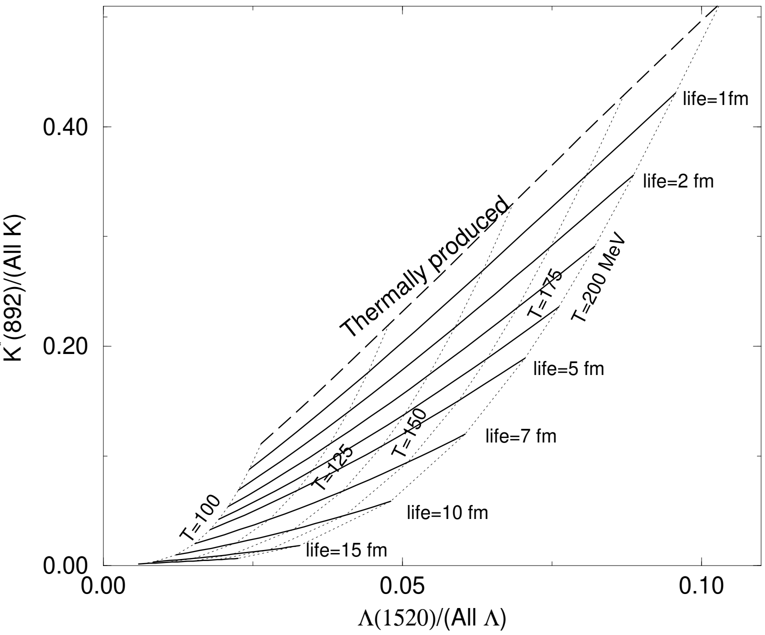

Figure 6.9: Dependence of the combined K^{*0}/K and $\Lambda(1520)/\Lambda$ ratios on the chemical freeze-out temperature and interacting phase lifetime. Figure is taken from [33].

ratios to determine the chemical freeze-out temperature and the time scale between freeze-outs at the same time according to G. Torrieri and J. Rafelski's calculations.

In conclusion, through the measurement of the K^*/K ratios in both Au+Au and p+p collisions, we estimate that the time scale between the chemical and kinetic freeze-outs is not much larger than 3 ± 1 fm/c. And this result is consistent with the UrQMD transport model calculations for the Pb+Pb at 160 A GeV and the theoretical calculations by G. Torrieri and J. Rafelski. We also expect to use soon both the K^*/K and $\Lambda(1520)/\Lambda$ ratios to determine the chemical freeze-out temperature and the time scale between freeze-outs at the same time. As discussed in Section 1.2.4, we might also be able to measure the ρ di-leptonic decay to constrain the upper limit for the time scale between the freeze-outs.

Chapter 7

Conclusion

By using about 2M top 10% central triggered and 2M minimum bias triggered Au+Au collision events and 6M minimum bias triggered p+p collision events at $\sqrt{s_{NN}}$=200 GeV taken during the second RHIC run in 2001 and 2002, the K^{*0} and $K^{*\pm}$ vector meson resonance production has been measured via their hadronic decay channels: $K^{*0} \rightarrow K\pi$ and $K^{*\pm} \rightarrow K^0_S\pi^{\pm}$.

The K^{*0} mass and width as a function of p_T have been measured in central Au+Au and p+p collisions. The K^{*0} transverse mass spectra have been studied in central Au+Au, four centrality bins in minimum bias Au+Au and p+p collisions and the K^{*0} mid-rapidity yield, dN/dy, and the inverse slope parameter, T, have been extracted through an exponential fit to the transverse mass spectra. The K^{*0} and $K^{*\pm}$ transverse momentum spectrum has been observed to fit with a power-law function in the range $p_T > 0.5$ GeV/c.

The particle ratios, K^{*0}/K and ϕ/K^{*0}, and the K^{*0} mean transverse momentum, $\langle p_T \rangle$, have been studied in central Au+Au, different centrality bins in minimum bias Au+Au and p+p collisions. The K^{*0} nuclear modification factor, R_{AA}, has been measured as a function of p_T by comparing the K^* yields in top 10% central Au+Au and p+p collisions. The K^{*0} elliptic flow v_2 has been measured as a function of p_T and as a function of collision centrality in minimum bias Au+Au collisions.

7.1 Production Properties

A significant K^{*0} mass downward shift has been observed at low p_T in both central Au+Au and p+p collisions and this mass shift decreases as a function of p_T. The K^* mass shift in Au+Au collisions together with the measurements of the ρ^0 and Δ^{++} masses agree with the theoretical predictions that resonances with extremely short lifetimes in a hot and dense medium can interact with the surrounding hadrons and the properties of the resonances would be modified by this resonance in-medium effect.

The K^*/K ratios in Au+Au collisions have been observed to be significantly smaller than the ratio in p+p collisions. This K^*/K ratio difference gives us information that between the chemical and kinetic freeze-out stages in Au+Au collisions, the K^* decayed daughter particles scatter with the hadrons in the medium and this re-scattering effect has destroyed a portion of the primordial K^* yields. This K^* daughter particles' re-scattering effect is p_T dependent. K^* resonances with larger p_T have a greater chance to escape the medium and thus avoid the re-scattering effect. Our observation that the K^{*0} mean p_T in Au+Au collisions is significantly larger than the mean p_T in p+p collisions agrees with the p_T dependence of the K^* daughter particles' re-scattering effect.

Considering the total cross section between $\pi - \pi$ interactions is in magnitude larger than the cross section between $K - \pi$ interactions, the number of K^* signals re-produced by the re-generation effect is much smaller than the K^* yields destroyed by the daughter particles' re-scattering effect. Thus by comparing the K^*/K ratio in central Au+Au and p+p collisions, the time between the chemical and kinetic freeze-outs has been estimated to have a lower limit, 3 ± 1 fm/c. This is consistent with Rafelski's theoretical calculation and the UrQMD model prediction.

The K^* nuclear modification factor R_{AA} with $p_T >\sim 1.6$ GeV/c is observed to be close to the R_{CP} of K_S^0 and significantly different from the Λ R_{CP}. This indicates that the nuclear modification factor might be particle type (meson vs. baryon) dependent rather than particle mass dependent.

With the currently available statistics, there is no significant difference between the observed K^{*0} v_2 and the observed charged hadron v_2.

7.2 Future Directions

In the 2004 RHIC Au+Au run, we expect to have a factor of 20 more statistics than the second RHIC run. This will enable us to precisely measure the K^* mass and width as a function of p_T in Au+Au collisions. We also expect to greatly reduce the statistical uncertainties of the K^* mid-rapidity yields, dN/dy, and the inverse slope parameters, T. The future available statistics can also enable us to more precisely measure the K^* elliptic flow v_2 as a function of p_T and as a function of collision centrality.

With the full coverage TOFr being installed in the STAR detector hopefully in 2006, the pion and kaon particle identification can be extended with momentum up to around 1.6 GeV/c. This should greatly reduce the residual background in the $K\pi$ invariant mass spectrum.

With the measurement of $\Lambda(1520)$ production in Au+Au collisions, together with the K^* measurement, it may enable us to estimate both the medium temperature and the time scale between chemical and kinetic freeze-outs. The full coverage TOFr can also effectively identify the electrons and positrons. This might provide us great chances to reconstruct the ρ^0 resonance signal via the di-lepton channel. This future measurement may give us an estimation of the upper limit of the time scale.

Appendix A

Kinematic Variables

The transverse momentum of a particle is defined by using the momentum azimuthal components p_x and p_y

$$p_T = \sqrt{p_x^2 + p_y^2} \tag{A.1}$$

Then the transverse mass for a particle with mass m_0 is defined as

$$m_T = \sqrt{m_0^2 + p_T^2} \tag{A.2}$$

Thus

$$m_T dm_T = \frac{\sqrt{m_0^2 + p_T^2}}{2\sqrt{m_0^2 + p_T^2}} dp_T^2 = p_T dp_T \tag{A.3}$$

The energy of a particle is

$$E = \sqrt{m_0^2 + p_x^2 + p_y^2 + p_z^2} = \sqrt{m_T^2 + p_z^2} \tag{A.4}$$

Thus the rapidity variable y is defined as

$$y = \frac{1}{2}\ln\frac{E + p_z}{E - p_z} \tag{A.5}$$

Then

$$E = m_T \cosh y \tag{A.6}$$

$$p_z = m_T \sinh y \tag{A.7}$$

If θ is the angle between the particle momentum and the beam axis, then the pseudo-rapidity η is defined as

$$\eta = -\ln[\tan(\theta/2)] \tag{A.8}$$

Appendix B

Branching Ratio

Here we discuss how to use the isospin quantum numbers to calculate the decay branching ratio for the $K^*(892)$ resonance by assuming 100% of the K^* meson decays in the $K\pi$ channel.

As we know, the isospin z-component (I_z) of a u quark is $\frac{1}{2}$ and the I_z of a d quark is $-\frac{1}{2}$. Thus the isospin state of a proton can be written as $|I, I_z\rangle = |\frac{1}{2}, \frac{1}{2}\rangle$ and the isospin state of a neutron can be written as $|I, I_z\rangle = |\frac{1}{2}, -\frac{1}{2}\rangle$.

In the case of $K^{*0}(d\overline{s})$, the isospin state is $|I, I_z\rangle = |\frac{1}{2}, -\frac{1}{2}\rangle$. It can decay in two channels

$$K^{*0}(d\overline{s}) \rightarrow K^0(d\overline{s}) + \pi^0((u\overline{u} - d\overline{d})/\sqrt{2}) \tag{B.1}$$

$$K^{*0}(d\overline{s}) \rightarrow K^+(u\overline{s}) + \pi^-(d\overline{u}) \tag{B.2}$$

The isospin states for the decayed daughters are: K^0: $|I_1, I_{1z}\rangle = |\frac{1}{2}, -\frac{1}{2}\rangle$ and π^0: $|I_2, I_{2z}\rangle = |1, 0\rangle$; or K^+: $|I_1, I_{1z}\rangle = |\frac{1}{2}, \frac{1}{2}\rangle$ and π^-: $|I_2, I_{2z}\rangle = |1, -1\rangle$.

Since both the decay channels have two daughters with $I_1 = \frac{1}{2}$ and $I_2 = 1$, the K^{*0} decay can be expressed as $|I_1, I_2; I, I_z\rangle = |\frac{1}{2}, 1; \frac{1}{2}, -\frac{1}{2}\rangle$. The right side of the decay shown in B.1 can be written as $|I_1, I_2; I_{1z}, I_{2z}\rangle = |\frac{1}{2}, 1; -\frac{1}{2}, 0\rangle$. The right side of the decay shown in B.2 can be written as $|I_1, I_2; I_{1z}, I_{2z}\rangle = |\frac{1}{2}, 1; \frac{1}{2}, -1\rangle$. Then by reading the Clebsch-Gordan Coefficients, we can have

$$|\frac{1}{2}, 1; \frac{1}{2}, -\frac{1}{2}\rangle = \frac{1}{\sqrt{3}}|\frac{1}{2}, 1; -\frac{1}{2}, 0\rangle - \frac{2}{\sqrt{3}}|\frac{1}{2}, 1; \frac{1}{2}, -1\rangle \tag{B.3}$$

Thus we know that the decay branching ratio for B.1 is 1/3 and the decay branching ratio for B.2 is 2/3.

In the case of K^{*+}, it has two decay channels

$$K^{*+}(u\overline{s}) \rightarrow K^{+}(u\overline{s}) + \pi^{0}((u\overline{u} - d\overline{d})/\sqrt{2}) \tag{B.4}$$

$$K^{*+}(u\overline{s}) \rightarrow K^{0}(d\overline{s}) + \pi^{+}(u\overline{d}) \tag{B.5}$$

Thus the K^{*+} decay $|I_1, I_2; I, I_z\rangle = |\frac{1}{2}, 1; \frac{1}{2}, \frac{1}{2}\rangle$. The right side of the decay shown in B.4 can be written as $|I_1, I_2; I_{1z}, I_{2z}\rangle = |\frac{1}{2}, 1; \frac{1}{2}, 0\rangle$. The right side of the decay shown in B.5 can be written as $|I_1, I_2; I_{1z}, I_{2z}\rangle = |\frac{1}{2}, 1; -\frac{1}{2}, 1\rangle$. Then we have

$$|\frac{1}{2}, 1; \frac{1}{2}, \frac{1}{2}\rangle = -\frac{1}{\sqrt{3}}|\frac{1}{2}, 1; \frac{1}{2}, 0\rangle + \frac{2}{\sqrt{3}}|\frac{1}{2}, 1; -\frac{1}{2}, 1\rangle \tag{B.6}$$

Thus we know that the decay branching ratio for B.4 is 1/3 and the decay branching ratio for B.5 is 2/3.

Appendix C

STAR Collaboration

J. Adams[4], C. Adler[13], M.M. Aggarwal[28], Z. Ahammed[44], J. Amonett[17], B.D. Anderson[17], D. Arkhipkin[12], G.S. Averichev[11], J. Balewski[14], O. Barannikova[31], L.S. Barnby[4], S. Bekele[27], V.V. Belaga[11], R. Bellwied[47], J. Berger[13], B.I. Bezverkhny[49], S. Bharadwaj[32], H. Bichsel[46], L.C. Bland[5], C.O. Blyth[4], B.E. Bonner[33], M. Botje[25], A. Boucham[38], A. Brandin[24], A. Bravar[5], R.V. Cadman[1], H. Caines[49], M. Calderon[5], J. Carroll[20], J. Castillo[20], P. Chaloupka[26], S. Chattopdhyay[44], H.F. Chen[35], Y. Chen[7], M. Cherney[10], A. Chikanian[49], W. Christie[5], T.M. Cormier[47], J.G. Cramer[46], H.J. Crawford[37], D. Das[44], S. Das[44], L. Didenko[5], T. Dietel[13], X. Dong[35], W.J. Dong[7], J.E. Draper[6], F. Du[49], A.K. Dubey[3], V.B. Dunin[11], J.C. Dunlop[5], M.R. Dutta Mazumdar[44], V. Eckardt[22], L.G. Efimov[11], V. Emelianov[24], J. Engelage[37], G. Eppley[33], M. Estienne[38], P. Fachini[5], V. Faine[5], R. Fatemi[14], J. Fedorisin[11], K. Filimonov[20], P. Filip[26], E. Finch[49], Y. Fisyak[5], D. Flierl[13], K.J. Foley[5], K. Fomenko[11], J. Fu[48], C.A. Gagliardi[39], J. Gans[49], M.S. Ganti[44], L. Gaudichet[38], F. Geurts[33], V. Ghazikhanian[7], P. Ghosh[44], J.E. Gonzalez[7], O. Grachov[47], S. Gronstal[10], D. Grosnick[43], S.M. Guertin[7], A. Gupta[16], T.D. Gutierrez[6], T.J. Hallman[5], A. Hamed[47], H. Hardtke[20], M. Heinz[49], T.W. Henry[39], S. Hepplemann[29], B. Hippolyte[49], A. Hirsch[31], E. Hjort[20], G.W. Hoffmann[40], S.L. Huang[35], H.Z. Huang[7], E. Hughes[50], T.J. Humanic[27], G. Igo[7], A. Ishihara[40], W.W. Jacobs[14], P. Jacobs[20], M. Janik[45], H. Jiang[7], P.G. Jones[4], E.G. Judd[37], S. Kabana[49], M. Kaplan[8], D. Keane[17], J. Kiryluk[21], A. Kisiel[45], E.M. Kislov[11], J. Klay[20], S.R. Klein[20], A. Klyachko[14], D.D. Koetke[43], T. Kollegger[13], M. Kopytine[17], L. Kotchenda[24],

M. Kramer[9], P. Kravtsov[24], K. Krueger[1], A.I. Kulikov[11], A. Kumar[28], C.L. Kunz[8], R.Kh. Kutuev[12], A.A. Kuznetsov[11], M.A.C. Lamont[4], J.M. Landgraf[5], S. Lange[13], F. Laue[5], J. Lauret[5], A. Lebedev[5], R. Lednicky[11], S. Lehocka[11], M.J. LeVine[5], C. Li[35], Q. Li[47], S.J. Lindenbaum[9], M.A. Lisa[27], F. Liu[48], L. Liu[48], Z. Liu[48], Q.J. Liu[46], T. Ljubicic[5], W.J. Llope[33], H. Long[7], R.S. Longacre[5], M. Lopez-Noriega[27], W.A. Love[5], T. Ludlam[5], D. Lynn[5], J. Ma[7], D. Magestro[27], S. Mahajan[16], D.P. Mahapatra[3], R. Majka[49], L.K. Mangotra[16], R. Manweiler[43], S. Margetis[17], C. Markert[49], L. Martin[38], J.N. Marx[20], H.S. Matis[20], C.J. McClain[1], T.S. McShane[10], F. Meissner[20], M. Miller[21], Z. Milosevich[8], C. Mironov[17], A. Mischke[25], D. Mishra[3], B. Mohanty[44], L. Molnar[31], C.F. Moore[40], M.J. Mora-Corral[22], V. Morozov[20], B.K. Nandi[44], T.K. Nayak[44], J.M. Nelson[4], P.K. Netrakanti[44], V.A. Nikitin[12], B. Norman[17], G. Odyniec[20], A. Ogawa[5], V. Okorokov[24], M. Oldenburg[20], D. Olson[20], S.K. Pal[44], Y. Panebratsev[11], S.Y. Panitkin[5], A.I. Pavlinov[47], T. Pawlak[45], T. Peitzmann[25], V. Perevoztchikov[5], C. Perkins[37], W. Peryt[45], V.A. Petrov[12], S.C. Phatak[3], R. Picha[6], M. Planinic[41], J. Pluta[45], N. Porile[31], J. Porter[5], A.M. Poskanzer[20], M. Potekhin[5], E. Potrebenikova[11], B.V.K.S. Potukuchi[16], D. Prindle[46], C. Pruneau[47], J. Putschke[22], G. Rai[20], G. Rakness[29], R. Raniwala[32], S. Raniwala[32], O. Ravel[38], R.L. Ray[40], S.V. Razin[11], D. Reichhold[31], J.G. Reid[46], G. Renault[38], F. Retiere[20], A. Ridiger[24], H.G. Ritter[20], J.B. Roberts[33], O.V. Rogachevskiy[11], J.L. Romero[6], A. Rose[47], L. Ruan[35], I. Sakrejda[20], S. Salur[49], J. Sandweiss[49], I. Savin[12], P.S. Sazhin[11], J. Schambach[40], R.P. Scharenberg[31], N. Schmitz[22], L.S. Schroeder[20], K. Schweda[20], J. Seger[10], P. Seyboth[22], E. Shahaliev[11], M. Shao[35], W. Shao[50], M. Sharma[28], S.S. Shimanskiy[11], F. Simon[22], R.N. Singaraju[44], G. Skoro[11], N. Smirnov[49], R. Snellings[25], G. Sood[28], P. Sorensen[20], J. Sowinski[14], H.M. Spinka[1], B. Srivastava[31], L. St.. Claire[20], A. Stadnik[11], R. Stock[13], A. Stolpovsky[47], M. Strikhanov[24], B. Stringfellow[31], C. Struck[13], E. Sugarbaker[27], C. Suire[5], M. Sumbera[26], B. Surrow[21], T.J.M. Symons[20], P. Szarwas[45], A. Tai[7], A.H. Tang[25], D. Thein[7], J.H. Thomas[20], S. Timoshenko[24], M. Tokarev[11], T.A. Trainor[46], S. Trentalange[7], R.E. Tribble[39], O. Tsai[7], T. Ullrich[5], D.G. Underwood[1], A. Urkinbaev[11], G. Van Buren[5], R. Varma[18], I.M. Vasilevski[12], S.E. Vigdor[14], V.P. Viyogi[44], S. Vokal[11], M. Vznuzdaev[24], B. Waggoner[10], G. Wang[17], X.L. Wang[35], Z.M. Wang[35], Y. Wang[40], G. Wang[50], F. Wang[31], H. Ward[40], J.C. Webb[14], R. Wells[27], C. Whitten Jr.[7], H. Wieman[20], S.W.

Wissink[14], R. Witt[49], J. Wood[7], J. Wu[35], Z. Xu[35], Z. Xu[5], N. Xu[20], E. Yamamoto[20], P. Yepes[33], V.I. Yurevich[11], Y.V. Zanevsky[11], Z.P. Zhang[35], H. Zhang[49,5], P.A Zolnierczuk[14], R. Zoulkarneev[12], Y. Zoulkarneeva[12], A.N. Zubarev[11].

[2]Institute of High Energy Physics - Beijing

[18]Indian Institute of Technology. Mumbai

[19]Institute of Modern Physics. Lanzhou

[21]Massachusetts Institute of Technology

[42]Tsinghua University

[50]California Institute of Technology

[1]Argonne National Laboratory

[5]Brookhaven National Laboratory

[8]Carnegie Mellon University

[9]City College of New York

[10]Creighton University

[14]Indiana University

[3]Institute of Physics. Bhubaneswar

[15]Institut de Recherches Subatomiques de Strasbourg

[30]Institute of High Energy Physics - Protvino

[48]Institute of Particle Physics - Wuhan

[17]Kent State University

[11]Laboratory of High Energy Physics - Dubna

[20]Lawrence Berkeley National Laboratory

[22]Max-Planck-Institut fuer Physics

[23]Michigan State University

[24]Moscow Engineering Physics Institute

[25]NIKHEF

[26]Nuclear Physics Inst., Academy of Sciences

[27]Ohio State University

[28]Panjab University

[12]Particle Physics Laboratory - Dubna

[29]Pennsylvania State University

[31]Purdue University
[33]Rice University
[36]Shanghai Institue of Nuclear Research - SINR
[38]SUBATECH - Nantes
[39]Texas A & M University
[34]Instituto de Fisica da Universidade de Sao Paulo
[4]University of Birmingham
[37]University of California, Berkeley
[6]University of California - Davis
[7]University of California - Los Angeles
[13]University of Frankfurt
[16]Jammu University
[32]University of Rajasthan
[35]University of Science and Technology of China - USTC
[40]University of Texas - Austin
[46]University of Washington
[41]University of Zagreb
[43]Valparaiso University
[44]Variable Energy Cyclotron Centre. Kolkata
[45]Warsaw University of Technology
[47]Wayne State University
[49]Yale University

Bibliography

[1] T. Blum *et al.*, Phys. Rev. D **51**, 5153 (1995).

[2] P. Braun-Munzinger, Nucl. Phys. A **681** 119-123 (2001).

[3] D. Griffiths, *Introduction to Elementary Particles* (Addison-Wesley Publishing Company Inc.), First Edition, 1987.

[4] R. Rapp, Phys. Rev. C **66**, 027901 (2002).

[5] R. Rapp and E.V. Shuryak, Phys. Rev. Lett. **86**, 2980 (2001).

[6] P. Braun-Munzinger *et al.*, Phys. Lett. B **518** 41-46 (2001).

[7] D. Magestro, J.Phys. G **28** (2002) 1745-1752.

[8] C. Adler *et al.*, Phys. Rev. Lett. **89** 202301 (2002).

[9] C. Adler *et al.*, Kaon Production in Au+Au at 130 GeV to be pulished in Phys. Lett. B.

[10] A. Poskanzer and S. Voloshin, Phys. Rev. C **58** 1671 (1998).

[11] P. Fachini *et al.*, STAR TOF Proposal (2003).

[12] C. Adler *et al.*, Phys. Rev. Lett. **90** 032301 (2003).

[13] Y. Dokshitzer, D. Kharzeev, Phys. Lett. B **519** 199 (2001).

[14] D. Park, *Introduction to the Quantum Theory*(McGraw-Hill Inc.), second edition, 1974.

[15] Particle Data Group, Phys. Rev. D **45** (1992).

[16] L. Alvarez, Nobel Lecture, December 11, 1968.

[17] J. Adams *et al.*, nucl-ex/0307023.

[18] H. Zhang, in Proceedings of Strange Quark Matter 2003, nucl-ex/0306034.

[19] P. Fachini, in Proceedings of Strange Quark Matter 2003, nucl-ex/0305034.

[20] J. Ma, in Proceedings of Strange Quark Matter 2003, nucl-ex/0306014.

[21] A. Tai, STAR Collaboration, Internal STAR analysis meeting 2003.

[22] S. Salur, STAR Collaboration, Internal STAR analysis meeting 2003.

[23] L. Gaudichet, in Proceedings of Strange Quark Matter 2003, nucl-ex/0307013.

[24] R. Witt, STAR Collaboration, Internal STAR analysis meeting 2003.

[25] G. Brown and M. Rho, Phys. Rev. Lett. **66** 2720-2723 (1991).

[26] R. Rapp, hep-ph/0305011.

[27] E. Shuryak and G. Brown, Nucl. Phys. A **717**, 322 (2003).

[28] M. Bleicher and J. Aichelin, hep-ph/0201123.

[29] R. Rapp and J. Wambach, Adv. Nucl. Phys. **25**, 1 (2000).

[30] R. Rapp, Phys. Rev. C **63**, 054907 (2001).

[31] J. Schaffner-Bielich, Phys. Rev. Lett. **84**, 3261 (2000).

[32] J. Letessier *et al.*, J. Phys. G **27**, 427 (2001).

[33] G. Torrieri and J. Rafelski, Phys. Lett. B **509**, 239 (2001).

[34] W. Broniowski and W. Florkowski, Phys. Rev. Lett. **87**, 272302 (2001).

[35] A. Baltz and C. Dover, Phys. Rev. C **53**, 362 (1996).

[36] G. Torrieri and J. Rafelski, hep-ph/0112195, in Proceedings of Strange Quark Matter 2001.

[37] M. Bleicher *et al.*, hep-ph/9909407.

[38] S. Pal, C. Ko and Z. Lin, nucl-th/0202086.

[39] S. Afanasiev *et al.*, Phys. Lett. B **491**, 59 (2000).

[40] M. Abreu *et al.*, J. Phys. G. **27**, 405 (2001).

[41] X. Dong, STAR Collaboration, Internal STAR analysis meeting 2003.

[42] Z. Xu, STAR Collaboration, Internal STAR analysis meeting 2003.

[43] Introduction on RHIC at http://www.bnl.gov/RHIC/.

[44] P. Sorenson, Ph.D. thesis, UCLA, 2003.

[45] J. Schukraft, the 19th Symposium on Multiparticle Dynamics, Arles, France, 13-17 June 1988; KEK88-10-390.

[46] S. van der Meer, ISR-PO/68-31, KEK 68-64.

[47] C. Adler *et al.*, nucl-ex/0008005.

[48] Z. Xu, R. Majka and J. Sandweiss, STAR Note, October 9, 2000.

[49] A. Drees, Z. Xu and H. Zhang, Paper in Preparation on Vernier Scan at RHIC.

[50] J. Harris *et al.*, Nucl. Instrum. Meth. A **499**, 624 (2003).

[51] M. Anderson *et al.*, Nucl. Instrum. Meth. A **499**, 659 (2003).

[52] A. Tang, Ph.D. thesis, Kent State University, 2002.

[53] STAR Trigger Definitions, STAR Internal Documents.

[54] C. Adler *et al.*, Phys. Rev. Lett. **89**, 092301 (2002).

[55] C. Adler *et al.* Phys. Rev. C **66**, 061901(R) (2002).

[56] L. Gaudichet, STAR Note.

[57] H. Long, Ph.D. thesis, UCLA, 2002.

[58] CERN RD44 Project at http://wwwinfo.cern.ch/asd/geant/geant4public/G4UsersDocuments/Welcome/IntroductionToGeant4/html/introductionToGeant4.html.

[59] P. Nevski, http://www.star.bnl.gov/STARAFS/comp/simu/gstar/gstar.html.

[60] C. Adler *et al.*, Phys. Rev. C **66**, 034904 (2002).

[61] R. Longacre, Paper in Preparation.

[62] T. Sjorstrand *et al.*, hep-ph/0108264.

[63] D. Griffiths, *Introduction to Elementary Particles* (John Wiley and Sons, Inc.) 1987.

[64] J. Adams *et al.*, STAR paper submitted to PRL.

[65] J. Adams *et al.*, STAR paper in Preparation.

[66] J. Adams *et al.*, STAR paper submitted to PRL.

[67] J. Adams *et al.*, STAR paper in Preparation.

[68] M. Derrick *et al.*, Phys. Lett. B **158**, 519 (1985).

[69] Y. Pei, Z. Phys. C **72**, 39 (1996).

[70] P. Chliapnikov, Phys. Lett B **470**, 263 (1999).

[71] T. Akesson *et al.*, Nucl. Phys. B **203**, 27 (1982).

[72] K. Abe *et al.*, Phys. Rev. D **59**, 052001 (1999).

[73] H. Albrecht *et al.*, Z. Phys. C **61**, 1 (1994).

[74] J. Canter *et al.*, Phys. Rev. D **20**, 1029 (1979).

[75] D. Drijard *et al.*, Z. Phys. C **9**, 293 (1981).

[76] M. Aguilar-Benitez *et al.*, Z. Phys. C **50**, 405 (1991).

[77] J. Adams et al, STAR paper submitted to Phys. Rev. Lett., nucl-ex/0306007.

[78] J. Dunlop, STAR internal studies.

[79] B. Lasiuk, STAR internal studies.

[80] Private Communication with D. Magestro.

[81] E.V. Shuryak and G.E. Brown, hep-ph/0211119.

[82] F. Becattini, Nucl. Phys. A **702**, 336 (2002).

[83] J. D. Jackson, *Remarks on the Phenomenological Analysis of Resonances*, 1964.

[84] D. Perkins, *Introduction to High Energy Physics* (Addison-Wesley Publishing Company Inc.), Third Edition, 1987.